



HAL
open science

Synthesis and Characterization of BiVO₄ nanostructured materials: application to photocatalysis

Venkatesan Rajalingam

► **To cite this version:**

Venkatesan Rajalingam. Synthesis and Characterization of BiVO₄ nanostructured materials: application to photocatalysis. Condensed Matter [cond-mat]. Le Mans Université; Centro de Investigación y de Estudios Avanzados del Instituto Politécnico Nacional (Mexico), 2014. English. NNT: 2014LEMA1018 . tel-01150464

HAL Id: tel-01150464

<https://theses.hal.science/tel-01150464>

Submitted on 11 May 2015

HAL is a multi-disciplinary open access archive for the deposit and dissemination of scientific research documents, whether they are published or not. The documents may come from teaching and research institutions in France or abroad, or from public or private research centers.

L'archive ouverte pluridisciplinaire **HAL**, est destinée au dépôt et à la diffusion de documents scientifiques de niveau recherche, publiés ou non, émanant des établissements d'enseignement et de recherche français ou étrangers, des laboratoires publics ou privés.

Thèse de Doctorat

Venkatesan RAJALINGAM

*Mémoire présenté en vue de l'obtention du
grade de Docteur de l'Université du Maine
sous le label de L'Université Nantes Angers Le Mans*

École doctorale : 3MPL, Le Mans

Discipline : PHYSIQUE

Spécialité : PHYSIQUE DE LA MATIERE CONDENSEE

Unité de recherche : INSTITUT DES MOLECULES ET MATERIAUX DU MANS

Soutenue le 21 Janvier 2014

TITRE : SYNTHÈSE ET CARACTÉRISATIONS DES MATERIAUX NANOSTRUCTURES DE BiVO_4 : APPLICATION A LA PHOTOCATALYSE

JURY

Rapporteurs : **MME. SOUAD AMMAR-MERAH**, ITODYS-CNRS, UNIVERSITE PARIS DIDEROT (PARIS)
M. HORACIO ESTRADA, CENAM (QUERETARO - MEXIQUE)

Examineurs : **M. ALAIN BULO**, INSTITUT DES MOLECULES ET MATERIAUX DU MANS
M. YASUHIRO MATSUMOTO, CINVESTAV - IPN (MEXICO D.F.), *PRESIDENT*

Invité(s) : **M. MIGUEL GARCIA ROCHA**, CINVESTAV - IPN (MEXICO D.F.)

Co-directeur de Thèse **M. SUBRAMANIAM VELUMANI**, CINVESTAV - IPN (MEXICO D.F.)

Directeur de Thèse **M. ABDEL HADI KASSIBA**, INSTITUT DES MOLECULES ET MATERIAUX DU MANS

I hereby declare that the work presented in this thesis is entirely original and carried out by me at Center for Research and Advanced Studies of the National Polytechnic Institute (CINVESTAV-IPN), Zacatenco, Mexico D.F. and also at the Institut des Molécules et Matériaux du Mans (IMMM), Université du Maine, Le Mans, France. I further declare that this work has not formed the basis for the award of any degree or diploma or any other similar title of any other university or institution of higher learning.

21st January 2014.

Venkatesan RAJALINGAM

To

Mother (மாதா), Father (பாதா),

Teachers (பாடகர்), Brothers

(தம்பி) and to the Angel who is

blessing My Life.

Acknowledgement

One of the joys of completion is to look over the past journey of these four years of my PhD. First and foremost I would like to express my heartfelt gratitude to my thesis advisor Professor. Velumani Subramaniam. This work would not have been possible without his guidance, support and encouragement. Under his guidance I successfully overcome many difficulties and learned a lot in approaching both the personal and professional life. Despite his busy schedule in international co-ordination and research work he supported me through his valuable suggestions and made corrections. I am so grateful that he has given me an opportunity for the co – graduation. Also to attend the conferences which were important for this research work.

I am extremely thankful to the man who inspired and guided me to the art of research and personal life Professor. Abdel Hadi Kassiba, my thesis co-advisor, Universite du Maine. I am thanking him especially for his expert guidance, professionalism and diplomacy. I am so grateful for the time he spent on scientific discussions and ethics, which were useful in expanding my scientific knowledge and enabled me to finish my degree successfully.

With gratefulness, I would like to thank Cinvestav-IPN and Universite du Maine, for giving me an opportunity to carry out my studies and also for their financial support to attend various conferences. I am very grateful to the DGRI-SRE-SEP for granting the scholarship “Becas a extranjeros para programas de calidad y competencia internacional en Mexico”. I would like to acknowledge the financial support from European Union FP7- NMP EU-Mexico program under grant agreement no 263878/ by CONACYT no 125141.

I would like to extend my sincere thanks to Prof. Miguel Garcia Rocha, Prof. Yasuhiro Matsumoto, Prof. Mauricio Ortega Lopez, Prof. Horacio Estrada Vazquez and Prof. Frantisek Sutara for their several hours spent on meetings and scientific discussions especially their critical comments and suggestions. Thanks to all the professors and secretaries in Cinvestav-IPN and Universite du Maine for their hearty smile and care, this made me comfortable to work in these research institutes. Thanks to Dr. Jesus Arenas-Alatorre, IF-UNAM, Mexico City for his help in HRTEM investigations and teaching me some basic software for HRTEM image analysis. I am very grateful to Prof. Alain Gibaud, for his ever friendly cheerful discussions on XRD matching.

I also wish to express my sincere thanks to Prof. Gweneal Corbel, for the in situ annealing studies and also for his suggestions and discussions on our research work which helped me to perform cutting research activities. I wish to express my gratefulness to Prof. Nicolas Errien for his support, encouragement and technical discussions. I would like to thank Eng. Mathieu Edely for his guidance on handling the experimental and characterization instruments.

I am also indebted to Miguel Angel Luna, Miguel Galván Arellano, Adolfo Tavira Fuentes, Alvaro Guzmán Campuzano, Alejandro Cesar Meza Serrano, Gabriela Lopez (SEES), Fis. Josue Romero Ibarra, M. I Alvaro Pascual Angeles (LANE) and Marcela Guerrero and Zacarías Rivera (Physics department) for their technical assistance and friendly conversations. Special thanks go to my fellow group members, former and present, who took part in my work by creating a unique and encouraging atmosphere. I would like to thank my friend and peer M. Gurusamy who made even my little free time highly enjoyable during these intense four years, especially for all the discussions, care and moral support. My gratitude and heartfelt thanks to all Indian and Mexican friends, for their moral support and encouragements. Many thanks to my friend Dr. Shashi Kumar for being patient with my questions and helping me understand several aspects of life.

I would like to thank all the staff from Governement arts college, Coimbatore, India, especially Prof. Vijayalakshmi and Prof. Devaraj for their consistent guidance towards the research activity. My special thanks to Capt. Saravanan, India, who made me to dream and achieve this research work. I doubt that I will ever able to convey my appreciation fully, but I owe my deepest gratitude. I am also very grateful to Dr. Rathinavel Ponnusamy who gave the meaning of generosity.

Last but not the least I would like to pay high regards to my beloved family for their sincere encouragement, inspiration and unconditional support for shaping my personal and academic life and without whom I would have not stepped into such a stage at what I am right now. I owe everything to them. A special thanks to Mrs. Malathy Velumani for her continuous encouragement and care. Above all thanks to the Angel who is blessing my life to manage all the ups and downs throughout my stay away from home. Besides this several people have knowingly and unknowingly helped me in the successful completing of this thesis work. I am very grateful to each and every one of them.

Contents

	Page no.
List of tables	iv
List of figures	v
Abbreviations	xi
Abstract	xiv
Chapter 1: General Introduction	21
1.1. Choice of photocatalyst and BiVO ₄	22
1.2. Features of BiVO ₄	23
1.2.1. Crystal polytypes and optical properties	23
1.2.2. Numerical simulation of crystal and electronic band structures of BiVO ₄	24
1.3. Basic concept of Photocatalysis	26
1.3.1. State of art oxide and non-oxide based semiconductor photocatalysts	28
1.3.2. Photocatalytic properties of bismuth based semiconductors	30
1.3.3. Synthesis of BiVO ₄ : a state of art	31
Chapter 2: Synthesis and characterization techniques	40
2.1. Bismuth vanadate (BiVO ₄) powder preparations	40
2.1.1. Hydrothermal technique	40
2.1.1a. Hydrothermal synthesis of BiVO ₄ powders with surfactant	41
2.1.1b. Hydrothermal synthesis of BiVO ₄ powders without surfactant	42
2.1.2. Ball milling	42
2.1.2a. Mechanical alloying process	43
2.1.2b. Mechanochemical preparation of BiVO ₄ powders	43
2.2. BiVO ₄ thin film preparations	44
2.2.1. Ultrasonic spray pyrolysis (USP)	45
2.2.1a. Preparation of BiVO ₄ thin film using ball milled BiVO ₄ precursor	45
2.2.1b. Preparation of BiVO ₄ thin film using commercial precursors	46
2.2.2. Preparation of BiVO ₄ thin film by RF-Sputtering	47
2.2.2a. Thin film deposition	48
2.2.2b. Thin film annealing	49
2.3. BiVO ₄ characterization techniques	49
2.3.1. Structural investigations	49
2.3.2. Surface analysis by field emission scanning electron microscope (FE-SEM)	51
2.3.3. Surface studies by atomic force microscope (AFM)	51
2.3.4. Structural studies by high resolution transmission electron microscope	52
2.3.5. Elemental analysis by energy dispersive X-ray analysis (EDAX)	52
2.3.6. Optical absorption studies by UV-Vis spectroscopy	52
2.3.7. Raman spectroscopy studies	54
2.3.8. Fourier transform infrared (FT-IR) spectroscopy studies	55

2.3.9. Dielectric measurements	55
2.3.10. Electron paramagnetic resonance (EPR)	56
2.3.11. Photocatalytic set-up	57
2.3.11a. Photodegradation reaction for BiVO ₄ powder	57
2.3.11b. Photodegradation reaction for BiVO ₄ thin film	57
Chapter 3: BiVO₄ powders: Results and discussions	60
3.1. Hydrothermal process	61
3.1.1. Influence of pH	61
3.1.1a. XRD analysis	61
3.1.1b. Raman investigations	62
3.1.1c. Surface morphological analysis by FE-SEM	63
3.1.2. Influence of surfactants	64
3.1.2a. XRD and Raman investigations	64
3.1.2b. Surface morphological analysis by FE-SEM	65
3.1.3. Optical properties (UV-Visible and FT-IR)	66
3.2. Mechanochemical synthesis of BiVO ₄ powders	68
3.2.1. Effect of milling time	68
3.2.1a. XRD analysis	68
3.2.1b. Surface morphological analysis by FE-SEM	70
3.2.1c. UV-Vis absorption studies	71
3.2.2. Effect of ball to powder weight ratio (BPR)	72
3.2.2a. XRD and simulation studies	72
3.2.2b. Surface morphological analysis by FE-SEM	75
3.2.2c. Raman investigations	77
3.2.2d. UV-Visible diffuse reflectance spectroscopy (DRS)	78
3.2.2e. FT-IR spectroscopic analysis	79
3.2.3. Dielectric behavior, conduction and EPR active centers in BiVO ₄ nanoparticles	79
3.2.3a. Dielectric investigations-Theoretical background	80
3.2.3b. Frequency and temperature dependence of dielectric functions	81
3.2.3d. Frequency and temperature dependence conductivity	83
3.2.3e. Temperature dependance of relaxation times	84
3.2.3f. EPR investigations-theoretical background	87
3.2.3g. EPR spectral analysis	87
3.3. Reproducibility test of ball milled BiVO ₄	92
3.4. Conclusion	93
Chapter 4: BiVO₄ thin films: Results and discussions	96
4.1. Thin film deposition using ultrasonic spray pyrolysis	97
4.1.1. Effect of substrate temperature	98
4.1.1a. XRD analysis	98

4.1.1b. Surface morphological analysis by FE-SEM	99
4.1.1c. HR-TEM and Raman analysis	101
4.1.1d. UV-Visible absorption studies	102
4.2. Thin film deposition using RF-Sputtering	104
4.2.1. Effect of substrate temperature under Ar atmosphere	106
4.2.1a. Optimization of crystallization temperature (HT-XRD)	106
4.2.1b. XRD and Raman analysis	106
4.2.1c. Surface morphological analysis by FE-SEM and AFM	109
4.2.2. Effect of oxygen flow rate	111
4.2.2a. XRD analysis	111
4.2.2b. Surface morphological analysis by FE-SEM	112
4.2.3. Effect of substrate temperature under Ar+O ₂ atmosphere	113
4.2.3a. XRD analysis	113
4.2.3b. Surface and morphological analysis by FE-SEM and AFM	114
4.2.4. Optical characteristics	117
4.3. Conclusion	119
Chapter 5: Photocatalytic investigations	122
5.1. Concepts of photodegradation process	123
5.2. Photodegradation study of BiVO ₄ powders	124
5.2.1. Photodegradation effect on hydrothermally synthesized acicular BiVO ₄	124
5.2.2. Photodegradation study of ball milled BiVO ₄	126
5.2.3. Photodegradation study of USP deposited BiVO ₄ thin films	130
5.2.4. Photodegradation study of RF-Sputtered films under Ar atmosphere	132
5.2.5. Photodegradation study of RF-Sputtered films under Ar+O ₂ atmosphere	135
5.2.6. Reusability test of BiVO ₄ thin films	136
5.3. Conclusion	138
Chapter 6: Summary and future recommendations	140
6.1. Summary	140
6.2. Future recommendations	144
Publications	147
Conference contributions	147

List of tables

Table title	Page no.
Table 1.1	Bond length of monoclinic BiVO ₄ . 25
Table 1.2	Physical and structural parameters of monoclinic BiVO ₄ . 25
Table 1.3	Summary on ball milled BiVO ₄ . 34
Table 2.1	Characteristics parameters used for mechanochemical process. 45
Table 2.2	Variable parameters used for RF-Sputtering experiments. 50
Table 2.3	Chemical formula, molecular weight and maximum absorption wavelength for the Rh6 and MB dyes tested. 59
Table 3.1	Structural parameters of ball milled BiVO ₄ . 70
Table 3.2	Band gap absorption edges determined from diffuse reflectance experiments performed on the BiVO ₄ crystallites synthesized by ball milling with and without annealing. 80
Table 3.3	EPR spectral parameters of V ⁴⁺ in BiVO ₄ for samples A and B 89
Table 4.1	Structural parameters of USP deposited BiVO ₄ thin films at different substrate temperatures. 97
Table 4.2	Structural parameters of In situ HT-XRD for BiVO ₄ film deposited at room temperature under argon atmosphere. 105
Table 4.3	Structural parameters of BiVO ₄ post annealed (400°C) thin films. 107
Table 4.4	Calculated thickness of rf-sputtered BiVO ₄ films. 117
Table 5.1	Peak shift position of ball milled samples versus irradiation time. 127

List of figures

Figure title	Page no.
Fig.1.1. Human being top ten problems for next 50 years.	21
Fig.1.2. Band gap distribution of some semiconductors.	22
Fig.1.3. Crystal structure of monoclinic BiVO ₄ . (a) Conventional unit cell. (b) Density of states. (c) Band structure.	24
Fig.1.4. Photosynthesis by green plants and photocatalytic water splitting as an artificial photosynthesis. (Reproduced from ref.42).	26
Fig.1.5. A schematic illustration of the generation of electron-hole pairs and the corresponding redox reactions taking place on the semiconductor surface.	27
Fig.1.6. Phase diagram of Bi ₂ O ₃ -V ₂ O ₅ system.	32
Fig.2.1. Schematic representation of the steps followed in hydrothermal.	42
Fig.2.2. Planetary ball mill- Retsch PM 400.	43
Fig.2.3. Parameters affecting the milling process in a planetary ball mill.	44
Fig.2.4. Schematic representation of ball milling steps.	45
Fig.2.5. Ultrasonic spray pyrolysis setup and schematic diagram of the deposition process.	46
Fig.2.6. Schematic representation of the steps followed in USP using ball milled BiVO ₄ .	47
Fig.2.7. Schematic representation of the steps followed in USP using commercial precursors.	47
Fig.2.8. (a) The principle of rf-sputtering; (b) rf-sputtering instrument used for BiVO ₄ thin film depositions.	48
Fig.2.9. Schematic representation of the steps followed in the rf-sputtering.	49
Fig.2.10. XRD PANalytical Xpert equipment.	51
Fig.2.11. FE-SEM-Carl Zeiss Auriga 60 and SEM-JEOL, JSM 6510.	52
Fig.2.12. Atomic force microscope JEOL JSPM-5200.	52
Fig.2.13. HR-TEM-JEOL ARM200F.	53
Fig.2.14. UV-Visible spectrometer Cary varian 100 scan.	54
Fig.2.15. Raman spectroemeter-LabRAMJobinYvon.	55
Fig.2.16. FT-IR Spectroemeter Nicolet 510.	56
Fig.2.17. Dielectric relaxation spectrometer.	56
Fig.2.18. EPR spectrometer-EMX Bruker.	57
Fig.2.19. Experimental set up and schematic representation of photocatalytic reactor.	58
Fig.3.1. XRD patterns of BiVO ₄ catalysts obtained at (a) pH=2 and (b) pH=9 and XRD multi-peak separation for the BiVO ₄ crystallites from 28° to 30° according to the (-1 3 0), (-1 2 1) and (1 2 1) peaks.	62

Fig.3.2.	Raman spectra for BiVO ₄ catalysts obtained at (a) pH=2 and (b) pH=9 after thermal treatment.	63
Fig.3.3.	FE-SEM images of BiVO ₄ catalysts obtained at (a) pH 2 and (b) pH 9	64
Fig.3.4.	BiVO ₄ samples prepared with and without surfactants using hydrothermal method. A) XRD pattern and B) Raman spectra of the obtained BiVO ₄ powders.	65
Fig.3.5.	FESEM images of as prepared BiVO ₄ samples synthesized at different surfactants. (a) without surfactant, (b) OA, (c) HTAB, (d) PVA and (e) PVP.	67
Fig.3.6.	BiVO ₄ samples synthesized at (a) pH=2 and (b) pH = 9 A) UV-Visible and B) FT-IR spectra of BiVO ₄ powders.	68
Fig.3.7.	BiVO ₄ samples with and without surfactants using hydrothermal method A).UV-Visible and B) FT-IR spectra of BiVO ₄ powders.	68
Fig.3.8.	XRD patterns of BiVO ₄ products derived from different milling time.	70
Fig.3.9.	XRD patterns of 16 h milled and annealed BiVO ₄ powders (inset: magnification peak at 18.8°).	71
Fig.3.10.	FE-SEM images of BiVO ₄ (a) 16 h milled (b) 16 h milled annealed samples and (c) TEM image of 16h milled sample.	72
Fig.3.11.	UV-Visible DRS spectra of 16h milled and milled annealed samples. An inset figure shows ($\alpha h\nu$) ² vs ($h\nu$) graph.	72
Fig.3.12.	XRD patterns of BiVO ₄ samples prepared under different conditions. (A) Samples prepared under different BPR with 6 h milling time: a) 6 h5:1, b) 6 h8:1 and c) 6 h10:1. (B) Samples prepared under different BPR with 11 h milling time: a) 11 h5:1, b) 11 h8:1 and c) 11 h10:1. (C) Milled-annealed samples: a) 6 hA10:1, b) 11 hA10:1, c) 11 hA8:1. (D) The magnified XRD patterns near 18.5°, 35° and 47°: a) 6 h10:1 and b) 6 hA10:1.	74
Fig.3.13.	Experimental and simulated XRD patterns of monoclinic scheelite BiVO ₄ . The simulation is based on DFT calculations implemented in CASTEP code. The inset shows the characteristic unit cell of BiVO ₄ .	75
Fig.3.14.	XRD pattern of monoclinic BiVO ₄ sample obtained by 11 h milling and annealed at 450 °C for 1h: experimental (Yobs) and refined (Ycal) by using FullProf software.	75
Fig.3.15.	FE-SEM images of mechanochemically synthesized BiVO ₄ Nanoparticles A) As prepared and annealed samples of 6 h milled with 10:1 BPR, B) As prepared and annealed samples of 11 h milled with 10:1 BPR, C) As prepared and annealed samples of 11 h milled with 8:1 BPR.	77

Fig.3.16.	Raman spectra of ball milled samples in the defined conditions: a) 6 h10:1, b) 6 hA10:1, c) 11 h10:1, d) 11 hA10:1, e) 11 h8:1 and f) 11 hA8:1. Inset: frequency shift and FWHM decrease with annealing	78
Fig.3.17.	UV-Visible diffuse reflectance spectra of the as prepared samples: a) 6 h10:1, b) 6 hA10:1, c) 11 h10:1, d) 11 hA10:1, e) 11 h8:1 and f) 11 hA8:1.	80
Fig.3.18.	FT-IR spectra of BiVO ₄ obtained under different time durations of milling and after annealing: a) 6 h10:1, b) 6 hA10:1, c) 11 h10:1, d) 11 hA10:1, e) 11 h8:1 and f) 11 hA8:1.	81
Fig.3.19.	Temperature and frequency dependencies of real and imaginary dielectric permittivity in BiVO ₄ nanopowders of sample A ((a) and (b)) and sample B ((c) and (d)), continuous lines are fits obtained by Havriliak-Negami model.	83
Fig.3.20.	Nyquist plot of the imaginary part of impedance versus its real part for sample B at temperature of about 273K. Indications are also given on the frequency range HF, IF and LF designating, high, intermediate and low frequency regimes respectively.	84
Fig.3.21.	Frequency dependence (ac) of real part of conductivity $\sigma'(\omega)$ for different temperatures: a) A sample and b) B sample. The continuous lines are fits by Havriliak-Negami model.	85
Fig.3.22.	Temperature dependence of d.c conductivity in BiVO ₄ obtained under different synthesis conditions of samples A and B.	86
Fig.3.23.	Variation of the relaxation time versus the inverse temperature for samples A and B.	87
Fig.3.24.	Log-log plot of the d.c conductivity versus the relaxation time for samples A and B.	87
Fig.3.25.	EPR spectra of BiVO ₄ samples A and B. The graph (C) illustrates the contributions to the vanadium EPR spectrum from (1) anisotropic signal of isolated V ⁴⁺ and (2) background signal of V ⁴⁺ pairs or emanating from clustering of V ⁴⁺ ions.	91
Fig.3.26.	XRD patterns of as synthesized BiVO ₄ powders aged at different time.	92
Fig.3.27.	FE-SEM micrographs of as synthesized BiVO ₄ powders aged at different time.	93
Fig.4.1.	XRD patterns of BiVO ₄ thin films deposited at different substrate temperatures.	98
Fig.4.2.	FE-SEM micrographs of BiVO ₄ thin films deposited at different substrate temperatures a) 350°C b) 400°C c) 425 °C and d) 500 °C.	100

Fig.4.3.	HRTEM images of 425 °C deposited BiVO ₄ film, inset shows FFT and inverse FFT of the selected area.	101
Fig.4.4.	Raman spectra of BiVO ₄ thin films deposited at different T _{sub} (inset: frequency shift with T _{sub}).	102
Fig.4.5.	Dependence of FWHM of BiVO ₄ thin films prepared at different substrate temperatures.	102
Fig.4.6.	UV-Visible spectra of BiVO ₄ thin films. Inset shows plot of (αhν) ² against (hν).	103
Fig.4.7.	HT-XRD pattern of BiVO ₄ film deposited at room temperature and annealed in situ (inside XRD system) under argon atmosphere.	106
Fig.4.8.	XRD patterns and Raman spectra of BiVO ₄ thin films deposited at different substrate temperatures: a) RT deposited and b) deposited at 450°C. (A) and (B) as-deposited thin films, (C) and (D) post-annealed at 400°C thin films.	108
Fig.4.9.	FE-SEM micrograph of post-annealed (400°C) BiVO ₄ films grown on Si (100): (a) deposited at RT, (b) deposited at 450°C.	110
Fig.4.10.	AFM images of BiVO ₄ films deposited on Si and annealed at 400°C: (a) deposited at RT and (b) deposited at 450°C.	110
Fig.4.11.	XRD patterns of BiVO ₄ films sputtered at various Ar/O ₂ mixed ambient (inset: thickness variation with oxygen pressure).	112
Fig.4.12.	SEM images of BiVO ₄ films on BK7. a) O ₂ =10% and b) O ₂ =2% deposited at 550 °C.	113
Fig.4.13.	XRD patterns of BiVO ₄ thin films deposited at different substrate temperatures (inset: magnification of peak at 18.8°).	113
Fig.4.14.	SEM micrographs of BiVO ₄ thin films deposited at different substrate temperatures. a) 350°C, b) 450°C, c) 550°C, d) 600°C and 2D and 3D AFM images of film deposited at 550 °C.	114
Fig.4.15.	FE-SEM cross sectional micrographs of BiVO ₄ thin films deposited at different substrate temperatures.	116
Fig.4.16.	Film growth rate at different substrate temperatures.	117
Fig.4.17.	UV-Visible absorption spectrum of a BiVO ₄ thin film obtained by rf-sputtering on glass substrate under Ar. a) deposited at RT and b) deposited at 450 °C (inset: (αhν) ² vs photon energy plot).	117
Fig.4.18.	UV-Visible absorption spectrum of a BiVO ₄ thin film obtained by rf-sputtering with different oxygen pressure percentage (inset: (αhν) ² vs photon energy plot).	118
Fig.4.19.	UV-Visible absorption spectrum of a BiVO ₄ thin film obtained by rf-sputtering on BK7 substrate under Ar+O ₂ atmosphere (inset: (αhν) ² vs photon energy plot).	119

Fig.5.1.	General Mechanism of photocatalysis.	123
Fig.5.2	Degradation of methyl parathion using TiO ₂ .	124
Fig.5.3.	Changes in UV-Vis spectra of BiVO ₄ particles dispersed in Rh6 solution as a function of irradiation time.	124
Fig.5.4.	Photodecomposition of Rh6 dye and decolorization efficiency of BiVO ₄ C and C ₀ refers to the concentration of the dye Rh6 at time (t) and at initial time respectively.	125
Fig.5.5.	Absorption change of Rh6 solution undergoing a photocatalytic process with ball milled BiVO ₄ photocatalyst. (a) 6hA10:1, (b) 11hA10:1 and (c) 16hA5:1.	126
Fig.5.6.	Photodegradation of Rh6 in aqueous dispersions under visible light irradiation for different BiVO ₄ ball milled samples (inset Rh6 removal percentage vs time of ball milled samples).	127
Fig.5.7.	Changes of UV-Vis spectra of 6hA10:1 BiVO ₄ particles suspended MB solution as a function of irradiation time.	128
Fig.5.8.	Photodegradation of MB in aqueous dispersions under visible light irradiation for different time ball milled BiVO ₄ samples (inset MB removal percentage vs time of ball milled samples).	129
Fig.5.9.	Photocatalytic pseudo-first-order kinetics of 6hA10:1, 11hA10:1 and 16hA5:1. (A) Rh6 and (B) MB. (inset: photodegradation rate constant for different ball milled BiVO ₄ powders).	130
Fig.5.10.	Photodegradation of MB in aqueous dispersion under visible light irradiation for BiVO ₄ films deposited at different T _{sub} using USP technique.	131
Fig.5.11.	Photocatalytic pseudo first order kinetics of BiVO ₄ films deposited at different T _{sub} using USP method for the degradation of MB under visible light irradiation (inset: photodegradation rate constant for different Tsub deposited USP thin films).	132
Fig.5.12.	Absorption spectra of Rh6 solution in the presence of rf-sputtered BiVO ₄ thins films obtained in Ar atmosphere A) RT deposited film and B) 450°C deposited film.	133
Fig.5.13	Photocatalytic degradation of Rh6 for Ar atmosphere rf-sputtered BiVO ₄ thin films (inset: kinetic fit for Rh6 dye degradation with RT and 450°C rf-sputtered films).	133
Fig.5.14.	Photodegradation of Rh6 in aqueous dispersions under visible light irradiation on BiVO ₄ thin films deposited with different T _{sub} under Ar+O ₂ atmosphere (inset: Rh6 removal percentage vs time for different T _{sub} rf-sputtered films).	135

Fig.5.15.	Photocatalytic pseudo first order kinetics of BiVO ₄ films deposited at different T _{sub} by rf-sputtering for the degradation of Rh6 under visible light irradiation.	136
Fig.5.16.	XRD patterns of BiVO ₄ film deposited at 550 °C before and after the photocatalytic study.	137
Fig.5.17.	SEM surface images of 550 °C rf-sputtered BiVO ₄ film. (a) before (b) after photocatalytic study.	137

Abbreviations

Acronym	Definition of Acronym
μF	Microfarad
μm	Micrometer
AFM	Atomic force microscopy
Ar	Argon
Au	Gold
Bi	Bismuth
$\text{Bi}(\text{NO}_3)_3 \cdot 5\text{H}_2\text{O}$	Bismuth nitrate penta hydrate
Bi_2O_3	Bismuth oxide
$\text{Bi}_2\text{O}_3 \cdot n\text{MoO}_3$	Bismuth molybdate
Bi_2SiO_5	Bismuth silicate
Bi_2WO_6	Bismuth tungstate
BiOI	Bismuth oxyiodide
BiVO_4	Bismuth vanadate
BPR	Ball to powder weight ratio
CASTEP	Cambridge serial total energy package
CB	Conduction band
CdS	Cadmium sulfide
CdSe	Cadmium selenide
CdTe	Cadmium telluride
C_g	Grain capacitance
C_{gb}	Grain boundary capacitance
CO_2	Carbon dioxide
Cu	Copper
Cu_2O	Cuprous oxide
D	Crystallite size
d	d-spacing
DFT	Density functional theory
DRT	Distribution of relaxation time
EDAX	Energy dispersive analysis of X-rays
E_g	Band gap
EPR	Electron paramagnetic resonance
eV	Electron volt
Fe_2O_3	Ferric oxide
FE-SEM	Filed emission scanning electron microscopy
FFT	Fast Fourier Transform
FT-IR	Fourier transform infrared

FWHM	Full width half maximum
g	Lande g-factor
GaAs	Gallium arsenide
GGA	<i>Generalized gradient approximation</i>
h	Hour
HF	High frequency
HN	Havriliak-Negami
HNO ₃	Nitric acid
HR-TEM	High resolution transmission electron microscopy
HTAB	Hexadecyltrimethyl ammonium bromide
HT-XRD	High temperature X-ray diffraction
IF	Intermediate frequency
InP	Indium phosphide
JCPDS	Joint committee on powder diffraction standards
k	Boltzmann constant
K	Kelvin
K _{app}	Reaction rate constant
LF	Low frequency
MA	Mechanical alloying
MB	Methylene blue
mbar	Milli bar
MO	Methyl orange
N	Nitrogen
NC	Nanocrystalline
NH ₄ VO ₃	Ammonium metavanadate
nm	Nanometer
NP	Nanoparticles
OA	Oleic acid
°C	Degree celcius
OL	Oleylamine
PC	Photocatalyst
Pt	Platinum
PVA	Polyvinyl alcohol
PVP	Polyvinyl pyrrolidone
QD	Quantum dot
rf	Radio frequency
R _g	Grain resistance
R _{gb}	Grain boundary resistance
Rh6	Rhodamine 6G
RPM	Rotation per minute

SDS	Sodium dodecyl sulfate
SiO ₄	Silicate
SnO ₂	Tin dioxide
T	Temperature
T _c	Critical temperature
TiO ₂	Titanium oxide
T _{sub}	Substrate temperature
USP	Ultrasonic spray pyrolysis
UV-VIS	Ultraviolet visible
V	Vanadium
V ₂ O ₅	Vanadium oxide
VB	Valance band
VBM	Valence band maximum
VO ₄	Vanadate
W	Watt
WO ₃	Tungsten trioxide
XRD	X-ray diffraction
Z'	Real part of impedance
Z''	Imaginary part of impedance
ZnO	Zinc oxide
ZTO	Zinc tin oxide
α and β	Phenomenological parameter
δ	Dislocation density
ε	Strain
ε*	Complex dielectric function
'	Real part of dielectric function
"	Imaginary part of dielectric function
σ _{dc}	dc conductivity
τ _{max}	Relaxation time
ω	Frequency
Ω	Ohm

Abstract

Degradation of harmful organic pollutants using semiconducting materials has been considered as one of the vital solution for wastewater treatment. The major drawback of extensively used photocatalysts such as TiO_2 , ZnO and SnO_2 is that they are active under UV illumination due to their wide band gap (~ 3.2 eV), and hence capable of absorbing only 5-7% of the solar spectrum. To overcome this hurdle, visible light-driven bismuth vanadate (BiVO_4) photocatalyst has been developed in recent years due to its narrow band gap (~ 2.3 eV), crystalline structure and visible light response (43% of the solar spectrum). This dissertation is an exhaustive attempt towards synthesis of BiVO_4 powders in micro and nanoscale sizes using hydrothermal and mechanochemical processes as well as deposition of BiVO_4 thin films using ultrasonic spray pyrolysis (USP) and rf-sputtering techniques. The experimental parameters were optimized and tuned for both powder and thin films to obtain monoclinic scheelite phase of BiVO_4 . The crystalline phase, degree of crystalline order, morphology, surface states, spectral absorption range and oxygen vacancies were evaluated using different characterization techniques and it is well-correlated with the photocatalytic efficiency.

Controlled morphologies and well-crystallized monoclinic scheelite phase of BiVO_4 powders were synthesized using hydrothermal process by varying pH and surfactants. In the absence of surfactants, spherical nanoparticles were formed at neutral pH while in the presence of surfactant (i.e. oleylamine), microentities and acicular morphologies were obtained at pH 2 and 9, respectively. Mechanochemical ball milling process was also employed for obtaining monoclinic BiVO_4 nanostructured powders by optimizing experimental parameters such as milling time (6 h) and balls to powder weight ratio (10:1). Further, crystallinity of BiVO_4 powder was enhanced by annealing at 450°C which is confirmed by sharp and well-resolved XRD peaks. Such ball milled powders were further investigated for electrical conductivity, dielectric and mixed oxidation states of Vanadium (V^{5+} , V^{4+}) ions using EPR spectroscopy. It is worth noting that as compared to hydrothermal process, ball milling is far more efficient, reproducible, economically effective, less tedious and environmental friendly technique.

BiVO_4 thin film deposition was another endeavor which was performed using USP (non-vacuum) and rf-sputtering (vacuum) techniques. Polycrystalline monoclinic BiVO_4 thin films were deposited using even more cheaper, simpler, quite efficient and environmental friendly USP method which showed an increase in crystallinity and particle size (29 to 37 nm) with increasing substrate temperature (300° to 500 °C at an interval of 25 °C). Thin films deposited at 425 °C exhibited a narrow band gap (2.09 eV), thus leading to enhanced absorption in the visible region. In order to compare the photocatalytic performance of BiVO_4 thin films were also prepared by rf-sputtering. The experimental parameters such as chamber atmosphere (argon and argon/oxygen mixture), rf powers (25 and 50 W) and substrate temperatures (RT, 350°, 450°, 550° and 600 °C) were varied for fine-tuning the morphology (nanocrystalline-like, flat surface, autumn leaves-like and beads in a row-like), crystallinity, crystalline size (20-100 nm), thickness (653 to 455 nm), orientation of grains (28.8° to 18.8°) and optical energy band gap (2.29 to 2.68 eV) of sputtered thin films.

Finally, photocatalytic activity of as synthesized powders and thin films were evaluated for the degradation of rhodamine 6G (Rh6) and methylene blue (MB) under visible light irradiation. Hydrothermally prepared acicular BiVO_4 powders showed 86% removal of Rh6 under visible light illumination for 240 min. Mechanochemically synthesized 6 h milled sample with 10:1 ball to powder ratio (BPR) showed 97% removal of Rh6 under visible light illumination of 150 min. The photocatalytic efficiency of ball milled sample was 50% more as compared to hydrothermally prepared BiVO_4 powder. The photodegradation of MB for USP deposited thin films at T_{sub} of 425°C was found to be 66% in 120 min of illumination. BiVO_4 thin films prepared under Ar atmosphere by RF-Sputtering at RT (18 nm particle size) had 96% removal of Rh6 in 240 min while thin films prepared under Ar/O₂ atmosphere showed 99% removal in the same time span. Porosity, thickness and morphology of the films, significantly enhances the photodegradation activity. Thus, BiVO_4 nanostructures can be demonstrated as an efficient photocatalyst for degradation of organics as compared to existing materials with promising applications notably in preserving the environment.

1. General Introduction

Clean water is one of the most important natural resources for human, animals and plants in the world. With the rapid development of industries like chemical, petrochemical, pharmaceutical, mining, semiconductor and microelectronic, around the world the need for pure water as well as purification of contaminated water has increased. Each of these industries requires large quantity of water for processing and subsequently water discharged from them are contaminated with toxic organic pollutants. In addition, the increasing population of the world is also escalating the need of pure water for domestic purpose. The high population density and the level of industrialization have triggered the hydrosphere to be polluted with inorganic and organic matter with an increasing rate. Decades of untreated obnoxious waste disposed off in the land have created a serious ground water contamination problem due to metal leaching in water. Remediation of such a contaminated soil is an expensive process and it is highly unlikely that developing countries will have enough resources to ensure sufficient clean water reserve.

The other major problem of the world is energy crisis that needs to be circumvented by solar energy conversion technologies and hydrogen energy generation. Rising energy demands and dwindling fossil fuel stocks have enforced the whole scientific community to look for other sources and especially solar energy and hydrogen energy. There is an urgent need to divert a flurry of attention towards new materials such as semiconductors, which can convert abundant solar energy into electrical or chemical energy. Both energy crisis and water problems can be conquered over by stringent environmental regulatory acts. This has consequently led to the generation of efficient technologies superseding conventional ones for the treatment of industrial wastewaters and contaminated clean water resources [1, 2]. Semiconductor photocatalysts have created a revolution in waste water treatment technologies, thus attesting to be instrumental in removal of obnoxious compounds and splitting water for hydrogen production. They are capable of surmounting two global problems of the whole world i.e. “Energy and Water” as part of an answer to the question raised by Professor Richard E. Smalley in 2002-2003 [3] *‘What will be the Top ten Problems facing the World for next 50 years?’* (Fig.1.1). Photocatalysts are playing an



Fig.1.1. Human being top ten problems for next 50 years.

important role in water splitting for clean energy sources, degradation of organic pollutants and waste water treatment [4]. Particularly, with waste water treatment, semiconductor photocatalytic processes have shown a great potential as a low-cost, environment friendly, and sustainable treatment technology, to align with the “zero” waste scheme in drinking water/wastewater industry [4].

1.1. Choice of photocatalyst and BiVO₄

Semiconducting materials have attracted much attention in the past decades due to their optical, electrical, magnetic, mechanical and catalytic/photocatalytic properties [5, 6]. They are also evidenced to be attractive candidates for solar energy applications, which include photovoltaic, photoelectrochemical and photocatalytic remediation [5, 6]. Selection of such multifaceted material is really a difficult task. The desirable properties of semiconductors that determines their use in solar energy applications are listed below,

- Optical energy gap (favorable to have absorbance in visible region of solar spectrum).
- Electronic properties (higher life time of charge carriers and effective charge separation).
- Relevant positions of conduction and valence band edges with respect to reduction potentials of the substrate of interest.
- Generation of highly reducing and oxidizing species at the semiconductor/medium interface.
- Chemically inert and stable and photochemical stability in aqueous solutions.

Fig.1.2 shows the band gap distribution of some important semiconducting materials, which are likely candidates for photocatalytic applications. The widely used photocatalysts (Fig.1.2) generally include metal oxide or sulfide semiconductors such as TiO₂ [7, 8], ZnO [9, 10], Cu₂O

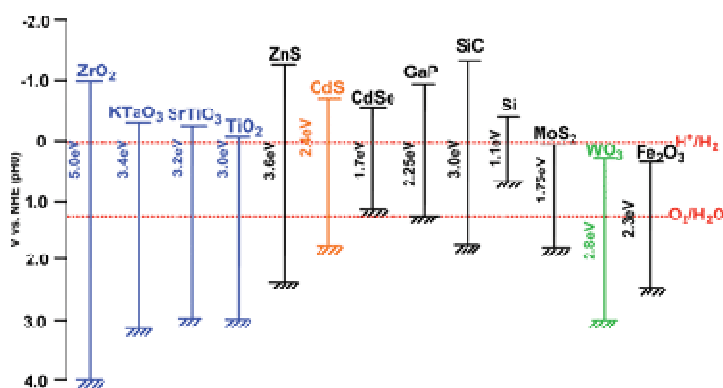


Fig.1.2. Band gap distribution of some semiconductors (Reproduced from ref.27).

[11, 12], CdS [13], Fe₂O₃ [14], SnO₂ [15], WO₃ [16, 17] and Bi₂WO₆ [18]. Photoelectrochemical water splitting using TiO₂ has been already established by Fujishima-Honda [19] and is proved to be responsible for diverting a flurry of attention towards photocatalysis [20, 21], solar cells [22, 23] and gas sensors [24, 25]. Non-oxide semiconductors namely, gallium arsenide (GaAs), indium phosphide (InP), cadmium telluride (CdTe) and cadmium selenide (CdSe) are also used for the same photoelectrochemical applications. However, they suffer from serious drawbacks such as low band gap, unstable in water upon illumination (e.g. CdS and CdSe) and toxicity.

Large numbers of traditional photocatalysts (TiO₂, ZnO, and SnO₂) are active only in the ultraviolet region due to their wide band gap (~3.0 to 3.4 eV) and they are capable of absorbing only 5-7% of the solar spectrum. In semiconductor oxides, the deep valence bands are formed by O2p orbital, which is a critical parameter on the band gap value [26]. To narrow down the band gap, it is indispensable to control the valence band with other elements instead of O2p orbital. Therefore, utilization of visible region which constitutes ~43% of the solar spectrum, can play a vital role for enhancing photocatalytic performance. Kudo *et al* [26] reported that bismuth is a potential candidate for such a valence band controlling element. In this context, Bismuth Vanadate (BiVO₄) has attracted much interest due to its unique properties namely oxygen evolution by photoelectrochemical water splitting [27], photocatalytic degradation of harmful pollutants [28], non-toxic yellow pigment, ferroelasticity, ionic conductivity and environmentally attractive “green” substitutes for lead, chromium and cadmium based paints [29].

1.2. Features of BiVO₄

1.2.1. Crystal polytypes and optical properties

Since the first report on preparation of bismuth vanadate crystals in 1925 [30], a tremendous effort has been made to synthesize monoclinic BiVO₄ due to its fascinating properties especially related to structural changes. It is reported that BiVO₄ mainly exists in three crystalline phases: tetragonal zircon (pucherite), monoclinic scheelite (distorted scheelite, clinobisvanite), and tetragonal scheelite (dreyerite) structure [31]. The orthorhombic phase occurs naturally as the pucherite mineral. The tetragonal zircon-type structure can be formed by low temperature synthesis, while at higher temperatures monoclinic structure is obtained. The monoclinic form undergoes a reversible transformation to tetragonal scheelite by heating above 255 °C. The tetragonal structure also transforms irreversibly to monoclinic form by mechanical treatment (e.g., grinding with an agate mortar and pestle) [32]. Tetragonal BiVO₄ (~2.9 eV band gap) mainly possesses an UV absorption band, while monoclinic scheelite BiVO₄, (~2.3 eV band gap) shows both visible-light and UV absorption. The UV absorption observed in both the tetragonal and monoclinic BiVO₄ is associated to band transition from O2p to V3d, whereas visible light absorption is due to the transition from a valence band (VB) formed by Bi6s or a hybrid orbital of Bi6s and O2p to a conduction band (CB) of V3d [33]. In addition, the Bi-O bond in monoclinic BiVO₄ is distorted, which increases the separation efficiency of photo-induced electrons and holes [34, 35].

1.2.2. Numerical simulation of crystal and electronic band structures of BiVO₄

Theoretical studies are necessary for the better understanding of how solid structures of BiVO₄ in different phases influence the electronic and photocatalytic properties. The calculations were performed using density functional theory (DFT) as implemented by Cambridge Serial Total Energy Package (CASTEP) [36] code. Figure 1.3 (a) depicts the unit cell structure of monoclinic BiVO₄ (Clinobisvanite) with the point group C_{2h}⁶ and space group: C_{2/c}. Basic unit structure consists of a VO₄ tetrahedron and a BiO₈ polyhedron. Four oxygen atoms surround V site, and eight oxygen atoms surround Bi site [37]. VO₄ tetrahedron is connected to BiO₈ by sharing an apex oxygen atom. Bi and V atoms are arranged alternately along the crystallographic axis, making monoclinic BiVO₄ to exhibit the characteristics of a layered structure [37]. The

calculated band structure and density of states are shown in Fig 1.3 (b) and (c) respectively. The calculated GGA band gap is 2.02 eV, which is about 0.28 eV lower than the experimental value. These features of pure BiVO_4 are consistent with reported DFT calculations [38, 41]. The valence bands are mainly composed of $\text{O}2p\text{-V}3d$ and $\text{O}2p\text{-Bi}6p$ and the bottom conduction bands are mainly composed of anti-bonding states.

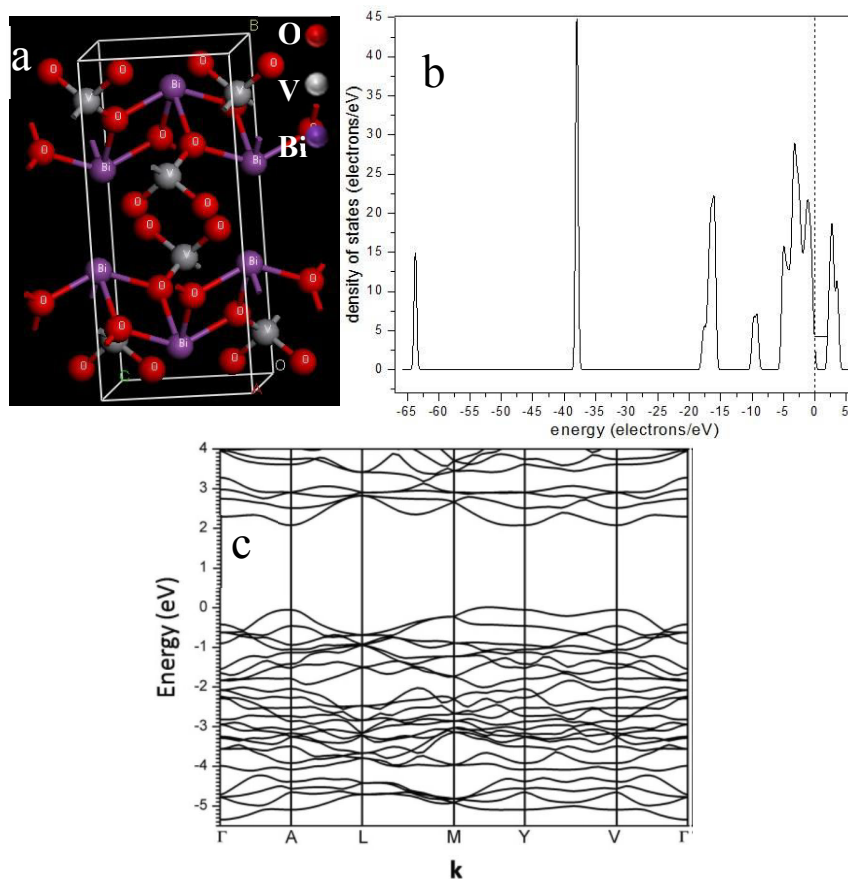


Fig.1.3. Crystal structure of monoclinic BiVO_4 . (a) Conventional unit cell. (b) Density of states. (c) Band structure.

The lone pair $\text{Bi}6s$ orbital also couples with the $\text{O}2p$ orbital and produces filled anti-bonding states near the VBM (Valence Band Maximum). Such coupling makes BiVO_4 a direct band gap at point A (Fig.1.3(c)) as compared to other conventional semiconductors, which makes a band gap at point A . ② Four types of bond lengths are present for Bi-O bond, and two types for V-O bond, and are shown in table 1.1. The different types of bond lengths indicate that both VO_4 and

BiO₈ polyhedra are slightly distorted [42]. This distortion enhances the lone pair impact of Bi 6s states, and disperses the VB (Valence band) upwards resulting in a reduced band gap. As a result, electrons can be excited by visible light the physical and structural parameters of monoclinic BiVO₄ phase are in table 1.1

Table 1.1. Bond length of monoclinic BiVO₄.

Crystal system	Bond length (Å)	
	Bi-O	V-O
Monoclinic	2.354 x 2	1.69 x 2
	2.372 x 2	1.77 x 2
	2.516 x 2	
	2.628 x 2	1.72 x 4

1.3. Basic concept of photocatalysis Every chemical reaction occurs only when a molecule is

Table 1.2. Physical and structural parameters of monoclinic BiVO₄.

Formula	BiVO₄
Synonyms	Bismuth orthovanadate; Bismuth vanadate. Vanadic acid, Bismuth salt
Appearance and odor	Yellow, Very soft.
Molecular weight (g/mol)	323.92
Melting point (°C)	934
Boiling point (°C)	1997
Solubility in water	Insoluble, soluble in strong acids
Structure	Monoclinic, tetragonal
Combustibility	Non-combustible
Stability	Stable under normal condition
Density (g/cm ³)/(g/mL)	6.95
Band gap (eV)	2.4 (m-BiVO ₄), 2.9 (t-BiVO ₄)
Specific gravity (gm/cc)	6.98
Crystal structure	Monoclinic
Cell parameters (Å)	a = 5.195 b = 11.701 c = 5.092, β = 90.38

provided with the necessary activation energy. A simple example is the combustion of hydrocarbons into carbon dioxide and water. In this reaction, the activation energy is provided in the form of heat or a spark. When activation energy is provided in the form of light then the reaction is known as photochemical reaction. Photochemistry, a sub-discipline of chemistry, is related to the study of interactions between atoms or molecules with light

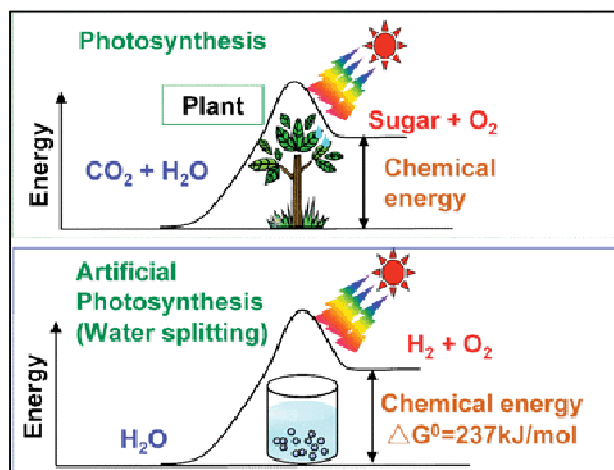


Fig.1.1. Photosynthesis by green plants and photocatalytic water splitting as an artificial photosynthesis (reproduced from ref.27)

. In our day-to-day life many important processes involve photochemistry. The foremost example is photosynthesis (Fig.1.4), in which most plants use sunlight to convert carbon dioxide and water into glucose and release oxygen as a byproduct. This conversion from solar energy to chemical energy is analogous to photosynthesis in green plants, both resulting in an uphill Gibbs free energy change. Therefore, photocatalytic water splitting is also considered as artificial photosynthesis [42, 43].

From past decade, many researchers have studied the photocatalytic mechanism of BiVO_4 extensively. Since BiVO_4 is a semiconductor with a narrow band gap of $\sim 2.3 \text{ eV}$, visible-light can excite an electron from valance band to conduction band resulting in the generation of electron hole pairs. The photogenerated electrons then react with molecular oxygen (O_2) to produce superoxide radical anions ($\bullet\text{O}_2^-$), and the photogenerated holes react with water to produce hydroxyl ($\bullet\text{OH}$) radicals. These two reactive radicals act together to decompose organic

compounds. For an efficient semiconductor photocatalyst, the different interfacial electron processes involving e^- and h^+ must compete effectively with the major deactivation processes involving (e^-, h^+) recombination, which may occur in the bulk or at the surface of the material (Figure 1.5). In principle, a semiconductor photocatalyst should be chemically and biologically inert, photocatalytically stable, easy to produce and to use, easily activated by sunlight, able to efficiently catalyze reactions, cheap and should not cause any risk for the environment or to humans.

1.3.1. State of art oxide and non - oxide based semiconductor photocatalysts

Semiconductor-based photocatalysts have attracted much attention in recent years because of their abundance, stability in aqueous media and tunable optical and electrical properties for solving energy and environmental problems [43]. TiO_2 is a widely known semiconducting photocatalyst having a band gap of 3.2 eV but it also suffers from limitation in its efficiency since it absorbs very narrow UV radiation in the solar spectrum [44]. Quantum efficiency can be enhanced only by augmenting the absorption of solar spectral range. This can be achieved notably by doping the material with suitable elements, which will induce intermediate levels in the band gap [45].

An alternative approach can be demonstrated with the use of photoactive titanium oxide based gels [46]. The photocatalytic activity can further be improved by co-catalyst immobilization [47, 48]. Jiang *et al* [49] recently showed that vacancies near the hydrogenation-disordered (at low temperature) surface can enhance photocatalytic activity of TiO_2 through charge carrier trapping and prevention of recombination. Consequently Leshuk *et al* [50]

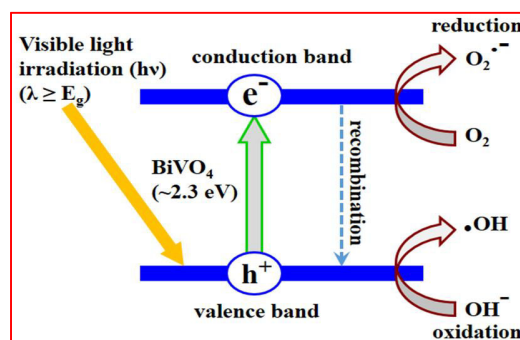


Fig.1.6. A schematic illustration of the generation of electron-hole pairs and the corresponding redox reactions taking place on the semiconductor surface.

reported that high-temperature hydrogenation, can serve to degrade the photocatalytic performance due to bulk vacancy defects. So, alternative synthesis and hydrogenation strategies

must be explored in order to generalize and advance the promising photocatalytic results. TiO_2 has been reported to decompose water without any additional external voltage. In contrast, hydrogen can evolve more efficiently from aqueous solutions containing organic materials, which include methanol, ethanol, or formic acid as reducing agents. Besides such organic materials, inorganic ions (sulfite or sulfide) are also reported to be able to serve as sacrificial reducing agents [51, 52].

Iron oxide (Fe_2O_3) in α , β , γ and amorphous forms has been recognized as attractive photocatalyst because it is stable, safe and inexpensive [53]. However, only α - Fe_2O_3 has usually been used as a photocatalyst [54]. Due to the short diffusion length of photogenerated carriers, photocatalytic degradation characteristics of α - Fe_2O_3 semiconductor showed mainly particle size dependent performance [55]. Recently, Gratzel *et al* [56] substantiate particle size (10 to 20 nm) dependent photocatalytic oxidation of water by dendritic α - Fe_2O_3 . Particle size dependent photocatalytic activity for WO_3 was also confirmed by Serpone [57] and Xu *et al* [58].

Zinc oxide (ZnO) has been proved as a promising photocatalytic material for the degradation of organic contaminants. One-dimensional ZnO nanorods combined with highly porous ceramic substrates were found to enhance the photocatalytic activity. Comparative studies on methyl orange (MO) degradation under UV light demonstrated that porous ceramic supports were 58% more active than polyester fiber membranes [59]. Also, zinc stannate (ZTO), is a ternary oxide semiconductor with a wide band gap (~ 3.6 eV) that has been used for the degradation of organic pollutants. ZTO is chemically stable and has high electron mobility essential for enhanced photocatalytic performance. The photocatalytic activity could be further enhanced by another 19% by coupling ZTO islands to ZnO nanorods. This enhancement in photocatalytic activity was attributed to an increase in charge separation due to the coupling of two oxides of different band gaps, leading to reduced electron-hole pair recombination and efficient transfer of electrons through the exposed ZnO nanorod surfaces [60].

Wang and Costi [61, 62] have reported efficient photocatalytic activity of TiO_2 nanoparticles (NP) by using gold (Au) as co-catalyst. Varghese *et al* [63] investigated the influence of plasmons induced in Au NPs on photoactivity of Fe_2O_3 electrodes. Recent reports on hybrid nanocomposites (Graphene with metal oxide semiconductors) were used to reduce the recombination process and hence to improve the photocatalytic performance by delocalizing the

photogenerated electron through graphene π network [64, 67]. Photodegradation of toluene over a spindle-shaped α -Fe₂O₃/graphene oxide composite was also studied by Li *et al* [68].

Compared to oxide semiconductors (TiO₂ and ZnO), Cadmium selenide (CdSe) quantum dots have broad absorption spectra with a first absorption and emission peak spanning a wide range of wavelengths in the visible region. It is reported that there will be an extension of visible region absorption upon increase in the particle size. Liu *et al* [69] reported that 3-mercaptopropionic acid capped CdSe QDs are capable enough for the photodegradation of cephalexin under UV irradiation. Cadmium sulfide (CdS) is another illustrious photocatalyst in quantum dot forms with the band-gap energy of 2.4 eV, well suitable for the solar spectrum absorption. It is also reported that incorporation of graphene into CdS increases the crystallinity and surface area of the CdS which yields 22.5% efficiency for hydrogen production. Li *et al* [70] found that the optimum percentage of graphene incorporation in CdS was 0.05%. Zi *et al* [71] demonstrated morphology, prolonged lifetime of charge carriers and surface area dependent photocatalytic activity for alcohol oxidation on CdS and CdS/titanate nanotube. However, CdS was found to be unstable in aqueous solutions under irradiation due to photocorrosion. Furthermore, it was also proved that the photocatalytic activity of individual CdS is not efficient enough to oxidize an alcohol.

It was widely reported that charge transfer against recombination can be effectively achieved by the fluorination of semiconductor photocatalysts [72]. The absorbed fluorine on the surface of semiconducting photocatalyst can act as electron trap due to higher electronegativity of fluorine than that of hydroxyl group. The improvement of photocatalytic activity was also observed over fluorinated TiO₂ [73], SrTiO₃ [74], ZnWO₄ [75] and Bi₂WO₆ [76] semiconductors.

1.3.2. Photocatalytic properties of bismuth based semiconductors

Bismuth oxy-iodides belong to the main group V-VI-VII ternary semiconductors with layered crystal structures. Till now five different bismuth oxy-iodide compounds are reported, viz., BiOI, Bi₄O₅I₂, α -Bi₅O₇I, β -Bi₅O₇I, and Bi₇O₉I_{3b} [77]. Among them, BiOI has been widely studied as a photocatalyst [78, 79]. Bismuth tungstate (Bi₂WO₆), one of the simplest members of aurivillius oxide family, has a crystal structure composed of accumulated layers with alternating bismuth oxide (Bi₂O₂)²⁺ layers and octahedral (WO₄)²⁻ sheets. The layered structure is favorable for charge transfer, and thus, Bi₂WO₆ exhibits excellent photocatalytic activity under visible light

irradiation [80, 81]. The optimum photocatalytic activity of 0.5C₃N₄-0.5Bi₂WO₆ heterojunction for the degradation of Methyl Orange (MO) was almost 3 and 155 times higher than that of individual C₃N₄ and Bi₂WO₆, respectively.

Bismuth molybdates have general chemical formula Bi₂O₃·*n*MoO₃ where *n* = 3, 2 or 1, corresponding to α-Bi₂Mo₃O₁₂, β-Bi₂Mo₂O₉, and γ-Bi₂MoO₆ respectively [82]. The photocatalytic investigation indicates that γ-Bi₂MoO₆ constituted by a layered structure with corner-shared MoO₆ units has shown excellent photocatalytic activity under visible light irradiation [83]. However, it was reported that β phase of Bismuth molybdate cannot be prepared by direct hydrothermal method. But later, hydrothermally synthesized bismuth molybdate (Bi₂MoO₆) nanostructures with different morphologies were achieved by Guo *et al* [84] for potential application in the removal of sulfamethazine (SMZ) from wastewater. The new bismuth silicate (Bi₂SiO₅) within Aurivillius family [85, 87] has been also reported as a promising photocatalyst. Dai's research group [88] synthesized single crystalline Bi₂SiO₅ nanosheets, but could not unravel the mechanism of photodegradation. However, this group reported that the distorted SiO₄ tetrahedron structure in Bi₂SiO₅ may be favorable for separating photogenerated carriers, which could improve its photocatalytic activity. Though few investigations have been performed on the synthesis and photocatalytic activity of Bi₂SiO₅, the as-prepared structure was usually associated with Bi₂O₃ phase, which is easy for the formation of polycrystallinity, thus seriously decreasing the photocatalytic performance of Bi₂SiO₅ [89, 94].

Bismuth titanate is a wide band gap semiconductor that includes several phases of Bi-O-Ti system. Yao *et al.* [95] demonstrated that nano-sized Bi₄Ti₃O₁₂ prepared by chemical solution decomposition method showed high photocatalytic activity to photodegrade 10 ppm methyl orange (MO) solution in 4 h under UV irradiation. Hou *et al* [96] reported that Bi₄Ti_{2.6}Cr_{0.4}O₁₂ nanosheets obtained by hydrothermal process with high stability showed highest photocatalytic performance leading to evolution of H₂ from water under visible-light irradiation. It is believed that the Bi6s and O2p levels can form a wide dispersed hybridized valence band (VB) [97] which favors mobility of photogenerated holes and oxidation reaction, inducing efficient separation of photogenerated electron-hole pairs and then improving the photocatalytic performance. In particular BiVO₄ is also an important visible light active photocatalyst and has been widely used in the evolution of O₂ and for the degradation of organic pollutants [98].

1.3.3. Synthesis of BiVO₄ - A state of art - BiVO₄ has been prepared with different morphologies by various techniques, such as solid-state reaction [99], aqueous solution method [100], co-precipitation [101, 102], solvothermal method [103], molten salt method [104], sonochemical method [105], microwave irradiation [106], solution combustion method [107], metal organic decomposition [108] and hydrothermal method [109-110]. Microsphere and

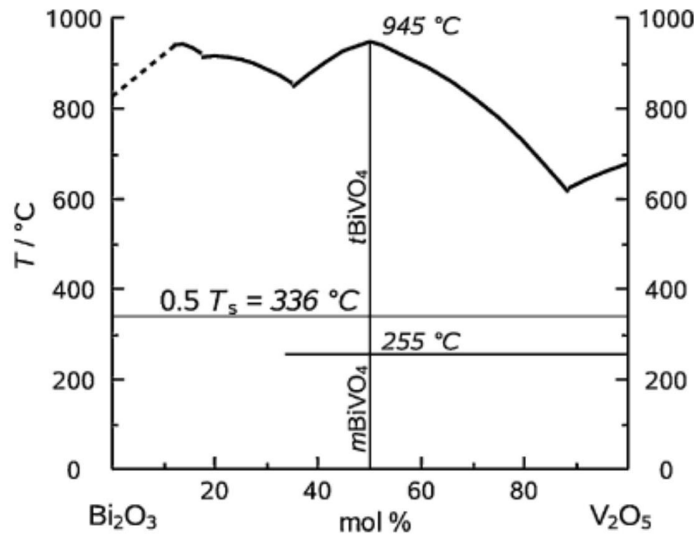


Fig.1.6. Phase diagram of Bi₂O₃-V₂O₅ system (Reproduced from ref.28).

lamellar BiVO₄ powders were selectively prepared through adjustment of hydrothermal temperature by using cetyltrimethyl ammonium bromide (CTAB) as a template directing reagent [111]. Guo *et al* [112] prepared BiVO₄ with various crystal structures and morphologies by tuning hydrothermal treatment time, acidity, and molar ratio of Bi to V in the starting materials. It is found that pH values of precursor solution have great effects on phase and morphology of BiVO₄ powders. With the help of triblock copolymer P123, Meng and co-workers [113] have synthesized the multi-morphology BiVO₄ powders using hydrothermal method by adjusting the pH values. They reported that rod like morphology was capable of degrading methylene blue completely after 3 h of visible-light irradiation. Zhang *et al* [114] studied the photocatalytic degradation of methyl orange over BiVO₄ powders prepared at different pH values. They have reported that sheet-like BiVO₄ prepared at pH 6.9 gave maximum photodegradation activity and the methyl orange degradation was completely achieved after 1 h of visible light irradiation. Bismuth nitrate pentahydrate and ammonium vanadate have been used as precursors to prepare tetragonal BiVO₄ of 1-4 micrometer particle size by solid state reaction. 10-20 nm tetragonal and

monoclinic BiVO₄ nanoparticles have been synthesized by microwave irradiation technique [106]. Molten salt method has been used to prepare monoclinic BiVO₄ nanoparticles of 30 to 52 nm. Strong dependence of band gap energy on nanocrystalline (NC) size has been observed, where band gap increased from 2.37 to 2.46 with a decrease in crystallite size due to quantum confinement effect. However, co-existence of polytypes can contribute to widen the band gap as in the case of BiVO₄ prepared by co-precipitation method, where band gap is in the range of 2.58 to 2.75 eV [115]. There are very few reports on ball milled BiVO₄ as summarized in table 1.3. However, all the reports were dedicated to application of the material as pigment, ceramics and for ferroelasticity behavior. The phase diagram for the Bi₂O₃ and V₂O₅ system were presented in Fig.1.6, which points out the percentage of precursor materials to form BiVO₄ the monoclinic structure.

The co-existence of monoclinic-tetragonal heterostructure appears as a new way to be considered for improving the photocatalytic performance [116]. Recently, Tan *et al* [117] reported a feasible procedure to obtain monoclinic and monoclinic-tetragonal mixtures by controlling the pH of precursors. They demonstrated that existence of a mixed-phase BiVO₄ showed higher photocatalytic activity as compared to pure form. In the same direction, Fan *et al* [118] reported that the particular monoclinic-tetragonal heterostructured BiVO₄ is expected to promote the separation of photo-induced electron-hole pairs. The results clearly revealed that the behavior of photo-induced charge is markedly dependent on BiVO₄ crystalline phases. Likewise, the presence of interface in monoclinic/tetragonal heterophase provides a spatial condition for charge transfer. This favors the separation of photoinduced electron-hole pairs and changes the migration direction of photo induced carriers. Zhang *et al* [119] selectively synthesized BiVO₄ with different crystalline phases. Monoclinic BiVO₄ with a band gap of 2.34 eV showed higher photocatalytic activity than that of tetragonal BiVO₄. Li and co-workers [120] prepared BiVO₄ nanoparticles by molten salt method. There were symmetry distortions in the local structure as evidenced by shifts in Raman peak positions. The variations in local structure contribute to the modification of electronic structure leading to enhancement of visible light photocatalytic activity. Furthermore, Saimi *et al* [121] considered that the distortion of a Bi-O polyhedron by a 6s² lone pair of Bi³⁺ may play an important role in improving the photocatalytic activity of monoclinic BiVO₄ under visible light irradiation. The distortion probably affects the charge separation and delocalization of photogenerated electrons and holes.

Semiconductor photocatalyst in powder form offers the advantage of easy activation of the photocatalyst. However, the powder catalyst has the drawback of post-separation in a slurry system after photoreaction. This can be avoided by using thin films. Thin film processing of BiVO₄ has grown impressively using chemical bath deposition [122], metal organic decomposition [123], citrate route [124], dip coating [125], spray pyrolysis [126] or electrochemical approaches (e.g. electrodeposition) [127, 128] while no reports have been made on rf-sputtering for the synthesis of BiVO₄ thin films.

Table 1.3. Summary of ball milled BiVO₄.

Ball mill type	Precursors	Experimental procedure	Particle size	Application	Remarks
Planetary ball mill [129]	oxides, bismuth nitrate, ammonium vanadate	Heated in platinum crucibles 2 or 3 times to 650 ⁰ C for 10 h and re-ground before the second and third annealing step. After that 12 hr BM		Yellow Pigment	≈32 h
Centrifugal ball mill [130]	Bi ₂ O ₃ & V ₂ O ₅	Heating 770 K and then at 1070 K for 24 h	50 h 2 μm	ferroelectricity	Intermediate grinding
Planetary ball mill [131]	Bi ₂ O ₃ & V ₂ O ₅	Zirconia pot of 45 cm ³ inner volume with 7 zirconia balls of 15.7 mm diameter in air. 700 rpm	200 nm		2 h grinding heating to 500 ⁰ C
Centrifugal ball mill [132]	Bi ₂ O ₃ & V ₂ O ₅	54 h milling	<50 nm	Ceramics	
Planetary ball mill [133]	Bi ₂ O ₃ & V ₂ O ₅	Mill for 16 h. After drying for 12 h at 400 K, obtained powder was ball-milled for 45 min and calcined for 16 h at 1073 K.		ceramics	≈45 h

In summary, various methods of synthesis were carried out to obtain several morphologies and polytypes of BiVO₄. Their electronic and optical properties are highly dependent on synthesis methods, precursors and experimental parameters. Towards this perspective, preparing powders by various techniques namely, hydrothermal and mechanochemical process as well as preparing BiVO₄ thin films by, ultrasonic spray pyrolysis and rf-sputtering technique constituted a relevant strategy for this thesis. The next most important endeavor is to achieve the photocatalytic efficiencies in such as-prepared BiVO₄ powders and thin films after optimizing different parameters during and after synthesis.

References

1. D. W. Chen, A. K. Ray, *Appl. Catalysis B: Environmental*, 1999, 23, 143-157.
2. H. Zhou, D. W. Smith, *Journal of Environmental Engineering Science*, 2002, 1, 247-264.
3. Richard E. Smalley, energy and nanotechnology conference, Rice University, may 3, 2003.
4. M. N. Chong, B. Jin, C. W. K. Chow, C. Saint, *Water Research*. 2010, 44, 2997-3027.
5. K. Rajeshwar, *Journal of Applied Electrochemistry*, 2007, 37, 765-787.
6. K. Rajeshwar, N. R. de Tacconi, *Chemical Society Reviews*, 2009, 38, 1984-1998.
7. A. Fernandez, G. Lassaletta, V. M. Jimenez, A. Justo, A. R. Gonzalez Elipe, J. M. Herrmann, H. Tahiri, Y. Aitichou, *Applied. Catalysis B: Environmental*, 1995, 7, 49-63.
8. C. Minero, E. Pelizzetti, P. Pichat, M. Sega, M. Vincenti, *Environmental Science Technology*, 1995, 29, 2226-2234.
9. L. Gao, L. Q. Jiang, *Mater. Chem. Phys*, 2005, 91, 313-316.
10. M. A. Gondal, K. Hayat, M. M. Khaled, S. Ahmed, A. M. Shemsi, *Appl. Catalysis: A*, 2011, 393, 122-129.
11. W. Z. Wang, H. L. Xu, W. Zhu, *J. Phys. Chem. B*, 2006, 110, 13829-13834.
12. K. Rajeshwar, S. Somasundaram, C. R. N. Chenthamarakshan, N. R. de Tacconi, *Int. J. Hydrogen Energy*, 2007, 32, 4661-4669.
13. A. J. Frank, K. Honda, *J. Phys. Chem*, 1982, 86, 1933-1935.
14. Z. H. Ai, L. R. Lu, J. P. Li, L. Z. Zhang, J. R. Qiu, M. H. Wu, *J. Phys. Chem. C*, 2007, 111, 4087-4093.
15. S. S. Wu, H. Q. Cao, S. F. Yin, X. W. Liu, X. R. Zhang, *J. Phys. Chem. C*, 2009, 113, 17893-17898.
16. M. Ashokkumar, P. Maruthamuthu, *J. Photochem. Photobiol: A*, 1989, 49, 249-258.
17. X. Quan, Y. F. Guo, N. Lu, H. M. Zhao, S. Chen, *Environ. Sci. Technol*, 2007, 41, 4422-4427.

18. H. B. Fu, C. S. Pan, W. Q. Yao, Y. F. Zhu, *J. Phys. Chem. B*, 2005, 109, 22432-22439.
19. A. Fujishima, K. Honda, *Nature*, 1972, 238, 37-38.
20. X. M. Yan, D. Y. Pan, Z. Li, Y. Y. Liu, J. C. Zhang, G. Xu, M. H. Wu, *Mater. Lett*, 2010, 64, 1833-1835.
21. H. J. Zhang, P. P. Xu, G. D. Du, Z. W. Chen, D. Oh K, D. Y. Pan, Z. Jiao, *Nano Res*, 2011, 3, 274-283.
22. J. Li, L. Wang, X. Kong, Ma, B. Y. Shi, C. Zhan, Y. Qiu, *Langmuir*, 2009, 25, 11162-11167.
23. H. E. Wang, L. X. Zheng, C. P. Liu, Y. K. Liu, C. Y. Luan, H. Cheng, Y. Y. Li, Martinu, L. Zapien, J. A. Bello, *J. Phys. Chem. C*, 2011, 21, 10419-10425.
24. K. M. Garadkar, B. S. Shirke, P. P. Hankare, D. R. Patil, *Sens. Lett*, 2011, 9, 526-532.
25. S. Lin, D. Li, J. Wu, X. Li, S. Akbar, *Sens. Actuators, B*, 2011, 156, 505-509.
26. A. Kudo, S. Hijii, *Chem. Lett*, 1999, 1103-1104.
27. A. Kudo, Y. Miseki, *Chemical Society Reviews*, 2009, 38, 253-278.
28. N. C. Castillo, A. Heel, T. Graule, C. Pulgarin, *Applied catalysis B: Environmental*, 2010, 95, 335-347.
29. Mara, A.B. Barata, Marcia, Neves, C. P. Neto, T. Trindade, *Dyes and Pigments*, 2005, 65, 125-127.
30. E. Zintl, L. Varino, L. Process for the manufacture of pure bismuth vanadate. German Patent, 422947, 1925.
31. A.R. Lim, S.H. Choh, M.S. Jang, *Journal of Physics: Condensed Matter*, 1995, 7, 7309-7323.
32. A. K. Bhattacharya, K. K. Mallick, A. Hartridge, *Materials Letters*, 1997, 30, 7-13.
33. Y. H. Ng, A. Iwase, A. Kudo, R. Amal, *J. Mater. Sci. Lett*, 2010, 1, 2607-2612.
34. W. Wang, M. Shang, W. Z. Yin, J. Ren, L. Zhou, *J. Inorg. Mater*, 2011, 27, 11-18.
35. S. Tokunaga, H. Kato, A. Kudo, *Chem. Mater*, 2001, 13, 4624-4628.
36. S. J. Clark, M. D. Segall, C.J. Pickard, P. J. Hasnip, M. J. Probert, K. Refson, M. C. Payne, *Z. Kristallogr*, 2005, 220, 567-570.
37. A. Walsh, Y. Yan, M. N. Huda, M. M. Al-Jassim, S. H. Wei, *Chemistry of Materials*, 2009, 21, 547-551.
38. K. Sayama, A. Nomura, T. Arai, T. Sugita, R. Abe, M. Yanagida, T. Oi, Y. Iwasaki, Y. Abe, H. Sugihara, *J. Phys. Chem. B*, 2006, 110, 11352-11360.
39. Z. Zhao, W. Luo, Z. Li, Z. Zou, *Physics Letters A*, 2010, 374, 4919-4927.
40. K. Ding, B. Chen, Z. Fang, Y. Zhang, *Theor Chem Acc*, 2013, 132, 1352-1358.
41. W. J. Yin, S. H. Wei, M. M. Al-Jassim, J. Turner, Y. Yan, *Physical review B*, 2011, 83, 155102-155111.
42. S. Tokunaga, H. Kato, A. Kudo, *Chemistry of Materials*, 2001, 13, 4624-4628.
43. W. Fan, Q. Zhang, Y. Wang, *Phys.Chem. Chem. Phys*, 2013, 15, 2632-2649.
44. Y. Hau Ng, A. Iwase, A. Kudo, R. Amal, *J. Phys. Chem. Lett*, 2010, 1, 2607-2612.
45. P. Mei, M. Henderson, A. Kassiba, A. Gibaud, *J. Phys. Chem. Solids*, 2010, 71, 1-6.

46. B. Pattier, M. Henderson, A. Poppl, A. Kassiba, A. Gibaud, *J. Phys. Chem B*, 2010, 114, 4424-4431.
47. H. G. Yang, C. H. Sun, S. Z. Qiao, J. Zou, G. Liu, S. C. Smith, H. M. Cheng, G. Q. Lu, *Nature* 2008, 453, 638-U4.
48. J. Pan, G. Liu, G. Q. Lu, H. Cheng, *Angew. Chem., Int. Ed.* 2011, 50, 2133-2137.
49. X. Jiang, Y. Zhang, J. Jiang, Y. Rong, Y. Wang, Y. Wu, C. Pan, *J. Phys. Chem. C* 2012, 116, 22619-22624.
50. T. Leshuk, R. Parviz, P. Everett, H. Krishnakumar, A. Robert, Varin, F. Gu, *ACS Appl. Mater. Interfaces* 2013, 5, 1892-1895.
51. M. Matsumura, Y. Saho, H. Tsubomura, *J. Phys. Chem* 1983, 87, 3807-3808.
52. N. Buhler, K. Meier, J. F. Reber, *J Phys Chem*, 1984, 88, 3261-3268.
53. C. Leygraf, M. Hendewerk, G. A. Somorjai, *J. Phys. Chem*, 1982, 86, 4484-4485.
54. S. Mohanty, J. Ghose, *J. Phys. Chem. Solids*, 1992, 53, 81-91.
55. M. P. Dare-Edwards, J. B. Goodenough, A. Hamnett, P. R. Trevellick, *J. Chem. Soc. Faraday Trans*, 1983, 79, 2027-2041.
56. M. Gratzel, J. Kiwi, L. C. Morrison, *J. Chem. Soc. Faraday Trans*, 1985, 81, 1883-1890.
57. N. Serpone, D. Lawless, R. Khairutdinov, E. Pelizzetti, *J. Phys. Chem*, 1995, 99, 16655-16661.
58. N. Xu, Z. Shi, Y. Fan, J. Dong, J. Shi, M. Z. C. Hu, *Ind. Eng. Chem. Res*, 1999, 38, 373-379.
59. S. Danwittayakul, M. Jaisai, T. Koottatep, J. Dutta, *Ind. Eng. Chem. Res.* 2013, 52, 13629-13636.
60. L. E. Greene, M. Law, D. H. Tan, M. Montano, J. Goldberger, G. Somorjai, P. Yang, *Nano Lett.* 2005, 5, 1231-1236.
61. Wang, R. A. Caruso, *J. Mater. Chem.*, 2011, 21, 20-28.
62. R. Costi, A. E. Saunders, E. Elmalem, A. Salant, U. Banin, *Nano Lett*, 2008, 8, 637-641.
63. O. K. Varghese, M. Paulose, T. J. La Tempa, C. A. Grimes, *Nano Lett*, 2009, 9, 731-737.
64. R. R. Nair, P. Blake, A. N. Grigorenko, K. S. Novoselov, T. J. Booth, T. Stauber, N. M. R. Peres, A. K. Geim, *Science*, 2008, 320, 1308-1308.
65. Q. Huang, S. Tian, D. Zeng, X. Wang, W. Song, Y. Li, W. Xiao, C. Xie, *ACS Catal*, 2013, 3, 1477-1485.
66. Q. P. Luo, X. Y. Yu, B. X. Lei, H. Y. Chen, D. B. Kuang, C. Y. Su, *J. Phys. Chem. C*, 2012, 116, 8111-8117.
67. H. Seema, K. C. Kemp, V. Chandra, K. S. Kim, *Nanotechnology*, 2012, 23, 355705-355712.
68. H. Li, Q. Zhao, Z. Zhu, M. Tade, X. Li, S. J. Liu, *Nanopart. Res*, 2013, 15, 1670-1680.
69. X. Liu, C. Ma, Y. Yan, G. Yao, Y. Tang, P. Huo, W. Shi, Y. Yan, *Ind. Eng. Chem. Res.* 2013, 52, 15015-15023.
70. Q. Li, B. Guo, J. Yu, J. Ran, B. Zhang, H. Yan, J. R. Gong, *J. Am. Chem. Soc.* 2011, 133, 10876-10884.

71. R. Zi, X. Tang, Y. Yin, Y. Zhang, J. Xu, *Inorg. Chem*, 2013, 52, 11758-11766.
72. S. Liu, J. Yu, B. Cheng, M. Jaroniec, *Adv. Colloid Interf. Sci.*, 2012, 173, 35-53.
73. H. Park, W. Choi, *J. Phys. Chem. B* 2004, 108, 4086-4093.
74. J. Wang, S. Yin, Q. Zhang, F. Satio, T. Sato, *J. Mater. Sci*, 2004, 39, 715-717.
75. G. Huang, Y. Zhu, *Phys. Chem. C*, 2007, 111, 11952-11958.
76. R. Shi, G. Huang, J. Lin, Y. Zhu, *J. Phys. Chem. C*, 2009, 113, 19633-19638.
77. X. Xiao, W. D. Zhang, *RSC Adv*, 2011, 1, 1099-1105.
78. L. Q. Ye, L. H. Tian, T. Y. Peng, L. Zan, *J. Mater. Chem*, 2011, 21, 12479-12484.
79. J. X. Xia, S. Yin, H. M. Li, H. Xu, Y. S. Yan, Q. Zhang, *Langmuir*, 2011, 27, 1200-1206.
80. L. Zhang, Y. Zhu, *Catal. Sci. Technol.*, 2012, 2, 694-706.
81. H. Cheng, B. Huang, Y. Dai, X. Qin, X. Zhang, Z. Wang, M. Jiang, *J. Solid. State Chem.* 2009, 182, 2274-2278.
82. L.M. Reilly, G. Sankar, C.R.A. Catlow, *J. Solid State Chem*, 1999, 148, 178-185.
83. H. H. Li, K. W. Li, H. Wang, *Mat. Chem. Phys.*, 2009, 116, 134-142.
84. C. Guo, J. Xu, S. Wang, Y. Zhang, Y. He, X. Li, ***Catal. Sci. Technol***, 2013, 3, 1603-1611.
85. J.Q. Lu, X. F. Wang, C. L. Yu, Y. Q. Xu, *J. Mat. Sc.: Mat. Elec.*, 2012, 23, 1770-1773.
86. H.W. Guo, X.F. Wang, D.N. Gao, *Mat. Lett.*, 2012, 67, 280-282.
87. J.Q. Lu, X.F. Wang, Y.T. Wu, Y.Q. Xu, *Mat. Lett.*, 2012, 74, 200-202.
88. X. J. Dai, Y. S. Luo, S. Y. Fu, W. Q. Chen, Y. Lu, *Solid State Sc.*, 2010, 12, 637-642.
89. Y.T. Fei, S.J. Fan, R.Y. Sun, J.Y. Xu, *J. Mat. Sc. Lett.*, 2000, 19, 893-895.
90. V.P. Zhereb, V.M. Skorikov, *Inor. Mat.*, 2003, 39, S121-S145.
91. O. Rico-Fuentes, E. Sánchez-Aguilera, C. Velasquez, R. Ortega-Alvarado, J.C. Alonso, A. Ortiz, *Thin Solid Films*, 2005, 478, 96-102.
92. V.M. Skorikov, Yu.F. Kargin, A.V. Egorysheva, V.V. Volkov, M. Gospodinov, *Inorg. Mat*, 2005, 41, S24-S46.
93. V.M. Denisov, L.A. Irtyugo, L.T. Denisova, *Phys. Solid State*, 2011, 53, 2180-2182.
94. J. Lu, X. Wang, C. Yu, Y. Xu, *J. Mat. Sci: Mat. Elec*, 2012, 23, 1770-1773.
95. W. F. Yao, H. Wang, X. H. Xu, S. X. Shang, Y. Hou, Y. Zhang, M. Wang, *Mater.Lett*, 2003, 57, 1899-1902.
96. J. Hou, R. Cao, Z. Wang, S. Jiao, H. Zhu, *J.Mater.Chem*, 2011, 21, 7296-7301.
97. W. Wei, Y. Dai, B.B. Huang, *J.Phys. Chem. C*, 2009, 113, 5658-5663.
98. Kohtani, S. Koshiko, M. Kudo, A. Tokumura, K. Ishigaki, Y. Toriba, A. Hayakawa, K. Nakagaki, R. *Appl. Catal., B*, 2003, 46, 573-586.
99. A. Kudo, K. Ueda, H. Kato, *Catal. Lett*, 1998, 53, 229-230.
100. L. Zhou, W. Z. Wang, H. L. Xu, *Cryst. Growth*, 2008, 8, 728-733.
101. H. M. Fan, T. F. Jiang, H. Y. Li, D. J. Wang, L. L. Wang, J. L. Zhai, D. Q. He, P. Wang, T. F. Xie, *J. Phys. Chem. C*, 2011, 116, 2425-2430.
102. D. N. Ke, T. Y. Peng, L. Ma, P. Cai, P. Jiang, *Al. Catal, A*, 2008, 350, 111-117.

103. L. Ren, L. Jin, J. B. Wang, F. Yang, Qiu, Q. Mi. Y. Yu, *Nanotechnology*, 2009, 20, 115603-115611.
104. Y. Liu, J. Ma, Z. Liu, C. Dai, Z. Song, Y. Sun, J. Fang, J. Zhao, *Ceram. Int*, 2010, 36, 2073-2077.
105. L. Zhou, W. Z. Wang, S. Liu, L. Zhang, H. Xu, W. J. Zhu, *Mol. Catal. A, Chem*, 2006, 252, 120-124.
106. Z. Zhang, W. Wang, M. Shang, W. Yin, *Cat. Comm.*, 2010, 11, 982-986.
107. H. M. Zhang, J. B. Liu, H. Wang, W. X. Zhang, H. Yan, *J. Nanopart. Res*, 2008, 10, 767-774.
108. A. Galembeck, O. L. Alves, *J. Mater. Sci.*, 2002, 37, 1923-1927.
109. Y. Zhou, K. Vuille, A. Heel, B. Probst, R. Kontic, G. R. Patzke, *Al. Catal A*, 2010, 375, 140-148.
110. A. P. Zhang, J. Z. Zhang, *Al. Surf. Sci*, 2010, 256, 3224-3227.
111. D. N. Ke, T. Y. Peng, L. Ma, P. Cai, K. Dai, *Inorg. Chem*, 2009, 48, 4685-4691.
112. Y. Guo, X. Yang, F. Ma, K. Li, L. Xu, X. Yuan, *Al. Surf. Sci*, 2010, 256, 2215-2222.
113. X. Meng, L. Zhang, H. Dai, Z. Zhao, R. Zhang, Y. Liu, *Mater. Chem. Phys*, 2011, 125, 59-65.
114. A. P. Zhang, J. Z. Zhang, N. Y. Cui, X. Y. Tie, Y. W. An, L. Li, *J. Mol. Catal. A, Chem*, 2009, 304, 28-32.
115. J. Yu, Y. Zhang, A. Kudo, *J. Solid State Chem*, 2009, 182, 223-228.
116. H. Fan, T. Jiang, H. Li, D. Wang, L. Wang, J. Zhai, D. He, P. Wang, T. Xie, *J. Phys. Chem. C*, 2012, 116, 2425-2430.
117. G. Tan, L. Zhang, H. Ren, S. Wei, J. Huang, A. Xia, *ACS Al. Mater. Interfaces*, 2013, 5, 5186-5193.
118. H. Fan, T. Jiang, H. Li, D. Wang, L. Wang, J. Zhai, D. He, D. Wang, T. Xie, *J. Phys. Chem C*, 2012, 116, 2425-2430.
119. X. Zhang, Z. H. Ai, F. L. Jia, L. Z. Zhang, X. X. Fan, Z. G. Zou, *Mater. Chem. Phys*, 2007, 103, 162-167.
120. Li, G. Pang, G. Sun, M. Feng, *J. Nanopart. Res*, 2010, 12, 3069-3075.
121. T. Saimi, K. Hideki, K. Akihiko, *Chem. Mater*, 2001, 13, 4624-4628.
122. A. Tucks, H. P. Beck, *J. Solid. State. Chem*, 2005. 178, 1145-1156.
123. W. Luo, Z. Wang, L. Wan, Z. Li, T. Yu, Z. Zou, *J. Phys. D, Appl. Phys*, 2010, 43, 405402-405408.
124. A. Galembeck, O.L. Alves, *Thin Solid Films*, 2000, 365, 90-93.
125. B. Xie, C. He, P. Cai, Y. Xiong, *Thin Solid Films*, 2010, 518, 1958-1961.
126. B. Zhou, J. Qu, X. Zhao, H. Liu, *J. Env. Sci*, 2011, 231, 151-159.
127. S. S. Dunkle, R. J. Helmich, K. S. Suslick, *J. Phys. Chem. C*, 2009, 113, 11980-11983.
128. N. M. N. Myung, S. Ham, S. Choi, Y. Chae, W. G. Kim, Y. J. Jeon, K. J. Paeng, W. Chanmanee, W. De Tacconi, K. Rajeshwar, *J. Phys. Chem. C*, 2011, 115, 7793-7800.
129. A. Seabold, K. S. Choi, *J. Am. Chem. Soc*, 2012, 134, 2186-2192.

130. C. Li, G. Pang, S. Sun, S. Feng, *J. Nanopart. Res*, 2010, 12, 3069-3075.
131. T. Tojo, Q. W. Zhang, F. Saito, *Chem. Sust. Dev*, 2007, 15, 243-247.
132. J. N. Torba, N.V. Golubko, E.A. Fortalnova, G.M. Kaleva, M.G. Saffronenko, N.U. Venskorskii, E.D. Politova, *Acta. Phys. Pol. A*, 2010, 117, 24-26.
133. K.V.R. Prasad, K.B.R.Varma, *Mater. Chem. Phys*, 1998, 38, 406-410.

2. Synthesis and characterization techniques

A photocatalytic material can be prepared by a variety of methods, which in general terms can be categorized as comminution (top down) or controlled precipitation (bottom up) [1]. The criteria of a good photocatalyst are as follows,

- a) Surface chemical composition
- b) Microstructure,
- c) Surface area, ensuring number of active sites
- d) High absorption coefficient and easy utilization in the catalytic process.

There is a need for an efficient technique that is capable of imparting all the above criteria in a photocatalyst. Moreover, a technique is proved to be significantly useful only when it can be implemented in commercial applications. As mentioned in Chapter 1, BiVO_4 is an active photocatalyst in visible light region which can be used efficiently for photoelectrochemical water splitting and solar energy conversion technologies. Our objective of getting such a visible light active photocatalyst in powdered form was realized with hydrothermal and mechanochemical processes. Thin film preparations were also accomplished by ultrasonic spray pyrolysis (USP) and rf-sputtering techniques. Prepared BiVO_4 powder and thin films were then characterized for their structural, optical, morphological and electrical properties using various characterization techniques, such as X-ray diffraction (XRD), field emission scanning electron microscopy (FE-SEM), HR-TEM, UV-visible, FT-IR, dielectric and electron paramagnetic resonance (EPR) spectroscopy. The experimental set up for carrying out photocatalytic decomposition of rhodamine 6G (Rh6) and methylene blue (MB) was designed and set up in our lab and discussed below.

2.1. Bismuth vanadate (BiVO_4) powder preparations

2.1.1. Hydrothermal technique

Hydrothermal technique is a soft-chemical process, which involves application of heat under pressure so that reaction takes place in an aqueous medium. This synthesis route is widely

acknowledged to generate materials with high purity, few defects and regulated morphology [2, 3]. Furthermore, concentrations of precursors, pH, reaction temperature and reaction time can be tuned for regulating particle size, size distribution and particle morphology of materials [4].

2.1.1a. Hydrothermal synthesis of BiVO₄ powders with surfactant

BiVO₄ powders with different morphologies and/or porous structures were prepared by adopting the hydrothermal method with Bi(NO₃)₃·5H₂O and NH₄VO₃ as inorganic source, oleic acid (OA), oleylamine (OL), polyvinyl alcohol (PVA), polyvinyl pyrrolidone (PVP), sodium dodecyl sulfate (SDS) and hexadecyltrimethyl ammonium bromide (HTAB) as surfactants. The typical preparation procedure was as follows: 3 mL of concentrated nitric acid (67 wt%) and 15 mmol of surfactants (OL/OA/PVA/PVP/SDS/HTAB) were added to a mixed solvent of 13 mL of ethanol and ethylene glycol (EG) under stirring. 5 mmol of Bi (NO₃)₃·5H₂O (Sigma Aldrich, ≥ 99.99% trace metal basis) was dissolved in the above mixed solution. Then 5 mmol of NH₄VO₃ (Sigma Aldrich, ≥ 99.0%) was also added under stirring condition. pH was adjusted to 2 and 9 using hydrochloric acid (HCl) and sodium hydroxide (NaOH) solution (2 mol/L) for OL surfactant while for neutral pH was maintained for other surfactants. The above mixture was transferred to an autoclave for hydrothermal treatment at 110 °C for 20 h. After being rinsed with deionized water, ethanol and then dried at 80 °C for about 12 h, the obtained solid was further calcined in air at 450°C for one hour, thus forming bismuth vanadate. Schematic illustration for the designed synthesis of BiVO₄ nanoparticles is presented in Fig.2.1.

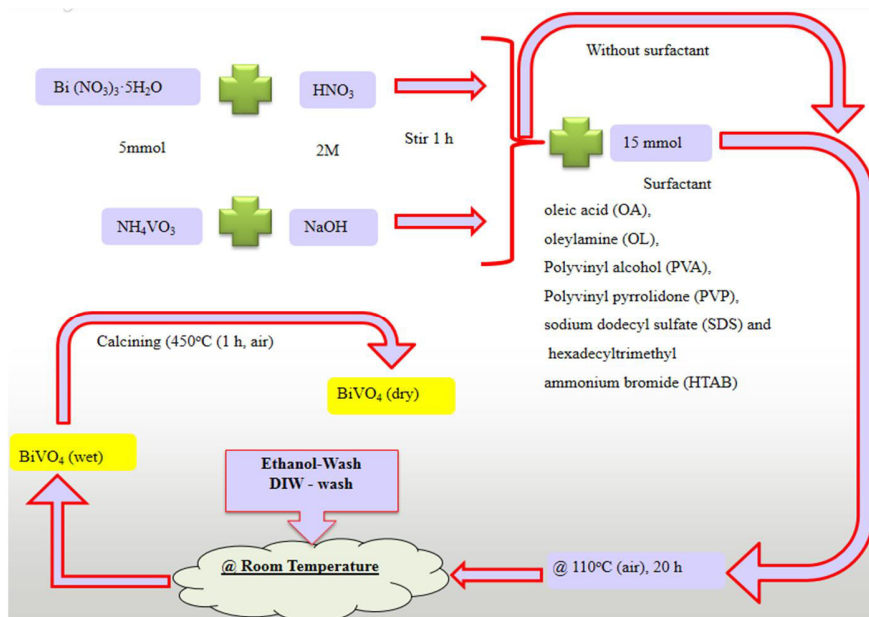


Fig.2.1. Schematic representation of the steps followed in hydrothermal process.

2.1.1b. Hydrothermal synthesis of BiVO₄ powders without surfactant

2.5 mmol of (Bi (NO₃)₃.5H₂O) (Sigma Aldrich, ≥ 99.99% trace metal basis) was dissolved in 5 mL of HNO₃ (4 M/L) and named as solution A while 2.5 mmol of NH₄VO₃ (Sigma Aldrich, ≥ 99.0%) was dissolved in 5 mL of sodium hydroxide (2 M/L) under stirring for 2 h and named as solution B. After that, A and B were mixed together in 1:1 molar ratio and stirred for about 1 h to get a stable homogeneous solution. Then, the mixture was sealed in an autoclave, and subjected to heat at 110 °C for 20 h under pressure. At the end of the process, the precipitate was filtered, washed with distilled water and ethanol each for three times, and dried at 80 °C for about 12 h. The obtained solid was calcined in air at 450 °C for one hour, thus leading to the formation of bismuth vanadate.

2.1.2. Ball milling

Mechanical alloying (MA) is a powder processing technique that allows production of homogeneous materials starting from blended elemental powdered mixtures. John Benjamin [5] and his colleagues at Paul D. Merica Research Laboratory of International Nickel Company



Fig.2.2. Planetary ball mill-Retsch PM 400 (taken from Retsch web page).

(INCO) developed the process around 1966. Benjamin [5] has summarized historic origins of the process and some background work that led to the development of present processing technique. MA is typically used for milling of two or more different metals or compounds. Material transfer is involved in this process to obtain a homogeneous alloy [6]. The device used for milling is shown in Fig.2.2. The primary goals of MA are grain size reduction; particle size control; solid-state blending; altering or changing the properties of material; and mixing or blending two or more materials [7].

2.1.2a. Mechanical alloying process

MA involves mixing of precursors in the right proportion and then loading them into the milling media for the formation of desired product. The process of milling takes place for a stipulated period of time so that a steady state is attained when the composition of powder particles are similar to the elemental proportion of the starting precursors. During the process of milling, the media gains energy due to collisions. During such collisions, sample is systematically compacted/deformed, cold welded and fractured. This deformation taking place at

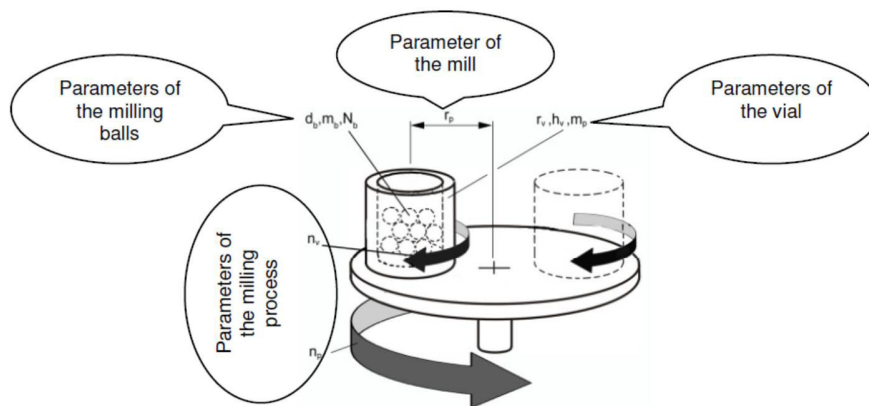


Fig.2.3. Parameters affecting the milling process in a planetary ball mill.

high strain rate results in the production of nanostructured materials [8]. As milling continues the mixed powder undergoes (i) refinement of crystallites (ii) nucleation of new phase from highly reactive powders activated by high energy ball milling, (iii) crystallization and crystal growth of newly-formed phase [9]. The working principle of the planetary ball mill is based on relative rotational movement between the grinding jar and the sun wheel. The higher the speed ratio, more is the energy generated. The most important parameters that affect the milling process is shown in Fig.2.3.

2.1.2b. Mechanochemical preparation of BiVO₄

All chemicals used were of analytical grade. BiVO₄ samples were prepared by milling pure bismuth oxide (99.999%, Sigma Aldrich) and vanadium oxide (99.99%, Sigma Aldrich) using a Retsch-planetary ball mill PM 400. Based on BiVO₄ phase diagram, Bi₂O₃ and V₂O₅ precursors [10] mixtures of about 8 g were homogenized by suitable grinding using agate mortar and pestle and then loading into 80 ml tungsten carbide jar with tungsten carbide balls of 10 mm

diameter. Schematic illustration of steps followed in the mechanochemical synthesis was presented in Fig.2.4.

In the present work, Retsch Planetary ball milling machine was used which consists of,

-Milling container-80 ml Tungsten Carbide jar with 10 mm diameter tungsten carbide balls

-Milling speed-400 Rotation per minute (RPM) for all Ball-to-powder weight ratio (BPR)

Under the conditions:

-Milling atmosphere-air

-Ball-to-powder weight ratio (BPR)-5:1, 8:1 and 10:1,

Following solid state reaction takes place during the mechanochemical process [11],



Table 2. 1. Characteristic parameters used for mechanochemical process.

BPR	5:1	8:1 (wet and dry)	10:1
Milling Time (hours)	6,11,12,13,14,15,16 and 25	6 and 11	6 and 11

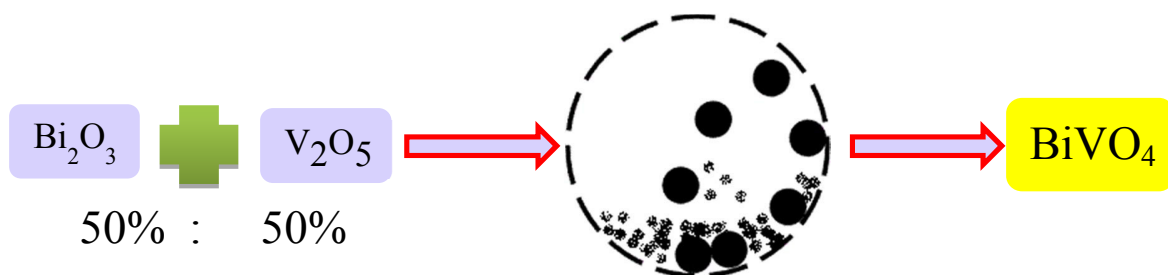


Fig.2.4. Schematic representation of ball milling steps.

2.2. BiVO_4 thin film preparations

From the application point of view, powders have its own demerits such as difficulty in monitoring and separation of photocatalysts, unavoidable mixing of O_2 and H_2 in a single reaction system, moreover significantly high energy penalty has to be paid for separation of both the gases. These problems can be avoided by using thin films. Generally thin film deposition involves series of steps: a source material is converted into vapor form (atomic/molecular/ionic species) from condensed phase (solid or liquid), which is transported to substrate and then it is allowed to condense on the substrate surface to form solid film [12]. The deposition techniques

are broadly classified into two categories, viz. Physical and Chemical methods [13]. The following sections discuss the methodology and experimental set-ups used in thin film deposition, namely ultrasonic spray pyrolysis (chemical method) and rf-sputtering (physical method).

2.2.1. Ultrasonic spray pyrolysis (USP)

Electrostatic atomization of liquids has been investigated since 1914 [14], however, only recently it has been applied in spray pyrolysis. Electrostatic spray deposition (ESD) was first used for the preparation of yttria-stabilized zirconia (YSZ) and LiMn_2O_4 thin films [15, 16]. Spray pyrolysis can be used to produce nanosized powders and thin solid films. The process is based on the pyrolytic decomposition of BiVO_4 droplets onto a heated substrate, under atmospheric conditions, by changing the concentration of precursors, carrier gas flow rate, nozzle distance, substrate temperature, deposition time and nozzle type. The main advantage of this technique is, low equipment cost and a simple atomization process. Additionally, the deposition takes place in ambient atmosphere as compared to other applications which involves inert gases or vacuum [17].

Schematic diagram and the actual experimental set up of the ultrasonic spray pyrolysis system is shown in Fig.2.5. It constitutes of the spraying unit (nebulizer), liquid feeding unit, heater, exhaust system and a temperature control unit. The system was designed to have large scale deposition by nozzle movement, varying flow rate from 50 mL to 15 L/min and producing droplets at the rate of 4 mL/min. The nature of precursors, deposition temperature and carrier gas flow rate are major parameters of the process to be investigated.

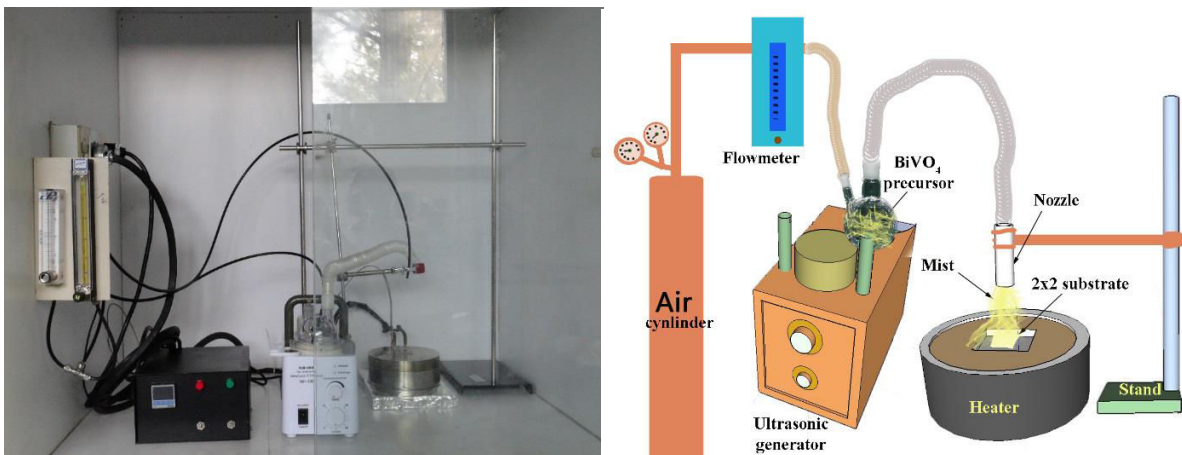


Fig.2.5. Ultrasonic spray pyrolysis setup and schematic diagram of the deposition process.

2.2.1a. Preparation of BiVO₄ thin film using ball milled powders of BiVO₄ precursor

The deposition process can be divided into three main steps: atomization of precursor solution in the nebulizer, transportation of aerosol by carrier gas and decomposition/deposition of aerosol on heated substrate. The precursor solution was prepared by dissolving 0.05 M of ball milled BiVO₄ in 3 M nitric acid (HNO₃). A static commercial ultrasonic nebulizer (Yuehua, WH-802) with 1.7 MHz resonator was employed to generate aerosols having a fairly uniform size distribution in the diameter range of 1-5 μm. The aerosols were transported to the substrates (fixed firmly on to a flat heater) using air. The substrate temperature was varied from 325 to 400 °C with a step of 20 °C and spraying duration of 15 min. The CORNING micro slides, plain glass

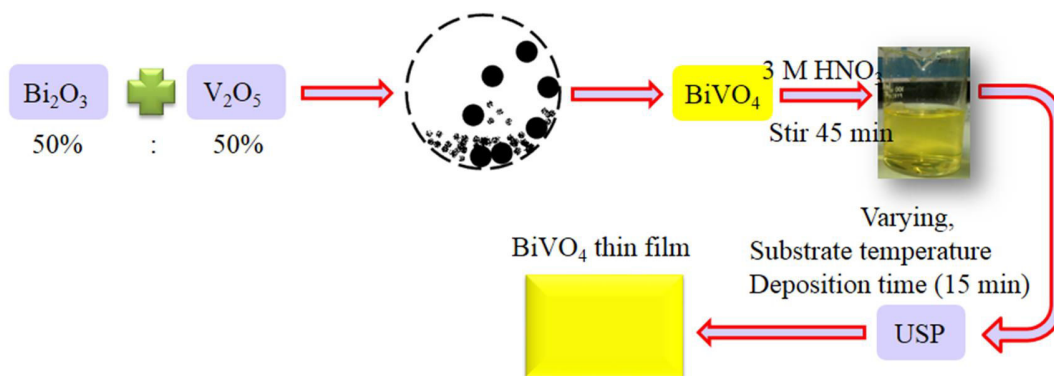


Fig.2.6. Schematic representation of the steps followed in USP using ball milled BiVO₄.

substrate was cleaned under ultrasonication in isopropanol before being loaded onto the substrate holder. The aerosols evaporate on reaching the hot zone and react with oxygen at the substrate surface to form BiVO₄ thin films. The substrate temperature was calibrated by placing a K-type thermocouple. Two step process for the preparation of BiVO₄ thin films from ball milled BiVO₄ powder was illustrated in Fig.2.6.

2.2.1b. Preparation of BiVO₄ thin film using commercial precursors

BiVO₄ thin films have been deposited on glass substrates using ultrasonic spray pyrolysis.

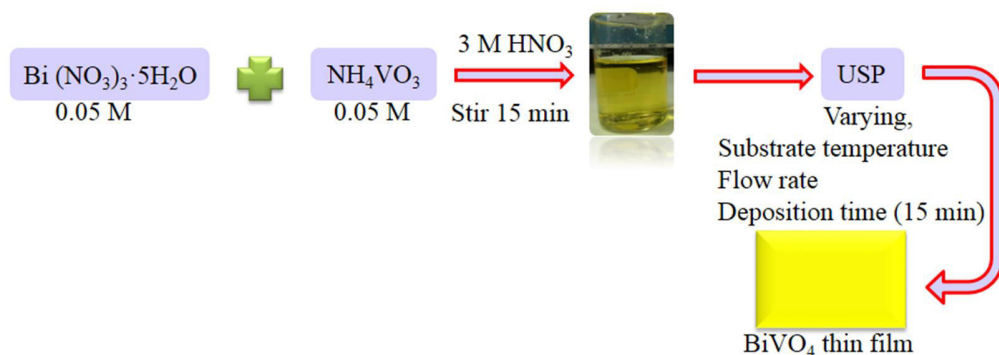


Fig.2.7. Schematic representation of the steps followed in USP using commercial precursors.

0.05 M solution of bismuth nitrate pentahydrate ($\text{Bi}(\text{NO}_3)_3 \cdot 5\text{H}_2\text{O}$) (Sigma Aldrich, $\geq 99.99\%$ trace metal basis) and 0.05 M solution of ammonium metavanadate (NH_4VO_3) (Sigma Aldrich, $\geq 99.0\%$) have been used as precursors. The spray solution was prepared by dissolving the precursors in 3 M HNO_3 . This solution was sprayed through 10 cm long and 2.5 cm wide glass nozzle by using air as carrier gas. The substrate temperature was varied from 300 to 500 °C at an interval of 25 °C. The temperature was continuously monitored using a K-type thermocouple fixed to the metallic substrate holder heater. After several trials, both substrate temperature and carrier gas flow rate of the system were optimized to obtain uniform and adherent films of BiVO_4 . The deposition time was 15 min. A simple process for producing BiVO_4 thin films from commercial precursors were illustrated in Fig.2.7.

2.2.2. Preparation of BiVO_4 thin film by RF – Sputtering

Sputtering is considered as most reliable technique, involving atom-by-atom deposition process. The technique is able to deposit metals and compounds onto RT or on hot substrates at specific rates. It also ensures sputtering of non-conductive materials at enhanced rates. RF-sputtering has gained an excellent reputation for providing uniform and homogeneous preparation of different kinds of single or mixed oxides and can be used at both laboratory and industrial scales [18]. The simple line diagram and the Plassys (MP 300) commercial rf-sputtering system used in this study are shown in Fig.2.8 a and b respectively. Substrates are placed in a vacuum chamber facing the target which is composed of material to be deposited. The sputtering gases, argon (Ar) and oxygen (O_2) are introduced into the chamber to a pressure between 10^{-3} to 10^{-2} mbar. A high negative voltage is applied to the target (cathode), while substrate holder (anode) is connected to chamber wall which is held at fixed potential. Under high voltage, gas is ionized and a plasma is created between cathode and anode. Positively charged ions are accelerated towards cathode and their collision on the target sputters the atoms

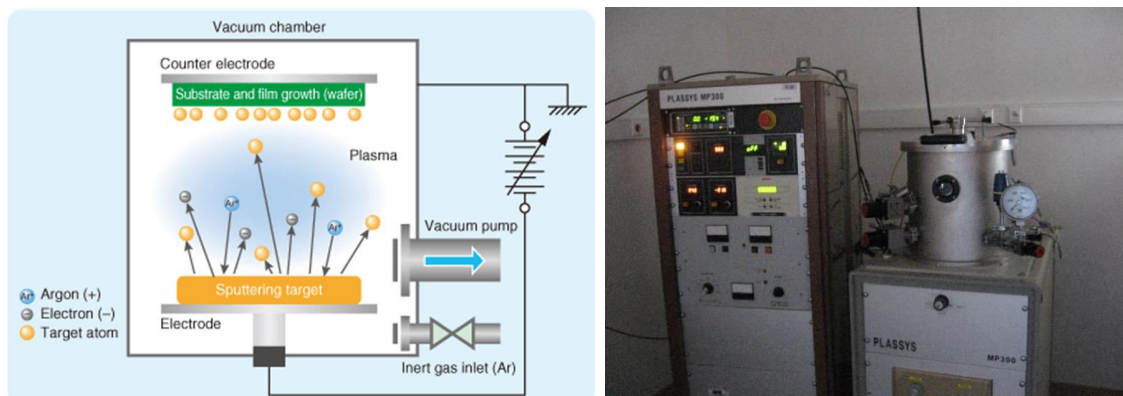


Fig.2.8. (a) The principle of rf-sputtering (taken from M-System Co. LTD); (b) rf-sputtering instrument used for BiVO_4 thin film depositions.

from the target. These atoms travel across the chamber and reach the substrate, resulting in formation of thin layer of the target material. The deposition rate is dependent on rf-pressure inside the chamber, substrate temperature, deposition time and rf-power applied to the target.

The optimized BiVO_4 power obtained from ball milling was uniaxially pressed into a disk of 3.3 cm in diameter. The disk was calcined at $900\text{ }^\circ\text{C}$ ($10\text{ }^\circ\text{C}/\text{min}$) in an atmosphere of air for 10 h, so that it becomes dense to withstand rf-power. This disk was then gradually cooled to room temperature. After cooling the pellet surface was polished and this sintered single-phase BiVO_4 disk was employed as the sputtering target. RF-sputtering experiment was successfully used to prepare single-phase monoclinic BiVO_4 thin film structure from the target.

2.2.2a. Thin film deposition

Silicon (Si) (100), borosilicate (BK7-pre-cleaned) and glass slides (2x2 cm) were used as substrates for the deposition of BiVO_4 films. Prior to deposition, substrates were cleaned in hot bath ($50\text{-}90\text{ }^\circ\text{C}$) of H_2SO_4 : methanol (1:1) for 15 min followed by rinsing with deionized water. The system was evacuated to a base pressure of 2×10^{-6} mbar. The target-to-substrate distance was fixed (7 cm). The sputter cleaning (15 min) of the substrate and target surfaces were carried out prior to film deposition by inserting the shutter between substrate and target. RF-sputtering deposition was performed at different substrate temperature (T_{sub}), rf-power and deposition chamber pressure to investigate the deposition rate, surface morphology and surface roughness of thin films. Ar and Ar/ O_2 mixture were used as sputtering gases for BiVO_4 thin films. Designed experimental steps followed in this study for the preparation of BiVO_4 thin films using rf-sputtering was shown in Fig.2.9. After optimizing the deposition conditions, deposition time was varied from 15 to 60 min. Optimized rf-sputtering parameters for BiVO_4 thin films are enlisted in

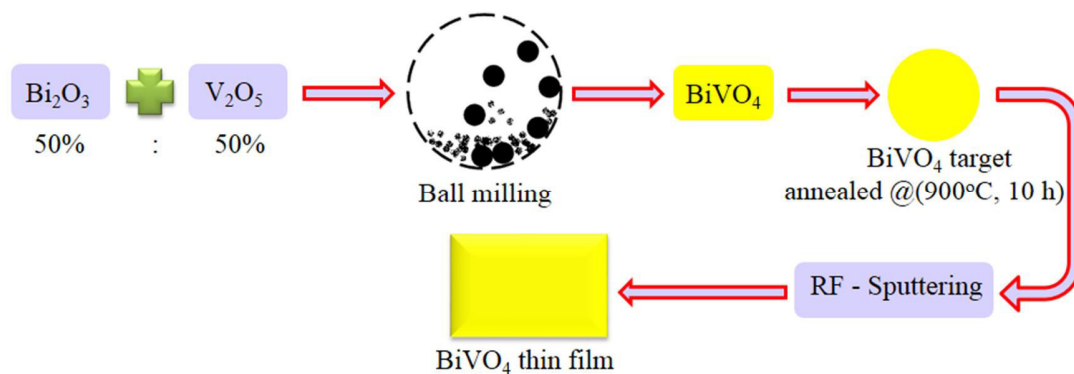


Fig.2.9. Schematic representation of the steps followed in the rf-sputtering.

Table 2.2.

Table 2.2. Variable parameters used for rf-sputtering experiments.

RF-Power (W)	Working pressure (10 ⁻² mb)	Substrate temperature (°C)	Chamber atmosphere
50	5	RT, 450 and 600	Ar
		RT, 350, 450, 550 and 600	Ar+O ₂

2.2.2b. Thin film annealing

Films deposited under Ar atmosphere were annealed in air at 400 °C for 1 h to make it crystalline in nature. It has been reported that strong re-crystallization occurs with post-deposition annealing at temperatures around 400 to 500 °C in air [19]. Post-deposition annealing of BiVO₄ films studied in this work was carried out using a furnace (Carbolite) in air, in an effort to understand the influence of O₂ in forming crystalline BiVO₄ thin films.

2.3. BiVO₄ characterization techniques

A detailed investigation of structural, morphological, optical, electrical and chemical composition of prepared BiVO₄ (micro-nano) powders and thin films are necessary for, determining whether they are suitable for visible light driven photocatalytic reactions. This section gives detailed overview of all characterization techniques used for the analysis of prepared samples.

2.3.1. Structural investigations

X-ray diffraction is a characterization technique used to determine structure and composition of compounds. It is also one of the most convenient tools to check crystal orientation, crystallite size, strain, dislocation density and inter-reticular distances. In the present study, BiVO₄ samples obtained using ball milling and USP, were analyzed using PANalytical Xpert (Fig.2.10) X-ray Diffractometer equipped with CuKα1 ($\lambda=1.5406$ Å) X - ray source, operating at room temperature in 2 θ mode.

The crystalline phases involved in rf-sputtered films were identified by X-ray diffraction (XRD) using Philips X'pert diffractometer as show in Fig.2.10, with a Cu-K α radiation. Thermo-diffractograms (HT-XRD) at room temperature for rf-sputtered thin films were recorded on Si, BK7 and microslides glass substrates using $\theta/2\theta$ Bragg-Brentano Philips X'pert MPD PRO



Fig.2.10. XRD PANalytical Xpert equipment.

diffractometer (CuK 1+2 radiations) equipped with the X'celerator detector and a HTK 1200 Anton Paar chamber. HT-XRD was performed under constant flow of air, in the scattering angle range of 5°-49°, with a 0.0167° step at different temperatures ranging from 25 to 700 °C (heating and cooling rates 10 °C/min, temperature stabilization for 20 min) in a time span of 200 minutes. Phase identification has been carried out with an X'pert high score database provided in the diffractometer and also confirmed by computer simulation with FULLPROF Rietveld refinement. *FWHM* (full width at half maximum) for all the prominent peaks were evaluated to determine the average particle size (crystallite size or coherently diffracting domains) through Scherrer equation. Parameters like 2θ range, step size, time per step were varied. XRD patterns of the powders obtained using ball milling and hydrothermal were refined from the JCPDS card no 014-0688 using FULLPROF to evaluate lattice constants and phase structure.

Crystallite sizes (*D*) are calculated using Scherrer's formula [20]:

$$D = 0.94 \lambda / \phi \quad (2.2)$$

where ϕ is full width at half maximum (FWHM) intensity of reflected peak at the Bragg angle, θ .

The strain (ϵ) is calculated using the relation:

$$\beta = \frac{\phi}{4 \cos \theta} - \epsilon \tan \theta \quad (2.3)$$

while the dislocation density (δ) is defined as the length of dislocation lines per unit volume of the crystal and can be evaluated from equation:

$$\delta = 1/D^2 \quad (2.4)$$

The inter-reticular distance *d* can be calculated from known diffraction angle θ : using Bragg's relation:

$$2d \sin \theta = n \lambda \quad (2.5)$$

where n is order of diffraction and λ is wavelength of X-ray radiation.

2.3.2. Surface analysis by field emission scanning electron microscope (FE-SEM)

Field emission scanning electron microscopy is one of the most widely used techniques for obtaining grain size, presence of minor or secondary phases, orientation of grains, uniformity, porosity, micro-structural and surface morphology of samples.

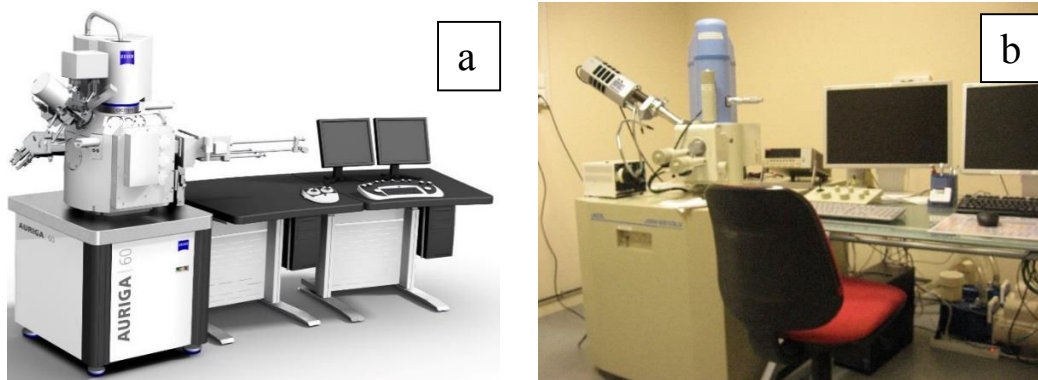


Fig.2.11. FE-SEM-Carl Zeiss Auriga 60 and SEM-JEOL, JSM 6510.

In the present work two microscopes were used to investigate the morphology of as-synthesized BiVO_4 powder and thin films namely, Carl Zeiss Auriga 60, nanotechnology system and JEOL, JSM-6510 as shown in Fig.2.11 (a) and (b) respectively. Powdered samples were dispersed ultrasonically in water and then few drops were dried directly on carbon tape for FE-SEM analysis. Thin film thicknesses were measured using Carl Zeiss Auriga 60, nanotechnology system by viewing cross section.

2.3.3. Surface studies by atomic force microscope (AFM)

Scanning probe microscope is a highly relevant tool to provide three-dimensional real space images and can allow spatially localized measurements of structure and properties.



Fig.2.12. Atomic force microscope JEOL JSPM-5200.

Surface roughness and morphology of rf-sputtered BiVO₄ thin films were examined by JEOL JSPM-5200 (Fig.2.12) Scanning Probe Microscope (AFM & STM) in tapping mode.

2.3.4. Structural studies by high resolution transmission electron microscope (HR-TEM)

High resolution transmission electron microscopy (HR-TEM) is one of the most useful tools for visualizing the nanostructure of heterogeneous catalysts at atomic level. It provides a powerful tool to analyze the internal structure of materials. The micrographs were obtained using two different HR-TEM, namely, JEOL 2010 FEG FASTEM and JEM-ARM200F as shown in Fig.2.13. JEM-ARM200F incorporates a spherical aberration corrector for electron optic system as standard. It contributes to a scanning transmission image (STEM-HAADF) with a resolution of 0.08 nm, the highest in the world among the commercial transmission electron microscopes.

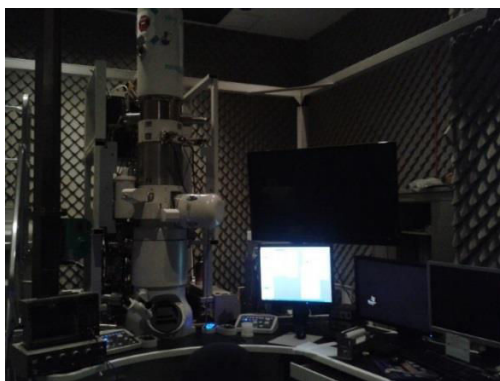


Fig.2.13. HR-TEM-JEOL ARM200F.

2.3.5. Elemental analysis by energy dispersive X- ray analysis (EDAX)

Chemical composition of powders and thin films have been evaluated by energy dispersive analysis of X-rays (EDAX) using Carl Zeiss Auriga 60, nanotechnology system coupled with a Bruker Quantex EDS featured with XFlash detectors. The scans were done with different accelerating voltages (5-10 kV), emission currents and working distances (3 mm to 15 mm).

2.3.6. Optical absorption studies by UV–Vis spectroscopy

Optical absorption is generally considered to be a key parameter in determining photocatalytic degradation rates. Diffuse reflectance spectroscopy is a useful tool for characterizing optical properties of materials. The diffuse reflectance spectra over a range of 300-800 nm were recorded by a Varian Cary 500 Scan UV-VIS-NIR system equipped with an

integrating sphere diffuse reflectance accessory for the determination of optical absorption measurements and allows to deduce band gap data. Optical absorption spectra of the films were recorded in the range of 300-800 nm on a Varian Cary 100 Scan UV-Visible spectrophotometer.



Fig.2.14. UV-Visible spectrometer Cary varian 100 scan.

In this study, the used UV-Vis spectrometer can be visualized from Fig.2.14.

The relationship between absorbance (A) and transmittance (T) is expressed as:

$$A = - \log (T (\%) / 100) \quad (2.6)$$

Absorption coefficient (α) can be estimated from optical transmittance spectra using the relation,

$$\alpha = \frac{2.303}{t} \log \left(\frac{I_0}{I} \right) \quad (2.7)$$

where T is transmittance value at a particular wavelength and t is thickness of the film. Study of absorption coefficient (α) of a semiconductor provides valuable information regarding inter band transitions and consequently about energy band structure of the material. Absorption of radiation gives rise to transition of electrons from valence band to conduction band. There are four types of transitions i) direct allowed ii) direct forbidden, (iii) indirect allowed and iv) indirect forbidden. The most important condition for direct transitions is that, there must not be any change in electronic k -value (momentum vector) during excitation processes. This happens only when conduction band minimum and valence band maximum occurs at the same value of k . In contrast, when there is change in crystal momentum, the process is known as indirect transition. The minimum of conduction band and maximum of valence band occur at different values of k for an indirect transition. In this case absorption of both photon and phonon or absorption of a photon and emission of a phonon takes place [21]. Transition probability is given by the relation,

$$(\alpha h\nu)^p = C (h\nu - E_g) \quad (2.8)$$

where C is a constant, E_g is the energy gap, ν is the frequency of incident radiation and h is Planck's constant. Exponent p is the number which characterizes the transition process

$p = 2$ for direct allowed transitions,

$p = 2/3$ for direct forbidden transitions,

$p = 1/2$ for indirect allowed transitions and

$p = 1/3$ for indirect forbidden transitions.

Electronic transitions between the valence band and conduction band can be direct or indirect. In both cases it can be allowed as permitted by the transition probability (p) or forbidden where no such probability exists. The band gap is determined by plotting $(\alpha h \nu)^p$ against photon energy $h\nu$. For suitable value of p the graph is a straight line and the value of band gap (E_g) is obtained by extrapolating linear portion of graph to intercept photon energy axis. Optical method provides a very simple way of finding band gap as compared to electrical method using thermal excitations which is less reliable because of the fact that effective mass of electron and holes also influence most of the electrical properties [22].

2.3.7. Raman spectroscopy studies

Raman spectroscopy is a non-destructive technique to study vibrational, rotational, and other low-frequency modes of both organic and inorganic samples. In the present study, Micro-

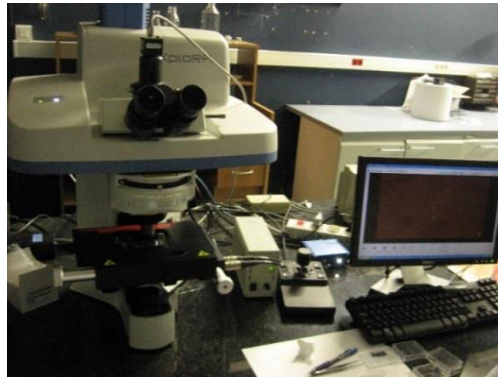


Fig.2.15. Raman spectrometer-LabRAMJobinYvon.

Raman measurements were performed using a LabRAM Jobin Yvon spectrometer as shown in Fig.2.15, with a 632.8 nm He-Ne laser source as excitation line for probing local structure of the as- prepared BiVO_4 samples.

2.3.8. Fourier transform infrared (FT - IR) spectroscopy studies

FT-IR spectrometer measurements were carried out to study bonding configurations of BiVO_4 powders. FT-IR spectra of catalysts (1 wt% sample + 99 wt% KBr) were obtained in the $400\text{-}4000\text{ cm}^{-1}$ range with a resolution of 0.4 cm^{-1} on a Nicolet 510 spectrometer as shown in



Fig.2.16. FT-IR spectroemeter Nicolet 510.

Fig.2.16.

2.3.9. Dielectric measurements

Dielectric study is one of the basic electrical characterizations technique to evaluate dielectric constant, conduction mechanism and activation energy in solids at defined frequency ranges. Dielectric relaxation spectroscopy (DRS) measurements were performed over a wide frequency range (0.1 Hz to 10 MHz) using Novocontrol Broadband Dielectric Spectrometer (Fig.2.17). To cover the experiments in a wide frequency domain, a Solartron S 11260 combined



Fig.2.17. Dielectric relaxation spectrometer

with a broadband dielectric converter (BDC) were used to obtain impedance measurements. The method is well adapted for classes of materials with a low conductivity ($\leq 1\text{ S.cm}^{-1}$) or insulating materials. Fine and homogenous powders of BiVO_4 compound were compacted into cylindrical

pellets of 5 mm diameter and 1 mm thickness by applying a uniaxial pressure of 17 MPa with a hydraulic pressure. Contact between electrodes and the sample must be good enough such that we do not need any metal deposition on the surfaces. The experimental setup consists of sample as a pellet placed between two golden plated electrodes to form a capacitor. The sample temperature was varied between 173 K and 533 K by using a stream of nitrogen gas and resistance with a controlled temperature close to sample within the accuracy of ± 0.1 K.

2.3.10. Electron paramagnetic resonance (EPR)

EPR experiments were performed on EMX - Bruker spectrometer working in X-Band (9.5 GHz). The EPR signal is related to Vanadium ions (V^{4+}) which occur in samples due to the stoichiometry departure as oxygen vacancies within $BiVO_4$ structures or from nanoparticle surfaces. The measurements were made at different temperatures by using Oxford cryostat in the range of 4 K-300 K. The resonance positions of EPR lines were accurately evaluated by using a characteristic EPR line of dry DPPH sample associated to g-factor about 2.0036. Experimental parameters such as microwave power, modulation field and detection frequency were chosen to avoid any resonant line distortion. A typical modulation field of about 1-5 Gauss and frequency modulation of about 100 kHz were used.

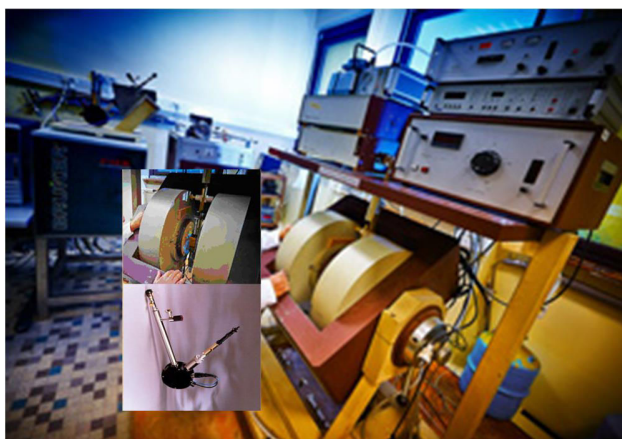


Fig.2.18. EPR spectrometer-EMX Bruker.

The recorded EPR spectra were adjusted by using Bruker commercial software Winsinfonia. These simulations give magnetic g-tensor components as well as the hyperfine parameters related to the nuclear spin of vanadium ions. EPR equipment used for this study is show in Fig.2.18.

2.3.11. Photocatalytic set – up

Homebuilt photocatalytic reactor setup was used for photodegradation studies. It consists of light source, cylindrical flask with magnetic stirrer and an online analysis system as shown in Fig.2.19. Oriel xenon lamp (50 W) was used as light source without UV-cut off filter (cylindrical glass flask acted as filter for UV radiation). The photocatalytic activities of as-prepared BiVO_4 catalysts were evaluated by the degradation of rhodamine 6G (Rh6) and methylene blue (MB) in an aqueous solution at ambient temperature.

2.3.11a. Photodegradation reaction for BiVO_4 powder

The photocatalytic activity of powdered BiVO_4 was evaluated by degradation of Rh6 and MB under visible-light irradiation of 50-200 W Oriel Xenon lamp. In this typical process, 50 mg of photocatalysts were added to 50 mL of dye (Rh6/MB) solution (5 mg/L). Before illumination, the solution was stirred in dark for 30 min to ensure establishment of an adsorption-desorption equilibrium between the photocatalysts and dyes. The solution was then exposed to visible light irradiation under stirring. At every given time interval (30 min), 3 ml of solution was collected and centrifuged to remove particles of photocatalyst. Then, the filtrates were analyzed for their absorption maximum (527 nm for Rh6 and 664 nm for MB) in UV-vis spectra using an Ulice (Reference-SPID_PCH) spectrophotometer.

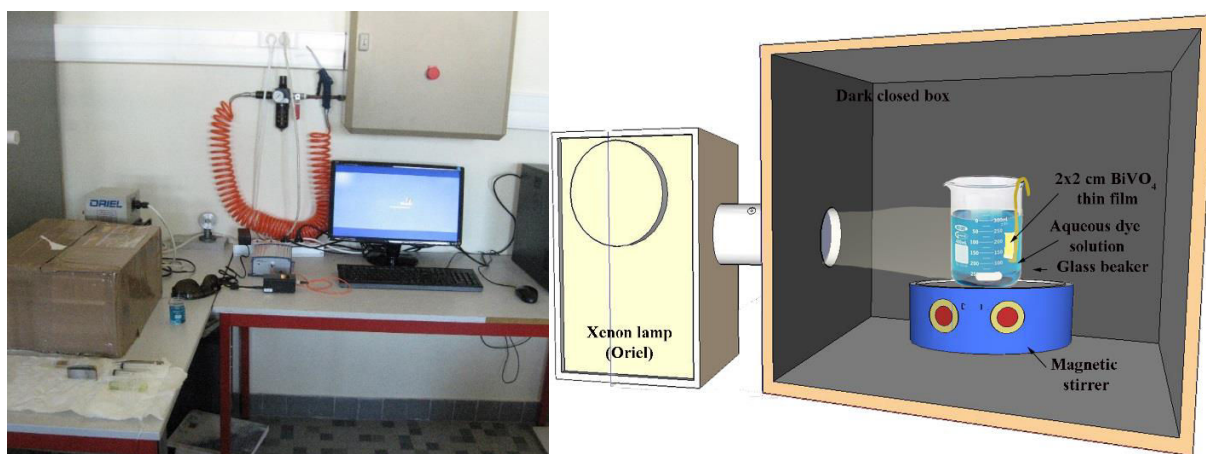


Fig.2.19. Experimental set up and schematic representation of photocatalytic reactor.

2.3.11b. Photodegradation reaction for BiVO₄ thin film

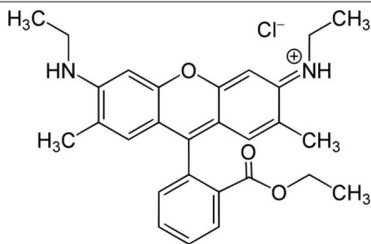
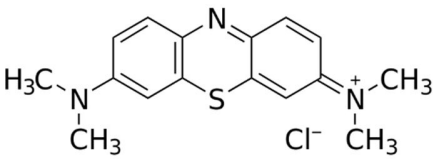
BiVO₄ thin films with a working area of 2 × 2 cm² were used for photocatalytic degradation studies. The irradiation intensities were varied in the range of 50-200 W in Oriol Xe lamp. In each experimental study, 50 ml of dye solution was used to determine the photodegradation rate. The initial concentration of each dye was maintained at 5 mg/L. During the photodegradation reaction, the solution was stirred continuously and exposed to air. The change in the dye concentration was monitored with Ulice (Reference-SPID_PCH) spectrophotometer at the maximum absorption of 527 nm for Rh6 and 664 nm for MB as shown in the table 2.3. MB is a smaller and linear molecule (structure in table 2.3) in contrast to Rh6. Therefore, it can be concluded that the higher adsorption capacities and photocatalytic activities can be expected for MB dye.

The photodegradation kinetics of Rh6 and MB can be analyzed by Langmuir-Hinshelwood equation [23], which follows the first order reaction kinetics model:

$$\ln \left(\frac{C_0}{C} - 1 \right) = -kt \quad (2.9)$$

where, C₀ is the initial absorbance, C is the absorbance after a time (t) of dye degradation, and k is the pseudo first order rate constant (min⁻¹). The rate constant k can be derived from a plot of

Table 2.3. Chemical formula, molecular weight and maximum absorption wavelength for Rh6 and MB dyes tested.

Dye	Chemical formula	Molecular weight (g/mol)	λ _{max} (nm)
Rhodamine 6g (Rh 6g)		479.02	527
Methylene blue (MB)		319.85	664

$\ln(C/C_0)$ versus irradiation time.

This chapter described the experimental techniques adopted for the preparation, simulation and characterization of BiVO₄ powders and thin films.

References

1. J. A. Schwarz, C. Contescu, A. Contescu, *Chem. Rev.*, 1995, 95, 477-510.
2. X. Guan, J. Shi, L. Guo, *International journal of hydrogen energy*, 2013, 38, 11870-11877.
3. W. L. Suchanek, R. E. Riman, *Bull Mater Sci*, 2000, 36, 453-460.
4. J. B. Liu, H. Wang, S. Wang, H. Yan, *Materials Science and Engineering B*, 2003, 104, 36-39.
5. J. S. Benjamin, *Sci. Amer.*, 1976, 234, 40-48.
6. C. Suryanarayana, *Progress in Materials Science*, 2001, 46, 1-184.
7. M. Hulle, G. G. Chernik, E. L. Fokina, N. I. Budim, *Rev. Adv. Mater. Sci*, 2008, 18, 366-374.
8. H. J. Fecht, *Nanostructured Materials*, 1995, 9, 33-42.
9. R. Venkatesan, S. Velumani, A. Kassiba, *Materials Chemistry and Physics*, 2012, 135, 842-848.
10. M. Touboul, C. Vachon, *Thermo Chimica Acta*, 1988, 133, 61-66.
11. T. Tojo, Q. W. Zhang, F. Saito, *Chemistry of sustainable development*, 2007, 15, 243-247.
12. A. Goswami, *Thin film fundamentals*, New age international P Ltd, New Delhi, 1996.
13. R. W. Berry, P. M. Hall, M. T. Harris, *Thin Film Technology*, D. Van Nostrand company Inc 1968.
14. J. Zeleny, *Physical Review*, 1914, 32, 69-91.
15. E. M. Kelder, O. C. J. Nijs, J. Schoonman, *Solid State Ionics*, 1994, 68, 5-7.
16. A. A. Van Zomeren, E. M. Kelder, J. C. M. Marijnissen, J. Schoonman, *J. Aerosol Sci*, 1994, 25, 1229-1235.
17. P. S. Patil, *Materials Chemistry and Physics*, 1999, 59, 185-198.
18. R. F. Bunshah, *Handbook of Deposition Technologies for Films and Coating*. 2nd ed. 1994, Noyes Publications.
19. M. R. da Silva, L. H. Dall'Antonia, L. V. A. Scalvi, D. I. dos Santos, L. O. Ruggiero, A. Urbano, *Solid State Electrochem*, 2012, 16, 3267-3274.
20. S. Velumani, Ph.D. Thesis, Bharathiar University, Coimbatore, India, 1998, 31.
21. L. H. Hall, J. Bardeen and F. J. Blatt, *Physical Review*, 1954, 95, 559-560.
22. J. Bardeen, F. J. Blatt and L. H. Hall, *Photoconductivity conference, Atlanta City (1954)*, John Wiley, 1956, 146-154.
23. J. Wu, Q. J. Liu, Z. Q. Zhu, *Mater. Res. Bull.*, 2011, 46, 1997-2003.

3. BiVO₄ powders: Results and discussions

Nanostructured materials offer the possibility of modulating their mechanical, electronic, optical and magnetic properties, as compared to their bulk state counterpart. Semiconducting composites with hetero-junction structures are of great interest for photocatalytic (PC) applications [1] such as, generation of hydrogen based clean energy due to water splitting, degradation of organic pollutants or waste water treatments [2]. In this context, monoclinic BiVO₄, from bismuth vanadate family, has attracted a great deal of attention in recent years due to its excellent visible light response. The recent upsurge in the hydrothermal route by different groups [3, 5] has been a constant motivation for employing hydrothermal process to synthesis BiVO₄ powders. One of the major goals of this thesis is to find the most economical synthetic route that can offer materials with improved photocatalytic performance. To fulfill this aim, a series of BiVO₄ nanoparticles were synthesized via hydrothermal method by tuning pH and using different surfactants. The effects of surfactants and pH on crystal structure, morphology and spectroscopic properties of BiVO₄ are discussed in details.

Mechanochemical process is another inexpensive technique, which is quick and versatile, for the preparation of BiVO₄ nanoparticles that has been discussed in this chapter. The study involves optimization of parameters like milling time, ball to powder ratio (BPR) and annealing temperature for the preparation of BiVO₄ nanostructures. The difference between mechanochemical and chemically synthesized BiVO₄ nanostructures was discussed based on the structural, optical, dielectric and EPR properties of as-prepared BiVO₄ samples. Theoretical simulations were performed to verify the involved structures. To evidence the monoclinic nature of BiVO₄ compound, comparison between experimental and simulated X-ray diffraction pattern was carried out and discussed in detail. The dielectric, conduction behavior and electron paramagnetic resonance (EPR) of the active electronic centers have been investigated in detail since they can significantly alter the concentration of charge carriers and their mobility. Correlation between the conductivity and the active electronic centers as probed by EPR are also discussed.

3.1. Hydrothermal process

3.1.1. Influence of pH

3.1.1.a. XRD analysis

XRD patterns of the samples synthesized at 110 °C for 20 h at 2 different pH values (2 and 9) are shown in Fig.3.1 (a) and (b) respectively. XRD pattern correspond to BiVO₄ monoclinic scheelite structure which is in good agreement with the JCPDS [6] card No. 14-0688 (space group: I2/a, a = 5.195, b = 11.701, c = 5.092, β = 90.38). The results also reveal that synthesized BiVO₄ contained no other metal oxide peaks (except BiVO₄). When pH is increased from 2 to 9, the diffraction peak intensity at 2θ = 28.9° gets reduced. Furthermore, increment in the peak intensities at 2θ = 18.6°, 18.9°, 34.5° and 35.2°, suggest that the sample obtained at pH 9 has got a preferential orientation due to acicular morphology. Multi-peak separation fitting (c and d) is carried out from 28° to 30° for (-1 3 0), (-1 2 1) and (1 2 1) diffraction peaks. The intensity/peak separation of (-1 2 1) diffraction peak increases in comparison to (-130) and (121)

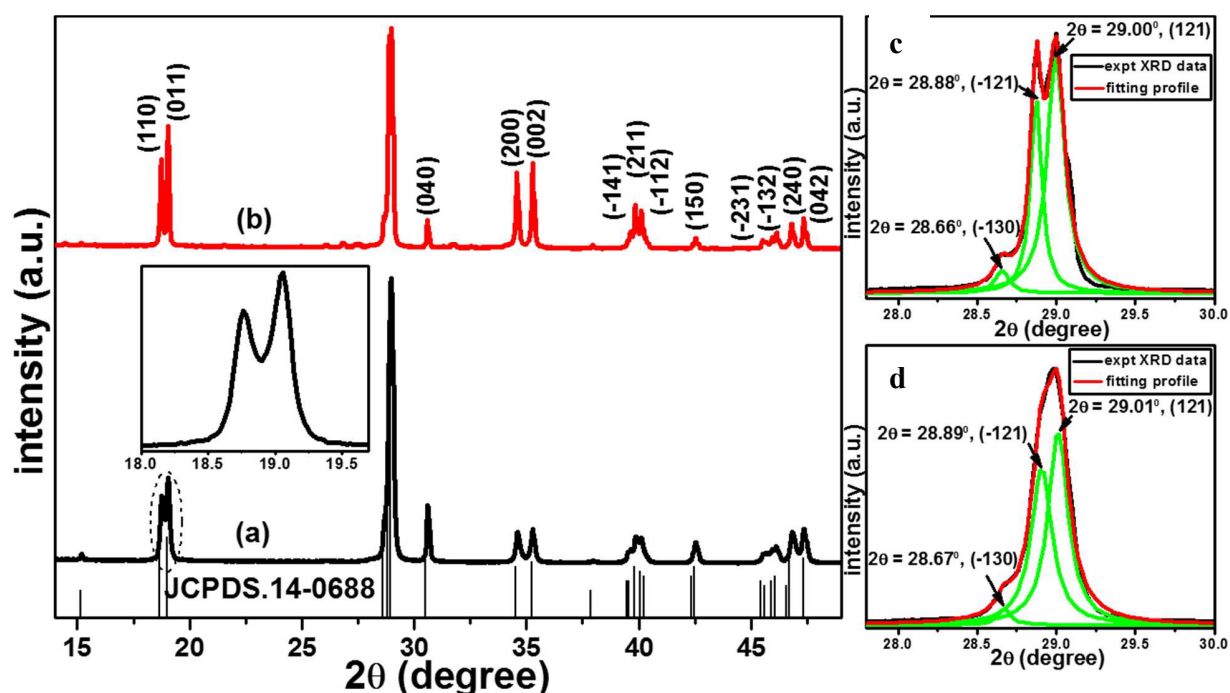


Fig.3.1. XRD patterns of BiVO₄ catalysts obtained at (a) pH=2 and (b) pH=9 and XRD multi-peak separation for the BiVO₄ crystallites from 28° to 30° according to the (-1 3 0), (-1 2 1) and (1 2 1) peaks.

peaks. This indicates that growth of BiVO₄ crystallites develop along (-1 2 1) direction as pH increases from 2 to 9.

The crystallite size of the samples a & b were calculated using equation 2.2 (chapter 2), and found to be 46 and 51 nm respectively. It can be observed that higher pH value (i.e. pH 9) induces slightly higher crystallite sizes. Likewise, it also appears that (0 1 1) and (0 0 2) planes for pH 9 exhibits a higher relative intensity with respect to the observed intensities of samples. But, the relative intensity of the diffraction line for (0 4 0) appears to be notably low. Similar trend was observed by Obregon's group [7] for monoclinic BiVO₄. By comparing the two samples obtained at different pH values, it is concluded that pH can be effectively tuned to produce different morphologies.

3.1.1b. Raman investigations

Raman scattering is an effective method for investigating crystallization local distortions in crystal lattice and vibrational properties of materials. Fig.3.2 shows Raman spectra of annealed (at 450 °C) BiVO₄ prepared by hydrothermal method at pH 2 (Fig.3.2 (a)) and pH 9 (Fig.3.2 (b)). For both the samples (pH 2 and 9), spectra exhibit typical vibrational bands at 208.5, 322.6, 365.2, 637.5, 706.3 and 824.5 cm⁻¹. The dominating Raman mode at 824.5 cm⁻¹ and a weak shoulder at 706.3 cm⁻¹ were due to the symmetric and anti-symmetric V-O stretching mode, respectively and the bands at 365.2 and 322.6 cm⁻¹ were due to symmetric and anti-symmetric bending vibration of VO₄³⁻ tetrahedra, respectively. Likewise, the peak at 208.5 cm⁻¹ can be attributed to the external modes. Hardcastle *et al* [8] reported an empirical expression [$\nu=21349 \exp (-1.97176R)$, where ν is the V-O stretching frequency and R is the V-O interatomic distance] to correlate V-O bond length with Raman stretching frequencies. Recently Yu *et al* [9] also used the same expression for correlating V-O bond length with Raman bands. It

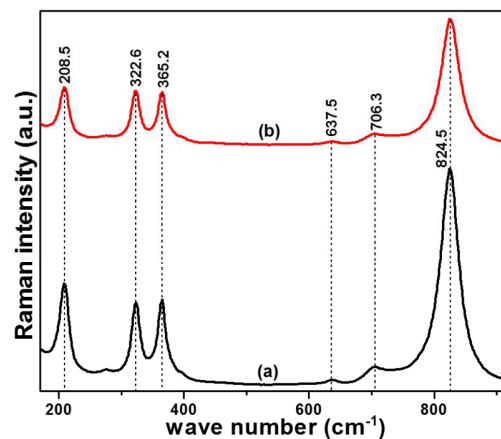


Fig.3.2. Raman spectra for BiVO₄ catalysts obtained at (a) pH=2 and (b) pH=9 after thermal treatment.

can be observed that position of the stretching mode for both pH values, is slightly shifted towards lower wavenumbers (824 cm^{-1}) as compared with literature data (827 cm^{-1}) [10, 12]. This fact would indicate a rather decreased V-O bond length for samples prepared at such lower hydrothermal temperature ($110\text{ }^{\circ}\text{C}$). The sintering effect could be the reason for shortening of V-O bond length [13]. Raman analysis showed that both the samples (a and b) are well crystallized with monoclinic structure, which is in accordance with the result of XRD.

3.1.1c. Surface morphological analysis by FE-SEM

The surface morphology and structure of BiVO_4 samples obtained at different pH values were characterized by FE-SEM and presented in Fig.3.3. It was observed that the sample obtained at pH 2 (Fig.3.3 (a)) consists of nanoparticles with meso and micropores (diameter = 20-70 nm). These meso and micro BiVO_4 nanoparticles are connected with each other to form microclusters. They constitute a porous structure with an average diameter of about 400 nm. At pH 9 (Fig.3.3 (b)), a needle-like morphological structure was observed which might be due to coalescence of the initial aciculate particles at higher sintering temperature.

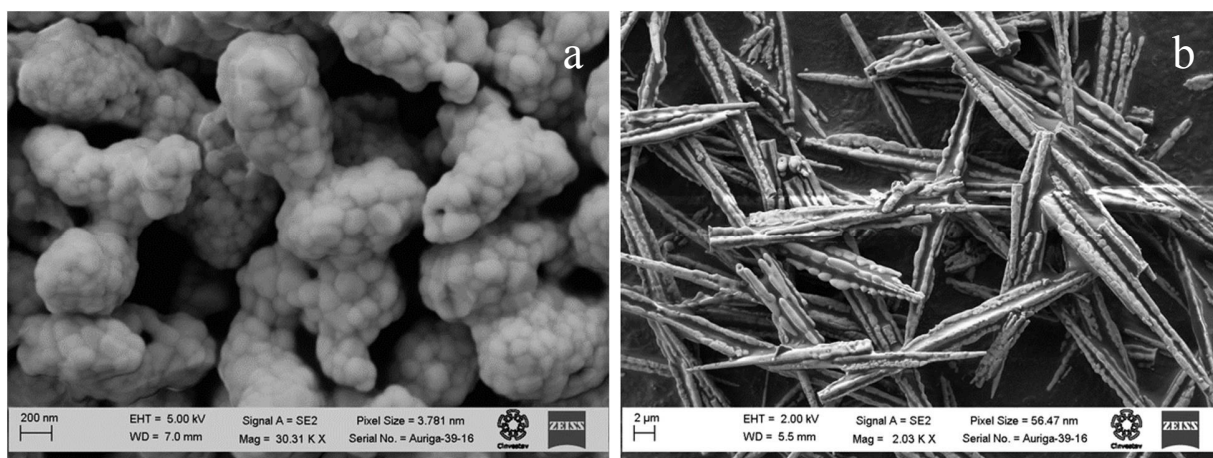


Fig.3.3. FE-SEM images of BiVO_4 catalysts obtained at (a) pH 2 and (b) pH 9.

The observed needle-like morphology explains the preferential orientation as evidenced by XRD. Thus, the crystalline growth along b axis leads to extinction of the (0 4 0) diffraction line and notably exaltation of diffraction lines corresponding to the planes (0 1 1) and (0 0 2). The difference in morphology and size of BiVO_4 might be ascribed to variation in the concentration of H^+ depending on the pH value. At low pH values for instance, the concentration of H^+ was high enough to restrain the hydrolysis of $\text{Bi}(\text{NO}_3)_3$ to BiONO_3 [14, 15]. Thus, the high

concentration of free Bi^{3+} in the reaction system resulted in the formation of BiVO_4 with large particle size due to its rapid crystal growth [16]. With increase in pH values, relatively lesser amount of free Bi^{3+} existed in the reaction system leading to smaller BiVO_4 nanoparticles due to the fast nucleation and comparatively slow crystal growth rate [17]. This result further demonstrates the dominant effect of pH and surfactant (oleylamine) on size and shape of BiVO_4 powder.

3.1.2. Influence of surfactants

3.1.2.a. XRD and Raman investigations

The detailed information regarding crystal structure and phase purity of prepared samples were obtained by XRD measurements. Fig.3.4 (A) shows XRD patterns of BiVO_4 particles synthesized with and without surfactants and calcined at $450\text{ }^\circ\text{C}$ in air. The diffraction pattern for BiVO_4 samples indicate a monoclinic structure (JCPDS File no. 14-0688) [6]. No impurity peaks were observed, which implies that the final samples of BiVO_4 were of pure phase. No significant orientation can be seen from the XRD patterns due to the random arrangement of different small crystals. The broad diffraction peaks of BiVO_4 nanoparticles indicate small crystal size. The average particle size of the as-prepared BiVO_4 nanoparticles varied between 60-100 nm as calculated using Scherrer's equation (equation 2.2, from chapter 2). These results suggest that the characteristic of a surfactant introduced during preparation affects the particle size. As a matter of fact, we could control the particle size of the material during preparation by selecting different surfactants. The formation of monoclinic scheelite BiVO_4 structure was substantiated from the results of Raman studies (Fig.3.4 (B)). It can be seen from Fig.3.4 that

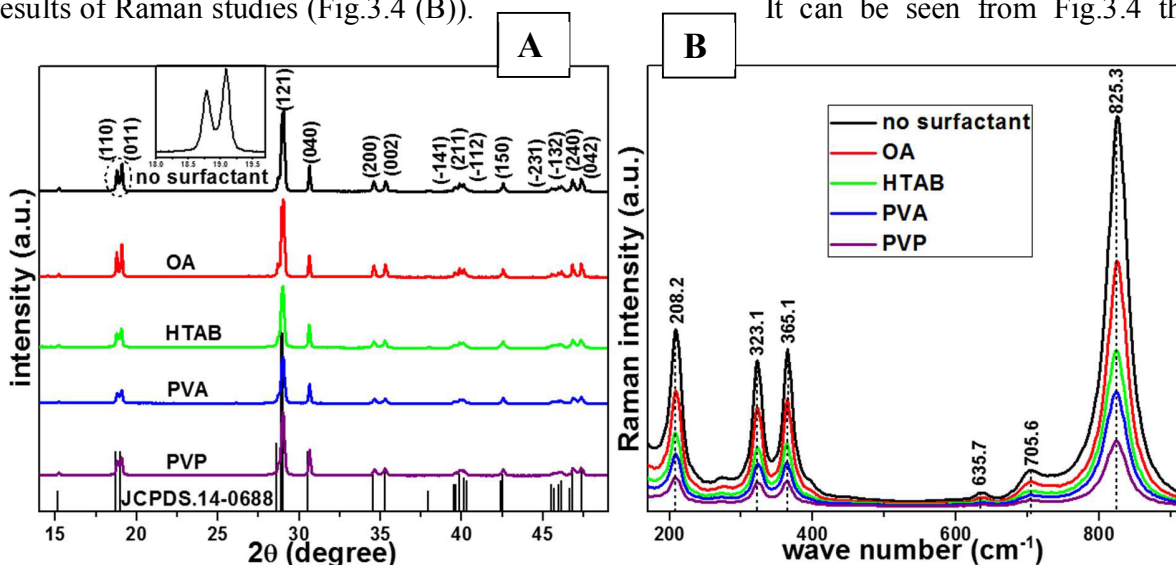


Fig.3.4. BiVO_4 samples prepared with and without surfactants using hydrothermal method. A) XRD pattern and B) Raman spectra of the obtained BiVO_4 powders.

peaks are located at 208, 323, 365, 635, 705, and 825 cm^{-1} for all the samples (with and without surfactants). They are associated with the characteristic Raman bands of monoclinic BiVO_4 . The band at 825 cm^{-1} was attributed to the symmetric V-O stretching mode and the weak bands at 705 and 635 cm^{-1} were assigned to the asymmetric V-O stretching mode. The asymmetric and symmetric bending vibrations of the VO_4^{3-} tetrahedron were detected at 323 and 365 cm^{-1} , respectively. The external mode (rotation/translation) occurred at 208 cm^{-1} . The V-O stretching mode (at 825 cm^{-1}) of BiVO_4 sample shifted to a lower frequency as compared to that (at 828 cm^{-1}) of published results [12], indicating that the bond length of our powders are shorter [12].

The differences in width and intensity of Raman bands reflected the variations in crystallinity, defect and disorder, particle size, and/or particle aggregation of these materials. The results of Raman investigations indicate that the synthesis parameters and surfactant had an important effect on the crystallinity and particle morphology of BiVO_4 samples. From Fig.3.4 (B), variations in the peak intensity among the prepared BiVO_4 samples are also observed, indicating the presence of crystallinity difference among these samples.

3.1.2b. Surface morphological analysis by FE-SEM

Surfactants are known to significantly affect the agglomeration and morphology of the particles. Morphology of the prepared samples using different surfactants were characterized by FE-SEM and presented in Fig.3.5. FE-SEM image of the powders obtained without surfactant [Fig.3.5 (a)] shows a sphere-like structure with a diameter in the range of 2-5 μm . The magnified image [inset, Fig.3.5 (a)] of these sphere-like structures show that they appear to be textured. Some cavities were observed in the center of the microspheres, which provides direct evidence that BiVO_4 microspheres have a hollow structure. The results could be elucidated by Ostwald ripening mechanism, which has been used to explain the formation of hollow nanospheres of ZnS [18] and Cu_2O [19].

The oleylamine (OA) assisted sample comprising of agglomeration of irregular shaped particles can be observed. Fig. 3.5 (c) depicts the morphology of the samples synthesized using HTAB. Instead of micro-particles, BiVO_4 crystallites assembled into microclusters in the size range of 1-3 μm . The morphology of these microclusters are cauliflower-like (hollow) and are comprised of numerous BiVO_4 nanoparticles. In PVA-assisted synthetic system, porous-like morphology was observed. The morphology of PVP sample is represented in Fig. 3.5 (e). It is

obvious that this PVP assisted sample possesses a mixture of morphologies including nanoparticles (20-40 nm) which forms hollow microclusters and flakes. Most of them exhibit mono-dispersed porous-like structures. Thus, it conforms that surfactant has a crucial role to play in determining the particle size and morphology of the final BiVO_4 products.

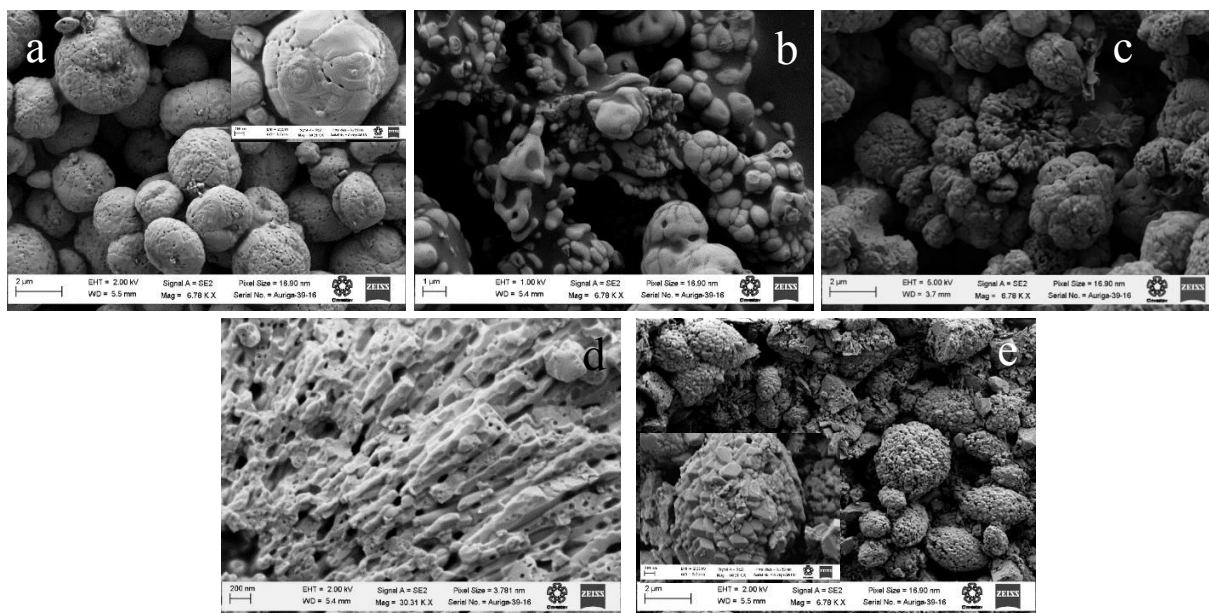


Fig.3.5. FESEM images of as prepared BiVO_4 samples synthesized at different surfactants. (a) without surfactant, (b) OA, (c) HTAB, (d) PVA and (e) PVP.

3.1.3. Optical properties (UV-Visible and FT-IR)

UV-Visible diffuse reflectance spectroscopy is a useful tool for characterizing the electronic states in optical materials. Fig.3.6 (A) shows the diffuse reflectance spectra of BiVO_4 powders prepared at (a) pH 2 and (b) pH 9. The absorption threshold of as-prepared sample is about 514.5 nm and 520.1 nm, suggesting that they can absorb visible light. Since solar light mainly covers the visible spectral region ranging from 400 to 700 nm, the prepared materials can absorb visible light in the wavelength range of 400-521 nm. It is convenient to use the band gap energy (E_g) to evaluate the optical absorption performance of a material. Acicular or needle-like BiVO_4 nanostructures formed at pH 9 possess a band gap of 2.44 eV and nanostructures formed at pH 2 possess 2.47eV. Such an optical absorption of needles show superior photocatalytic property for decomposition of contaminants under visible-light irradiation [20, 22].

Further evidence of BiVO_4 monoclinic phase can be determined by FT-IR (Fig.3.6B) analysis. The spectra demonstrate the absorptions \approx at 676 cm^{-1} corresponding to VO_4 . The band

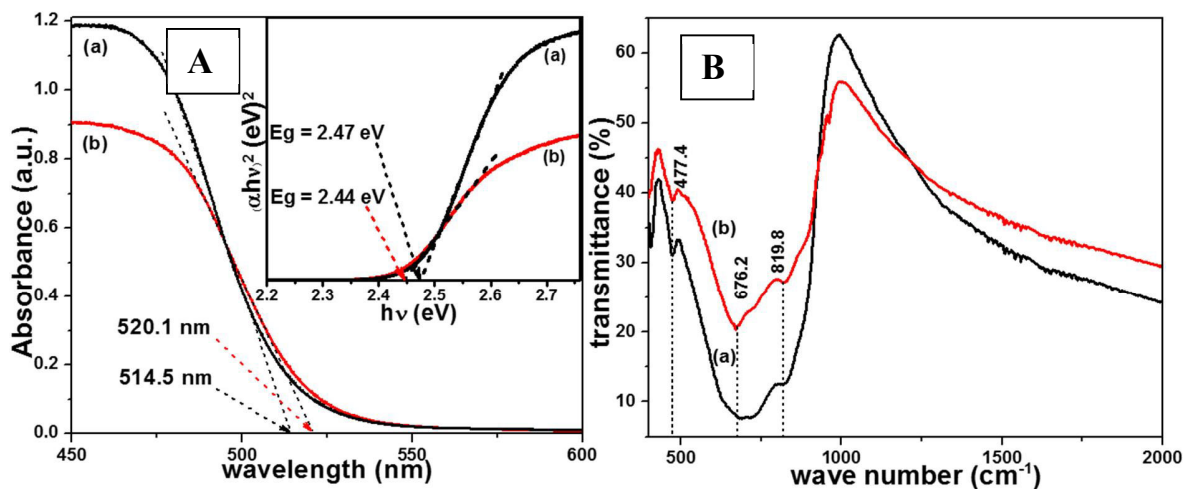


Fig.3.6. BiVO_4 samples synthesized at (a) $\text{pH} = 2$ and (b) $\text{pH} = 9$. A) UV-Visible and B) FT-IR spectra of BiVO_4 powders.

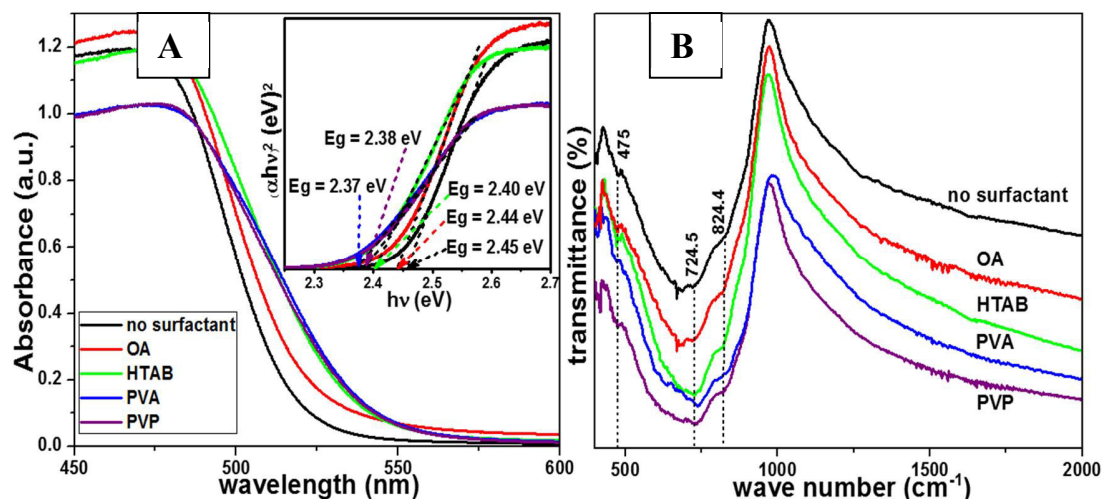


Fig.3.7. BiVO_4 samples with and without surfactants using hydrothermal method. A). UV-Visible and B) FT-IR spectra of BiVO_4 powders.

of V-O stretching is located at 819 cm^{-1} and the band at 477 cm^{-1} can be assigned to weak absorption of the Bi-O bond [23, 24]. FT-IR spectra indicates that there is no oleylamine and ethylene glycol (EG) present on the as-prepared BiVO_4 .

Fig.3.7 (A) shows UV-Vis diffuse reflectance spectra of BiVO_4 samples obtained for different surfactants. Although there were discrepancies in absorbance and absorption edge of the five samples, they exhibited strong absorptions both in UV and visible-light regions. The steep shape of the spectrum indicated that visible light absorption is due to inter band transitions. The energy band gap could be obtained from the plots of $(\alpha h\nu)^2$ versus photon energy ($h\nu$), as shown in inset of Fig. 3.7. Based on the results of analysis, sufficient visible light absorption is expected to ensure enhanced photocatalytic activities.

Fig.3.7 (B) shows FT-IR spectra of BiVO₄ samples prepared with and without surfactants. The characteristic bands of BiVO₄; the symmetric and asymmetric stretching vibrations of V-O at 724 cm⁻¹ and 824 cm⁻¹, and weak absorption at 472 cm⁻¹ corresponding to Bi-O bond, were clearly observed. The thermal treatment and washing process may efficiently remove the reaction by-products, hence yielding pure BiVO₄ with hydrothermal process.

3.2. Mechanochemical synthesis of BiVO₄ powders

In hydrothermal method, crystallized monoclinic BiVO₄ samples were obtained by changing pH and surfactants. The versatility of structures and morphologies of powders depend on different parameters. Thus reaction time, number of precursors and surfactants have to be tuned and controlled for the synthesis of such diverse nanostructures. Hence, there is an urgent requirement of an alternative method with less adjustable parameters that instigated to use ball-milling technique. Thus, BiVO₄ monoclinic scheelite structure was prepared for the first time by using mechanochemical process. In the forthcoming sections, the structural, morphological, optical and electrical properties of the ball milled BiVO₄ powders are investigated and analyzed.

3.2.1 Effect of milling time

The morphology, crystalline phase and surface states are mainly dependent on various experimental parameters. Hence as first step mechanochemical process has been used for the synthesis of BiVO₄ nanoparticles with reduced reaction time (6 h). In the initial stage of parametric optimization, the ball to powder weight ratio (BPR) was kept constant (5:1) and the milling time (6, 12,13,14,15 and 16 h) was varied. Here in this section, the results and discussions of ball milled BiVO₄ nanoparticles were characterized and the milling time was optimized.

3.2.1a. XRD analysis

XRD patterns of the ball milled BiVO₄ obtained at different milling time with same BPR (5:1) and RPM (400) are shown in Fig.3.8. Such patterns can be indexed to monoclinic BiVO₄ (JCPDS No. 14-0688). XRD patterns reveal that the main phase of all these samples is monoclinic scheelite structure with small amounts of Bi₂O₃. On the other hand, Bi₂O₃ content decreases with the increase in the milling time, while BiVO₄ content exhibits an equivalent rise.

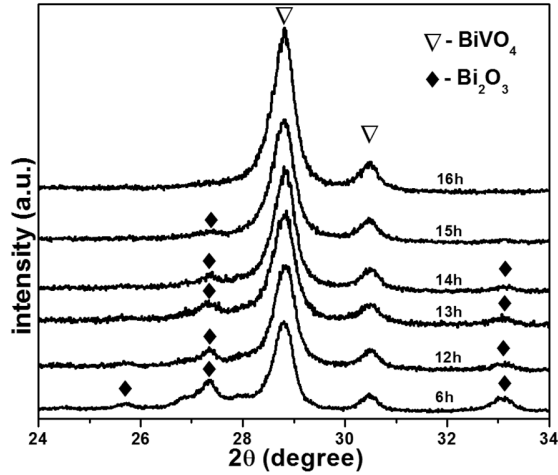


Fig.3.8. XRD patterns of BiVO_4 products derived from different milling time.

In addition, colors of the samples milled for less time are greenish yellow, suggesting that the samples may be in its inhomogeneous state. However, further increase in the milling time proves that a pure BiVO_4 monoclinic scheelite structure can be obtained after 16 h. Therefore, it seems that the phase transformations of BiVO_4 are controlled both kinetically and thermodynamically with respect to increasing milling time. It is comparable with the results obtained by Shantha *et al* [25] who carried out preparation of $2\text{Bi}_2\text{O}_3:\text{V}_2\text{O}_5$ with a centrifugal ball mill. The results had shown the progressive transformation of the starting oxides to BiVO_4 and to $\text{Bi}_2\text{VO}_{5.5}$, for 16 and 54 h of milling time, respectively. Table 3.1 gives FWHM values which increase linearly with milling time. The broadening may be due to grain refinement and/or lattice strain. Crystallite size, strain and dislocation density of the milled samples are also presented in the Table 3.1.

Table 3.1. Structural parameters of ball milled BiVO_4 .

Sample	FWHM (-121) (degree)	Crystallite size (nm)	Dislocation density $\delta \cdot 10^{14}$ Lines/m ²	Strain $\epsilon \cdot 10^{-3}$ lines ⁻² m ⁻⁴
6h	0.114	75.4	1.76	2.11
12h	0.148	58.1	2.96	2.74
13h	0.229	39.1	6.54	4.07
14h	0.266	32.3	9.56	4.92
15h	0.345	24.9	16.1	6.39
16h	0.518	16.6	36.4	9.61
16hA	0.090	95.5 ⁶⁹	1.10	1.67

In the initial stage of milling, an enhanced decrement in the grain size occurs. The reduction of grain size depends on the kinetic energy transferred from balls to powder. Initially, the kinetic energy transfer leads to the production of an array of dislocations. At certain strain level sub grains are formed. Reduction in grain size is directly proportional to milling time. Crystallinity of samples was confirmed by observing peak splitting at 18.5 (fig 3.9 inset), 35, and 46° (fig.3.9) for the optimized 16 h sample annealed at 450 °C. It confirms the increment of crystallinity and particle size with respect to annealing. Similar peak shift was observed and reported by Gao *et al* [26] for the pervovskite type photocatalyst BiFeO₃. They demonstrated that the photocatalytic ability to decompose methyl orange is significantly increased with improvement in the crystallinity of the samples. Hisatomi *et al* [27] also observed such phenomena for BaNbO₂ photocatalyst in water splitting application for improved oxygen evolution efficiency.

3.2.1b. Surface morphological analysis by FE-SEM

FE-SEM images of 16 h milled and 16 h milled -annealed samples are shown in Fig.3.10. Due to the strong agglomeration, powders were dispersed in ethanol using ultrasonicator for 20 min and then a few drops of this suspension were dried on carbon tape and gold grid for FE-SEM and TEM analysis respectively. As can be seen, the milling time has a significant influence on morphology of the product. 16 h milled sample shows irregular micro size aggregates. It can be clearly observed that the irregular micrometer sized aggregates possibly consist of nanoparticles with much smaller dimensions. It is a known fact that high-energy ball milling produces enormous amount of lattice imperfection, which leads to crystal defects, thus consequently

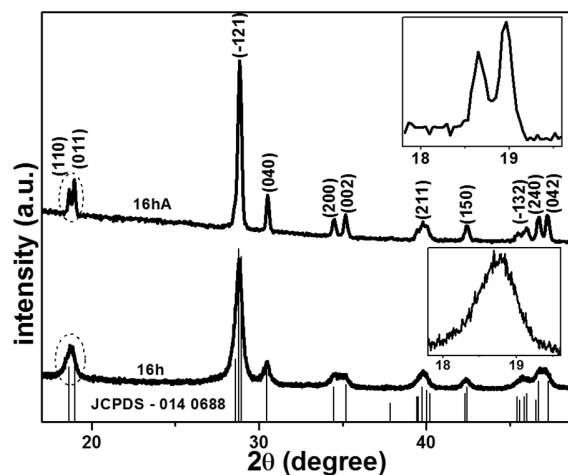


Fig.3.9. XRD patterns of 16 h milled and annealed BiVO₄ powders (inset: magnification peak at 18.8°).

decreasing the crystalline order. The agglomeration occurred due to the effects of Coulombic electrostatic and Van der Waal forces. After heat treatment at 450 °C, the apparent growth of particles can be observed and they become more compacted due to the crystallization process (Fig.3.10 (b)). No difference was observed in the dispersion of the particle sizes even after being sonicated in ethanol for more than 5 h. To clarify the size of particles in accordance with XRD results, we performed TEM analysis of 16 h milled samples. A typical large area TEM micrograph (Fig.3.10 (c) shows that BiVO₄ particles possess size of 20-30 nm and with larger aggregates. The crystalline size is in good agreement with that of XRD measurements evaluated by the Scherrer equation (section 3.21a).

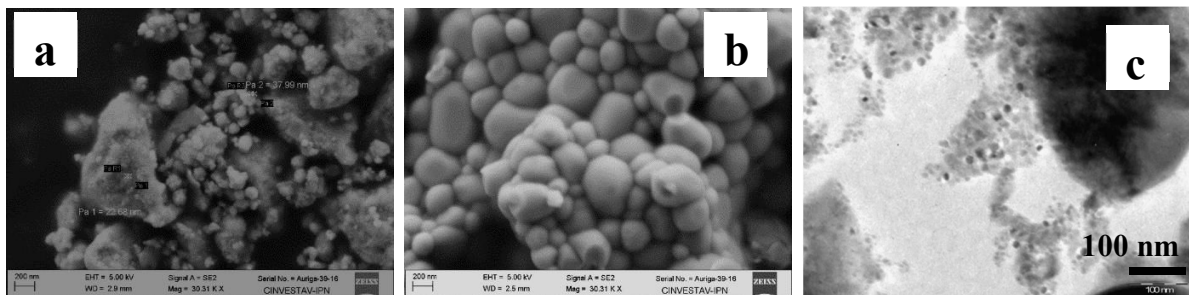


Fig.3.10. FE - SEM images of BiVO₄ (a) 16 h milled (b) 16 h milled annealed samples and (c) TEM image of 16 h milled sample.

3.2.1c. UV – Vis absorption studies

Fig.3.11 displays the diffuse reflectance absorption spectra of BiVO₄ prepared for 16 h milled and 16 h milled annealed sample (16hrA). Significant differences in the absorption edge between the milled and milled annealed samples are observed. All the samples show strong absorption in visible and as well as in UV regions. The band gap energies of milled and milled-

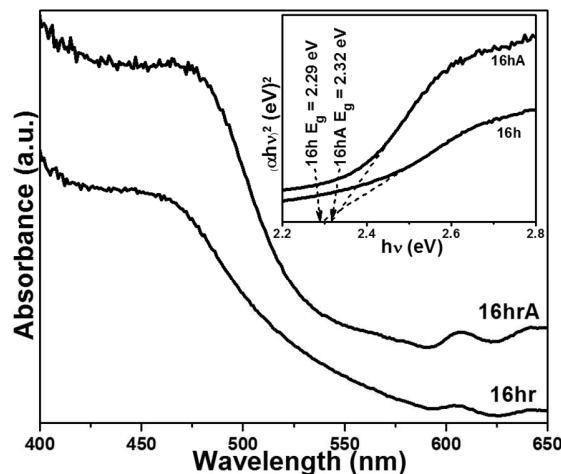


Fig.3.11. UV-Visible DRS spectra of 16 h milled and milled annealed samples. An inset figure shows $(\alpha h\nu)^2$ vs $(h\nu)$ graph.

annealed samples are 2.29 and 2.31 eV respectively. This is quite consistent with the reported band gap value of the monoclinic BiVO₄. Fig.3.11 (inset) shows the variation of optical direct band gap with the milled and milled annealed samples. The obvious blue shift of band gap absorption edges between milled and milled annealed samples were observed, which is likely attributed to size effect caused by evolution of crystal size and occurrence of crystal defects.

3.2.2. Effect of ball to powder weight ratio (BPR)

It was demonstrated that single phase BiVO₄ was obtained in 16 h with 5:1 BPR. So, to reduce the milling time, higher BPR (8:1 and 10:1) was varied and powders were milled for 6 and 11 h. The XRD results of the obtained BiVO₄ powders are summarized in Fig.3.12. It is generally recognized that during high-energy ball milling process of mixed oxide powder, three steps are involved namely, (i) refinement of crystallites (ii) nucleation of a new phase from highly reactive powders activated by high energy ball milling, and (iii) crystal growth of the newly-formed phase [28]. During initial ball milling period, the powders were mixed homogeneously and the strong mechanical collisions between the two powder particles induce their chemical melting [29].

The sample was mechano-chemically activated in air atmosphere using different ball to powder weight ratio BPR (5:1, 8:1 and 10:1) with 6 h and 11 h of milling time. Selected powders were annealed at 450 °C in air for 1 h. The samples hereafter will be designated with a label 11 h8:1 which means, powders milled for 11 h with a ball to powder ratio of 8:1 and for annealed it is represented as 11 hA8:1.

3.2.2a. XRD and simulation studies

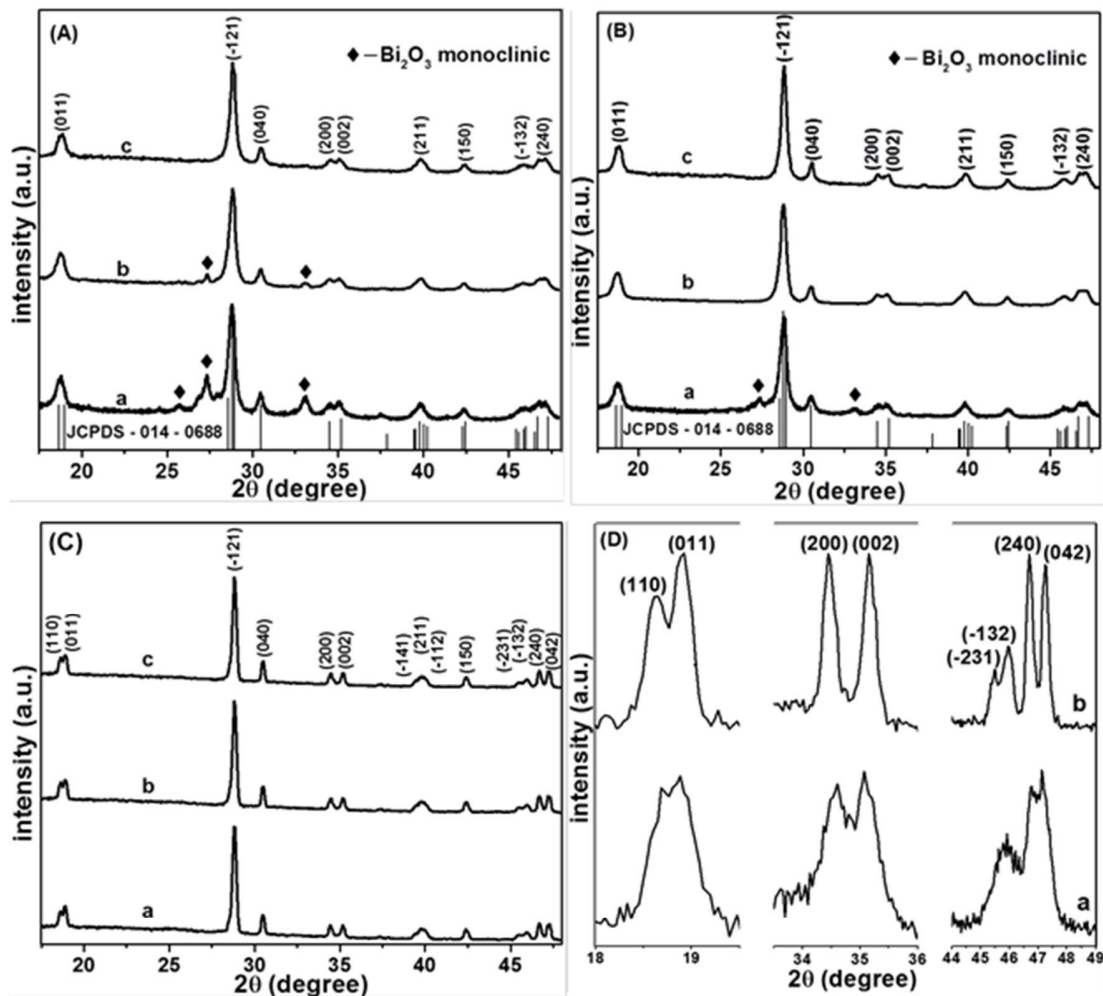


Fig.3.12. XRD patterns of BiVO_4 samples prepared under different conditions. (A) Samples prepared under different BPR with 6 h milling time: a) 6 h5:1, b) 6 h8:1 and c) 6 h10:1. (B) Samples prepared under different BPR with 11 h milling time: a) 11 h5:1, b) 11 h8:1 and c) 11 h10:1. (C) Milled-annealed samples: a) 6 hA10:1, b) 11 hA10:1, c) 11 hA8:1. (D) The magnified XRD patterns near 18.5° , 35° and 47° : a) 6 h10:1 and b) 6 hA10:1.

Fig.3.12 (A-D) shows XRD patterns of BiVO_4 powders obtained by ball milling for time durations of 6 h and 11 h with different ball to powder weight ratios (BPR). At first glance, the patterns can be readily assigned to a pure monoclinic scheelite phase with the space group $I2/a$ with lattice constants $a = 0.5195 \text{ nm}$, $b = 1.1701 \text{ nm}$ and $c = 0.5092 \text{ nm}$ which is in good agreement with the JCPDS data card number 00-014-0688 for the samples 6 h10:1, 11 h8:1, 11h10:1, 6 hA10:1, 11 hA8:1 and 11 hA10:1. For the remaining samples (6 h5:1, 6 h8:1 and 11 h5:1) it was found that there was a mixture of BiVO_4 and precursor Bi_2O_3 in their monoclinic

phases probably due to the incomplete mechanochemical reaction. However, the trace of Bi_2O_3 precursor can also reveal that the number of balls and the milling time used are not suitable enough to achieve the mechanochemical reaction to form pure BiVO_4 [1].

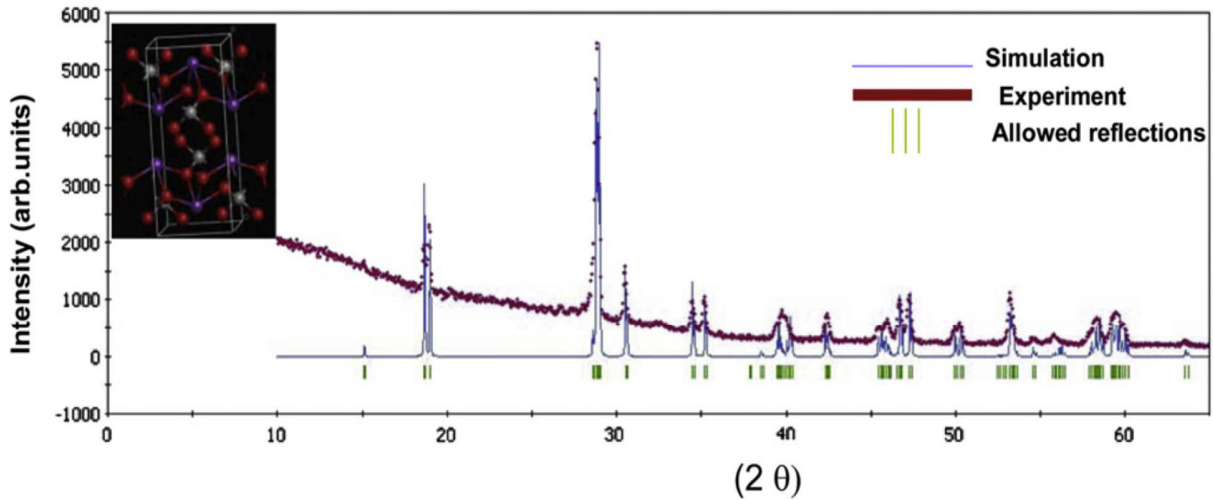


Fig.3.13. Experimental and simulated XRD patterns of monoclinic scheelite BiVO_4 . The simulation is based on DFT calculations implemented in CASTEP code. The inset shows the characteristic unit cell of BiVO_4 .

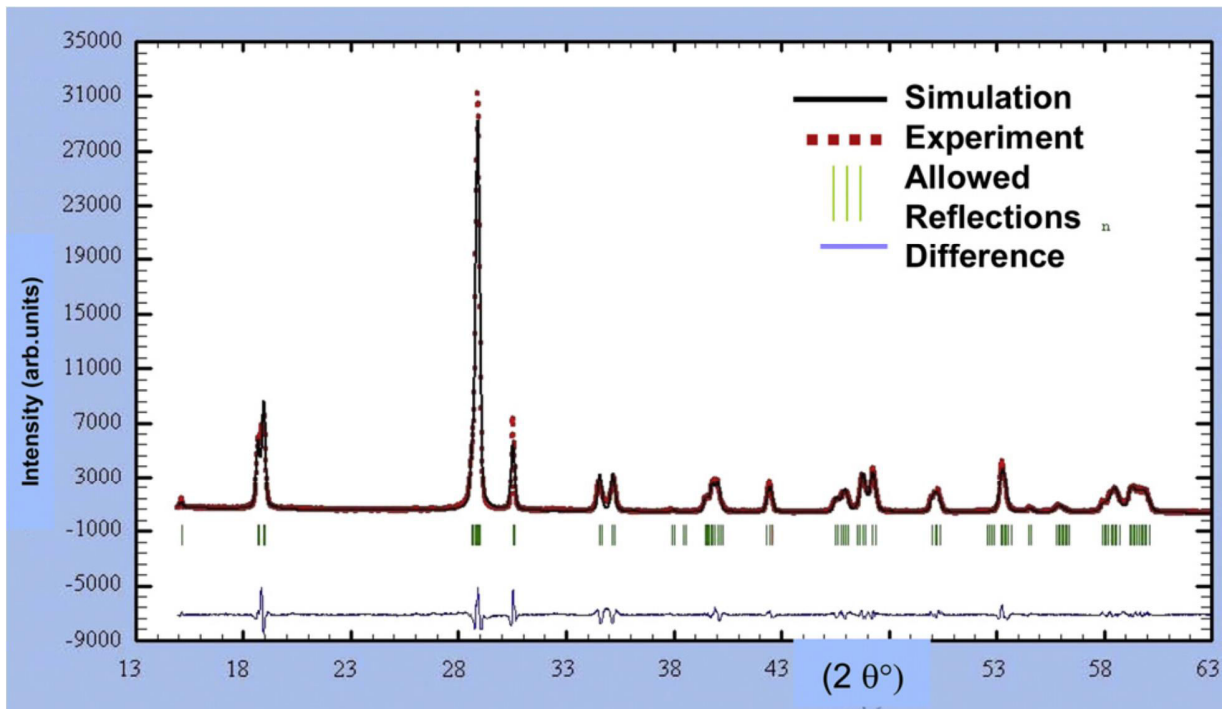


Fig.3.14. XRD pattern of monoclinic BiVO_4 sample obtained by 11 h milling and annealed at 450°C for 1h: experimental (Yobs) and refined (Ycal) by using FullProf software.

Based on simulation procedures, a quantitative analysis was carried out to identify the involved crystalline structures obtained by ball milling. Simulation studies were performed using the DFT approach as implemented in the commercial CASTEP code [30]. The ultrasoft pseudo potential was chosen in the calculations because of its advantages in both efficiency and credibility. Basic structure of BiVO_4 in the monoclinic phase is constructed by using crystallographic atomic positions and refined via DFT-LDA. Simulated structure of the monoclinic scheelite BiVO_4 is shown in Fig.3.13 with the unit cell depicted in inset of Fig.3.13 having four bismuth, four vanadium atoms and sixteen oxygen atoms. Fig.3.13 gives a comparison between XRD patterns of simulated monoclinic scheelite BiVO_4 structure and the powder prepared by 6 h 10:1 and annealed at 450 °C for 1 h. For this sample, additional reflections observed are attributed to Bi_2O_3 monoclinic phase. Increasing the milling time up to 11 h leads to pure monoclinic scheelite structure of BiVO_4 as also revealed by XRD fitting using FullProf software (Fig.3.14).

From XRD patterns and Scherrer equation, average particle sizes were estimated roughly and found to be in the range of 18-22 nm for 6 h and 11 h milling time and also for the samples processed with more balls. The BPR parameter plays an important role for the complete transformation of BiVO_4 from the precursor mixture. In addition to these effects, annealing plays a key role in increasing the nanoparticle size. Indeed, as a result of annealing at 450 °C the average particle size always increases and the particle size distribution widens. The average particle sizes were found in the order of 45 nm to few micrometers. After annealing, improvement in the crystalline order is observed as proved by well resolved peak splitting in XRD patterns at 18.8°, 35° and 46° (2θ positions). As indicated in the figure.3.12 (D) diffraction peak (0 1 1) splits into (1 1 0) and (0 1 1). Furthermore, (2 0 0) and (0 0 2) becomes well separated after such heat treatment and similar behavior was also observed for (2 4 0) and (0 4 2) diffracted peaks.

3.2.2b. Surface morphological analysis by FE-SEM

FE-SEM micrographs of the as-synthesized BiVO_4 nanopowders are shown in Fig.3.15. The agglomerations observed in all micrographs results from electrostatic forces at the interfaces and Van der Waals interactions [31]. From visual examination of fig.3.15, the as-prepared samples are composed of small and spherical shaped particles with slight agglomeration. These FE-SEM images show particle size in the range of 20 nm to few micrometers. For the annealed

samples, a net coalescence of the particles occurs leading to quite large particles with an improved crystalline order. However, the agglomerations (~micrometer) give rise to different exterior morphologies of the samples, which can be induced by different reactive surfaces.

The different morphologies observed in the samples points out a major role played by milling time and BPR parameter. Annealing alters significantly the grain size and also the morphology of samples. Kinetic energy of the medium and possibility of occurrence of exothermic process contribute to local heating of powder during milling. Beyond morphological changes, these processes improve the crystalline structures as also demonstrated by XRD investigations. It is worth mentioning that the mechanochemically assisted synthesis contributes to small sized BiVO_4 nanoparticles as compared to former reports [32, 33].

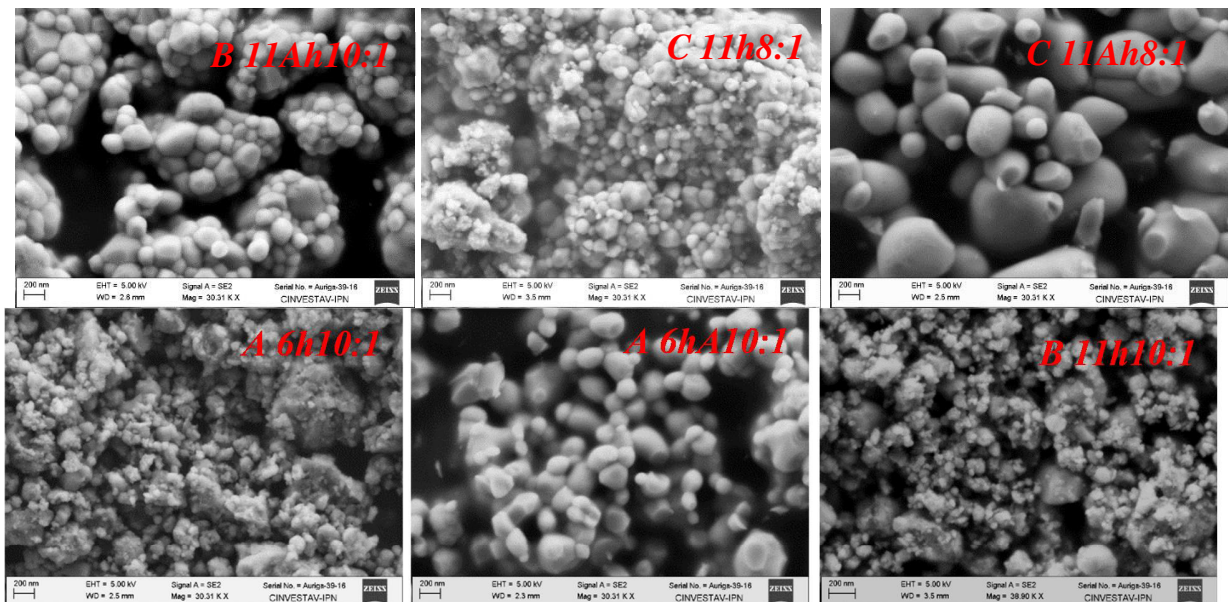


Fig.3.15. FE - SEM images of mechanochemically synthesized BiVO_4 nanoparticles. A) As prepared and annealed samples of 6 h milled with 10:1 BPR. B) As prepared and annealed samples of 11 h milled with 10:1 BPR. C) As prepared and annealed samples of 11 h milled with 8:1 BPR.

3.2.2c. Raman investigations

Raman spectrometry is a powerful tool to analyze the properties of materials using the vibrational peaks in close relation with the lattice structures. As illustrated in Fig.3.16, main Raman bands located at 211, 327, 369, 710 and 828 cm^{-1} are consistent with typical vibrational bands of BiVO_4 structures [34, 35]. It included a single major band at around 828 cm^{-1} that is

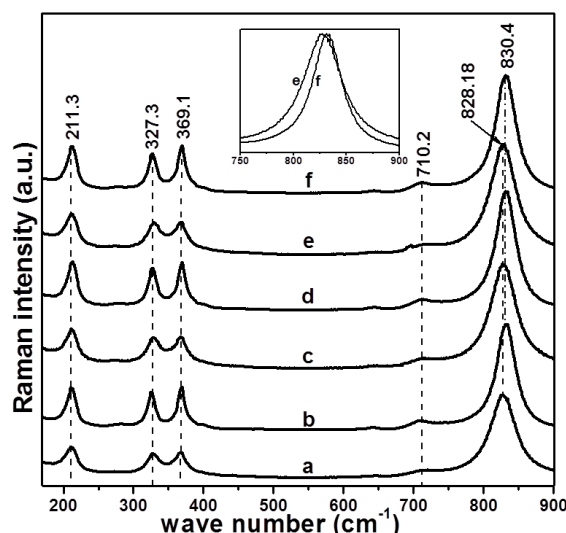


Fig.3.16. Raman spectra of ball milled samples in the defined conditions: a) 6 h10:1, b) 6 hA10:1, c) 11 h10:1, d) 11 hA10:1, e) 11 h8:1 and f) 11 hA8:1. Inset: frequency shift and FWHM decrease with annealing.

attributed to the symmetric V-O stretching mode and a weak shoulder at about 710 cm^{-1} which is due to the anti-symmetric V-O stretching. In the low wavenumber regions, the bands at 327 and 369 cm^{-1} are related to bending modes of the VO_4 tetrahedrons. Band at 210 cm^{-1} is assigned to external mode. Bands at 327 and 369 cm^{-1} are quite sensitive to the synthesis conditions with respect to different line widths, line splitting and line positions. Likewise, the stretching vibrational mode at 832 cm^{-1} is also responsible for changes in structural variations of the samples. Particularly, milling and annealing shift the 832 cm^{-1} band to high frequencies in comparison with the band of only milled samples. Moreover, along with improved crystallinity due to thermal treatment, the full width half maximum of the intense Raman band decreases (inset in Fig.3.16), thus indicating decreased vibrational frequency of V-O bond. Such observation is consistent with stretching vibrational Raman bands being associated to shorter bond lengths. This is well illustrated from the functional relationship between the Raman stretching frequencies and the metal - oxygen bond lengths in the crystalline structures [36, 38]. To sum up, Raman spectra correlate with the annealing effect and induced improvement of particle surface states and crystalline structures of all the samples. This thermal treatment affects the crystalline order of the samples as compared to time duration or mechanical milling conditions (BPR). Additionally, Raman spectra are consistent with the stabilized crystalline

structure as a pure monoclinic phase in agreement with the structural data obtained from XRD investigations.

3.2.2d. UV – Visible diffuse reflectance spectroscopy (DRS)

The diffuse reflectance spectra is used to compare the optical behavior of as prepared and annealed BiVO₄ powders as shown in Fig.3.17. All the curves show similar tendency of changes after annealing. An extrapolation of the curves to wavelength axis allows approximate estimation of band gaps, which is summarized and given in Table 3.2. The electronic structure of BiVO₄ can be outlined briefly in order to account for the optical behavior. With this aim in mind, it is worth noting that the valence band is formed by the hybrid orbitals of Bi6s and O2p while the conduction band results from unoccupied V3d states. Even if the electronic band extrema are located outside the Brillouin zone center, BiVO₄ exhibit direct band gap property, i.e. it maintains favorable low energy direct transitions [39]. The obtained values of the band gap are consistent with monoclinic BiVO₄. Comparing with the milled and milled-annealed samples, absorption edge was blue-shifted probably due to the aggregation of particles. The milled samples contain smaller particles in comparison with milled annealed ones. As a consequence, the blue shift of the band gap from 2.3 to 2.4 eV can be explained by confinement effects when the nanocrystals are smaller than the Bohr radius of excitons in crystal structures. However, it is well known fact that, annealing modifies the particles surface states and suppress all active electronic centers which can result from dangling bonds or disorder at the outermost particle surfaces. The suppression of surface electronic centers by annealing and the increased particle sizes contribute to changes on the absorption spectra of the samples.

3.2.2e. FT - IR spectroscopic analysis Fig.3.18 shows the FT-IR spectra of representative ball milled BiVO₄ samples. Whatever the sample (as-prepared or annealed), an intense and broad band at 731 cm⁻¹ with shoulders at 827 cm⁻¹ can be observed. A weak and intense IR band at 470 cm⁻¹ is also visible. According to the published results [40, 42], those IR bands correspond to the characteristic vibrations of monoclinic BiVO₄. The band at 731 cm⁻¹ corresponds to absorptions of $\nu_1(\text{VO}_4)$ and that at 470 cm⁻¹ is due to weak absorption of Bi-O bond. The IR spectra present sharp and better resolved spectra with annealing, which indicates an improvement of the crystalline order as also testified by Raman and XRD measurements. An increase in milling time and the post-synthesis annealing improves the crystallinity and stabilize the monoclinic phase of BiVO₄.

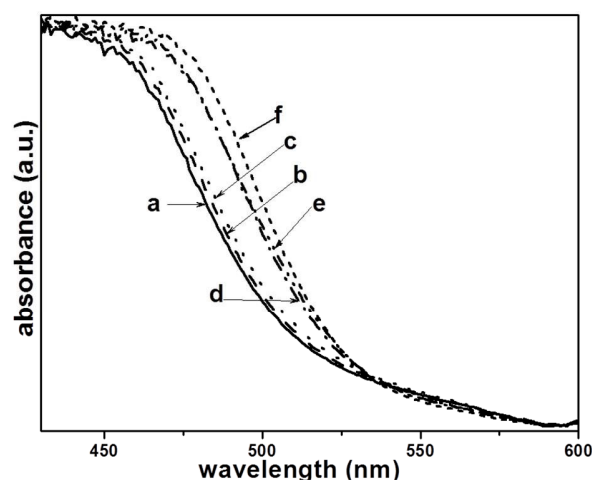


Fig. 3.17. UV - Visible diffuse reflectance spectra of the as prepared samples: a) 6 h10:1, b) 6 hA10:1, c) 11 h10:1, d) 11 hA10:1, e) 11 h8:1 and f) 11 hA8:1.

Table 3.2 Band gap absorption edges determined from diffuse reflectance experiments performed on the BiVO_4 powders synthesized by ball milling with and without annealing.

Samples reference	Absorption edge (nm)	Band gap (eV)
6h10:1	518	2.39
6hA10:1	530	2.34
11h10:1	520	2.38
11hA10:1	532	2.33
11h8:1	515	2.40
11hA8:1	530	2.34

3.2.3. Dielectric behavior, conduction and EPR active centers in BiVO_4 nanoparticles

The main drawback of nanostructured systems lies in the active electronic centers and reconstruction of the outermost nanoparticle surfaces [43]. The dielectric behavior can be used to monitor the role of interfaces in nanostructures. The main effect is related to interfacial polarizations with enhanced strength due to large specific surfaces. For BiVO_4 , mixed valence states of vanadium ions are expected to occur due to high specific surface area. EPR signal in nanostructured BiVO_4 is associated to the valance states of reduced V^{4+} which may result from

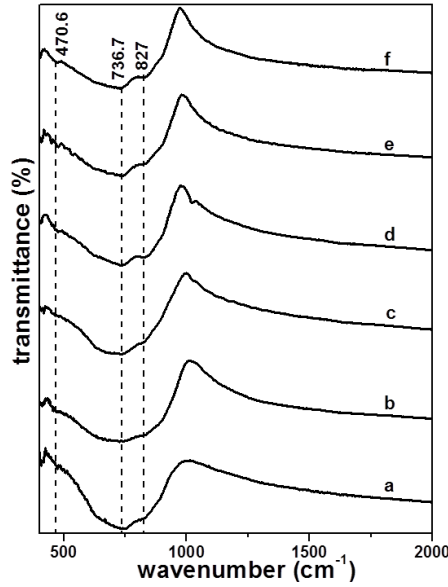


Fig.3.18. FT-IR spectra of BiVO₄ obtained under different time durations of milling and after annealing: a) 6 h10:1, b) 6 hA10:1, c) 11 h10:1, d) 11 hA10:1, e) 11 h8:1.and f) 11 hA8:1.

the stoichiometry, such as oxygen deficiencies or the surface states. EPR investigations clarify the surface or bulk location of V⁴⁺ in the structures and their local environments. These effects alter drastically the electronic and optical behavior of materials as well as their reactivity for catalytic applications. Even though the synthesis conditions were varied in a wide extent right from 11 h to 24 h and BPR from 5:1 to 10:1, we report here the dielectric and EPR results for two representative samples; i.e. A (11 hr 10:1) and B (24 hr 5:1).

3.2.3a. Dielectric investigations – Theoretical background

The analytical expression applied to the frequency dependence of complex dielectric function $\epsilon^*(\omega)$ is given by the Havriliak-Negami (HN) model [44]:

$$\epsilon^*(\omega) = \epsilon'(\omega) - i\epsilon''(\omega) = \frac{\sigma_{dc}}{i\epsilon_0\omega} + \epsilon_\infty + \frac{\Delta\epsilon}{(1 + (i\omega\tau)^\alpha)^\beta} \dots\dots\dots(3.1)$$

In this expression, dielectric strength $\Delta\epsilon$ represents the difference between the quasi-static dielectric permittivity ϵ_s and the high frequency referred to as ϵ_∞ . The coefficient τ corresponds to a characteristic time related to the dielectric relaxation phenomena which is also closely related to the conductivity process as discussed below. The phenomenological parameters α and β , in the range $0 < \alpha, \beta < 1$, are related to the distribution of relaxation times due to some

inhomogeneous processes which may be induced by nanocrystallite sizes or surface effects on BiVO₄ nanoparticles. In the case of Arrhenius process, the dielectric relaxation is characterized by a unique relaxation time τ_0 leading to $\alpha = 1$ and $\beta = 1$. For a general case, we may only give asymptotic behavior of ϵ'' (\ll) in the low and high frequency range with respect to the characteristic relaxation times. The tendencies are expressed in term of α and β such as $\epsilon'' \propto \omega^\alpha$ when $\omega\tau \ll 1$ and $\epsilon'' \propto \omega^{-\alpha\beta}$ for $\omega\tau \gg 1$. From the plot of dielectric functions, the parameter τ is closely related to the value of frequency, where the maximum dielectric loss peak is located. The coefficients α and β can be estimated only by tuning the experimental curves according to equation (1). For the frequency dependence (ac) and steady state (dc) conductivities, they are determined from the relation between the complex conductivity and dielectric function; i.e. $\sigma^*(\omega) = i\omega \cdot \epsilon_0 \epsilon^*(\omega)$.

3.2.3b. Frequency and temperature dependence of dielectric functions :

Fig.3.19 summarizes the experimental results for real (Fig.3.19 (a, c)) and imaginary (Fig.3.19 (b, d)) parts of the dielectric functions related to samples A and B. The frequency dependence of dielectric function ϵ' (\ll) reflects dynamic responses with thermally dependent relaxation phenomena. The low frequency (LF) divergence of ϵ' (\ll) traduces electrode polarization induced by ionic conductivity being thermally activated with rise in temperature.

Excluding this LF divergent contribution, the variation of dielectric data is well accounted by Havriliak-Negami model depicted as continuous lines in Fig.3.19. The same set of fitting parameters was used for both real and imaginary parts of dielectric function as well as for the frequency dependent conductivity. The calculated asymptotic behavior of ε' in the quasi-static regime is assigned to the dielectric constant which is indicative of large interfacial polarizations. Indeed, the low frequency values of ε' are about 140 and 170 respectively for samples A and B which represent twice the value (68) reported for the bulk BiVO_4 [45]. This is consistent with the large specific surfaces of nanoparticles where interfacial polarizations enhance the asymptotic dielectric constants in the quasi-static regime [46]. In order to support the relevance of interfacial polarizations as mentioned above, the Nyquist plot for sample B at

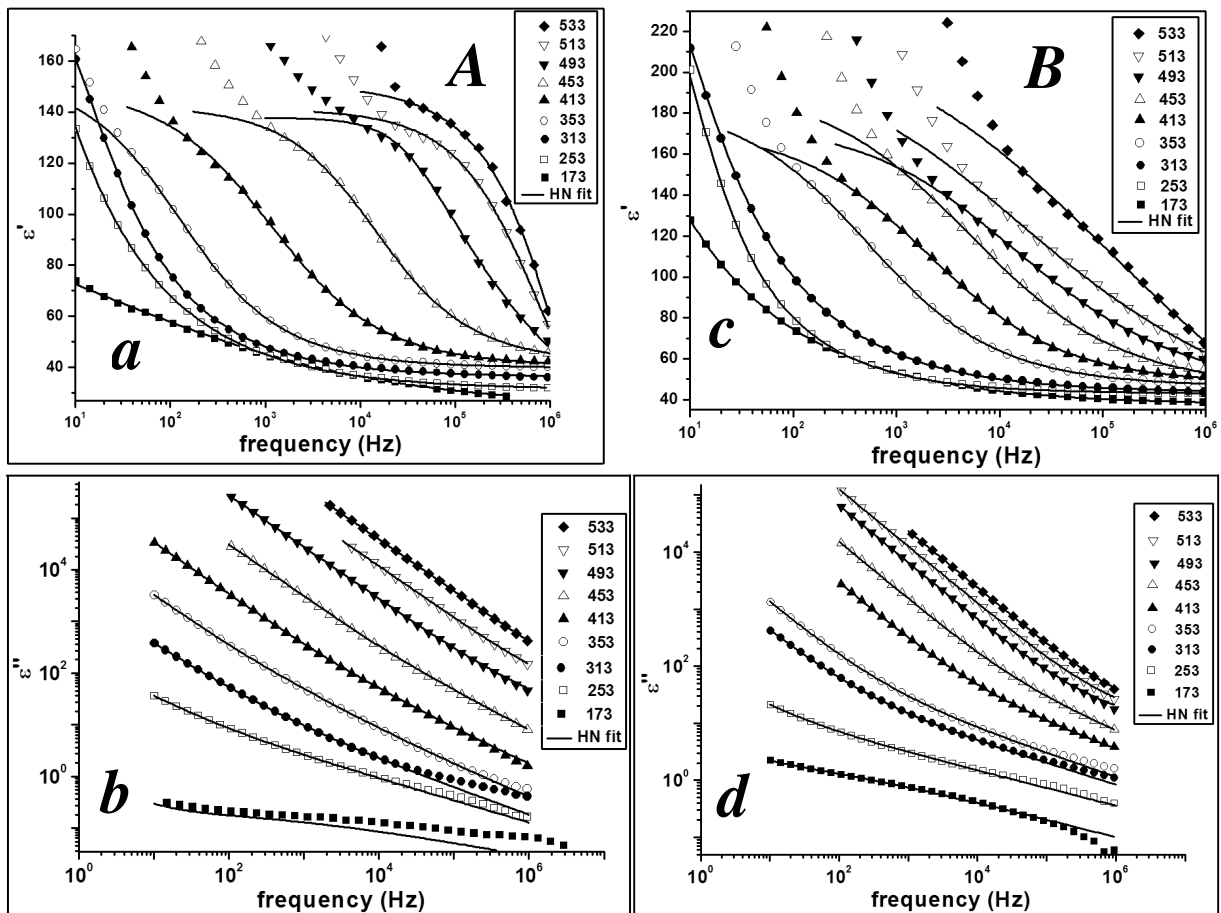


Fig.3.19. Temperature and frequency dependencies of real and imaginary dielectric permittivity in BiVO_4 nanopowders of sample A ((a) and (b)) and sample B ((c) and (d)), continuous lines are fits obtained by Havriliak-Negami model.

temperature of about 273 K is shown in Fig.3.20. Three main regions can be distinguished in the plot. The high frequency (HF) side is related to intrinsic behaviour involved in the nanoparticle core. The intermediate frequency region (IF) corresponds to the intra-particles contribution related to interfacial polarizations. The third part shown in the low frequency (LF) regime is plausibly induced by the electrode polarizations leading to the (LF) dispersion. An equivalent circuit made by two (R, C) components was used to account for the dielectric behaviour of samples where intra-grains (R_g, C_g) and inter-grains or grain boundary (R_{gb}, C_{gb}) contributions are involved (Fig.3.20) [47, 48]. A qualitative tuning of the experimental results was achieved by using the parameters in the order of $R_g = 87k\Omega, R_{gb} = 395k\Omega, C_g = 4\mu F, C_{gb} = 50\mu F$. What can be determined briefly from these results is the relevance of the contributions coming from the nanoparticle cores and their interfaces. High resistance (R_{gb}) and capacitance (C_{gb}) are plausibly connected with high barriers in the conduction channels and interfacial polarizations. Finally, the imaginary dielectric functions ϵ'' versus ω , were carefully tuned by using HN model and the results summarized in Fig.3.19 (b, d). Following the frequency range, different variation regimes of $\epsilon''(\omega)$ are involved. Thus, the linear variation accounted by the first term of Equation (3.1) indicates that steady state dc conductivity exists and increases with the temperature. Also, the behavior of $\epsilon''(\omega)$ in low frequency side is dominated by dc conductivity contribution while the higher frequencies asymptotic behavior is given by $\epsilon''(\omega) \propto \omega^{-\alpha\beta}$ which is determined to be in the order of $\alpha\beta = 0.8-0.9$.

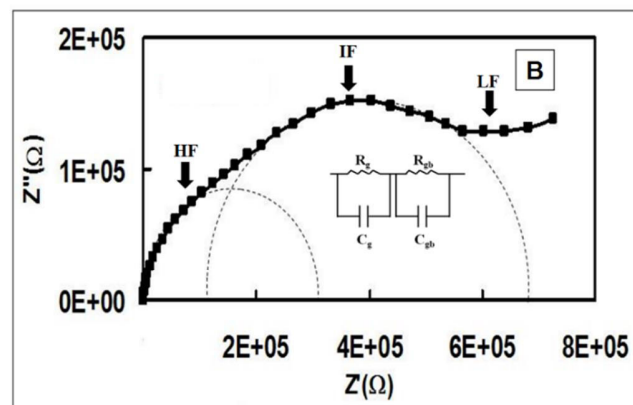


Fig.3.20. Nyquist plot of the imaginary part of impedance versus its real part for sample B at temperature of about 273 K. Indications are also given on the frequency range HF, IF and LF designating, high, intermediate and low frequency regimes respectively.

3.2.3c. Frequency and temperature dependence of conductivity

The electrical conductivities of the as- prepared samples A and B were determined from the dielectric measurements and graph is plotted between conductivity and frequency as shown in Fig.3.21. The conductivity curves display similar behavior for the two BiVO₄ samples. The dc conductivity can be inferred from low frequency region as summarized in frequency versus temperature plot (Fig.3.21). The obtained values depend on the milling times and also on the temperature through thermally activated conduction process. The semi-log plot of σ_{dc} versus the inverse of temperature ($1000/T$) yield Arrhenius activation energy,

$$\sigma_{dc}^i(T) = \sigma_0^i \cdot \exp\left(-\frac{E_a^i}{kT}\right) \dots\dots\dots (3.2)$$

where σ_0^i is pre-exponential factor and k is the Boltzmann constant.

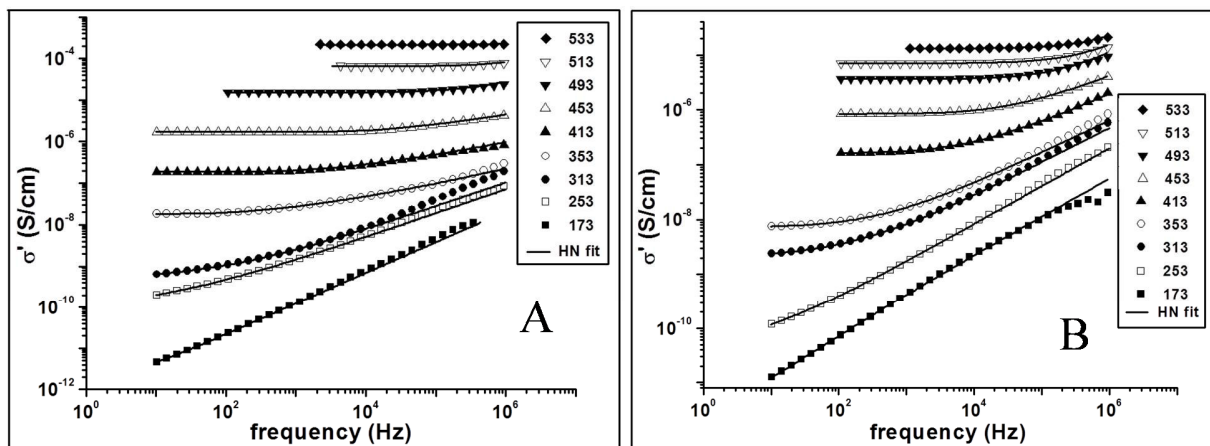


Fig.3.21. Frequency dependence (σ') of real part of conductivity $\sigma'(\omega)$ for different temperatures: a) A sample and b) B sample. The continuous lines are fits by Havriliak-Negami model.

However, two regimes are involved with different activation energies (E_a^i). The cross-over temperature between two regimes is found to be around $T_c = 300$ K. The activation energies for samples A and B was found to be about 0.621 eV and 0.242 eV respectively in the temperature range of 373-533 K while the activation energies change to 0.142 eV and 0.123 eV in the temperature range 173-293 K. Low activation energies are required for longer milling times and indicate low barrier heights in the conduction channels. These properties can be correlated with the microstructure of the samples. Indeed, sample A is composed of smaller nanoparticles

compared to sample B. Also, the microstructure with low density of interfaces requires low activation energies for the charge carriers.

3.2.3d. Temperature dependence of relaxation times

The relaxation times determine the dynamics of processes induced in the samples either by dipolar relaxation or charge carrier mobility under alternative voltages. As shown from dielectric functions discussed above, the relaxation mechanisms are too complex to be analyzed or accounted by unique relaxation time as it can be understood from Debye model [49]. A distribution of relaxation times (DRT) is more relevant and may be accounted for by the well-known Havriliak-Negami model. In this case, the parameters (α, β) define the shape of the dielectric functions and information on the occurrence of DRT. During the adjustment of the experiments by HN model, (α, β) were varied as function of temperature in the range [0.6-1.0] but no clear tendency is inferred. What can be addressed is only the relevance of DRT in the investigated samples. The relaxation time τ_{\max} (Fig.3.22) was determined by fitting the dielectric

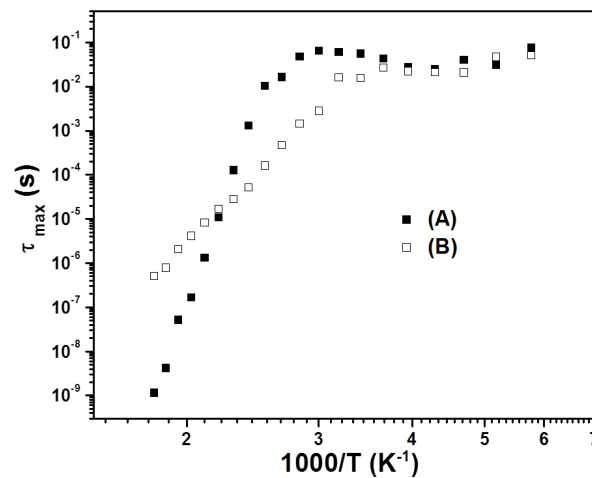


Fig.3.22. Temperature dependence of dc conductivity in BiVO₄ obtained under different synthesis conditions of samples A and B.

function curves $\epsilon'(F)$ and $\epsilon''(F)$ (Fig.3.19). Comparing the fitted values with those deduced, it is possible from the maximum of $\epsilon''(F)$, namely $\frac{1}{2\pi\tau_{\max}}$, the obtained values of τ_{\max} is quite good with the experimental values. In another instance, when the frequency maximum is not

clearly defined or is outside the range of frequency, only the evaluated value is reported, by fitting, as τ_{\max} .

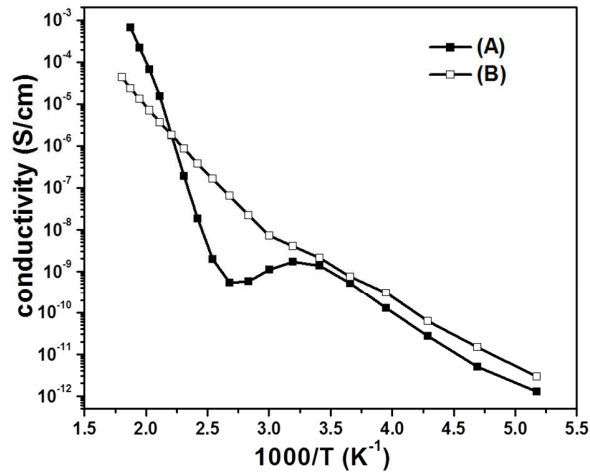


Fig.3.23. Variation of the relaxation time versus the inverse temperature for samples A and B.

For both samples, the average relaxation time is stationary at low temperatures. However, as temperature rises to 350 K as for sample A, the relaxation time decreases abruptly,

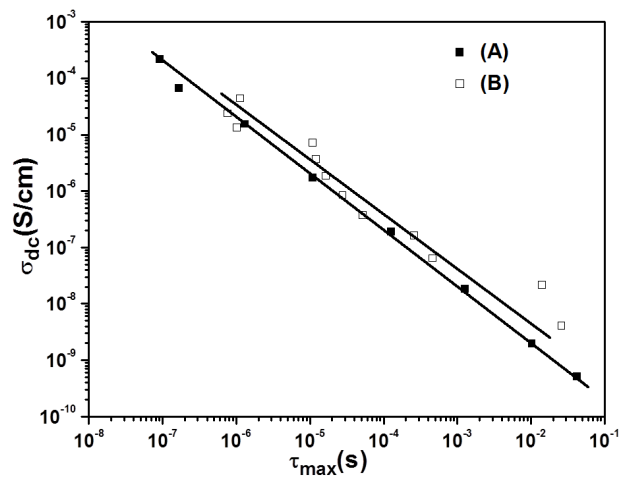


Fig.3.24. Log-log plot of the dc conductivity versus the relaxation time for samples A and B.

while it decreases nominally for sample B at 310 K. Such behavior is intimately correlated with the thermal evolution of the dc conductivities (Fig.3.23) which show changes in the activation energies of charge carriers. An additional argument supporting the intimate link between σ_{dc}

and τ_{\max} is illustrated in Fig.3.24 where these parameters are proportional to each other in the considered temperature range. This behavior was also demonstrated in nanostructured materials and a tentative explanation underlines the influence of the thermally activated charge motions on dielectric relaxation characteristic times [50].

To sum up, the thermally activated conductivity of two representative nanostructured BiVO₄ samples is in the order of 10⁻³-10⁻⁴ S/cm at T = 533 K. Two main thermal evolution regimes were demonstrated with a crossover at critical temperature of about 310 K. The activation energies depend on the temperature ranges, microstructure and crystalline order of the samples which influence the barriers heights in the conduction channels.

3.2.3e. EPR investigations-theoretical background

The EPR signal may be induced by i) reduction of Vanadium ions ii) intentional doping of impurities or iii) presence of impurities or doping ions in the chemical reactants used for BiVO₄ synthesis. Indeed, in a perfect crystalline structure, vanadium ions have valence state V⁵⁺ and then no EPR signal will be observed. If oxygen vacancies occur due to organisation or morphologies of the samples as nanoparticles with high specific surfaces, some vanadium ions can be reduced to V⁴⁺. This is favoured by the possibility of V⁴⁺ to adopt octahedral as well as pyramidal oxygen environments which may occur at the outermost particle surfaces or when vacancies are involved in the bulk. The resulting electronic configuration of reduced vanadium ions, V⁴⁺ (3d¹), possesses an effective electronic spin (S=1/2) giving rise to an EPR signal. In addition, the vanadium nuclei with the main isotope ⁵¹V (99.5%) is characterized by nuclear spin (I=7/2) which gives rise to characteristic substructures on the EPR spectrum (hyperfine splitting). From theoretical point of view, the interactions of vanadium ions is a consequence of coupling between electronic spin and external magnetic field (Zeeman interaction) as well as between electronic and nuclear spin (hyperfine interaction). The interactions define the spin Hamiltonian as:

$$\hat{H} = \beta \left(B_x g_x \hat{S}_x + B_y g_y \hat{S}_y + B_z g_z \hat{S}_z \right) + \left(A_x \hat{S}_x \hat{I}_x + A_y \hat{S}_y \hat{I}_y + A_z \hat{S}_z \hat{I}_z \right) \text{-----} (3.3)$$

In this expression, β represents Bohr magneton and the frame (x,y,z) refers to principal axes of g-tensor with the components $g_{x,y,z}$. The components $B_{x,y,z}$ are related to applied static magnetic field and $A_{x,y,z}$ represent the hyperfine tensor (A-tensor) parameters which characterize

the strength of hyperfine coupling [51]. The experimental EPR spectra are adjusted by using Bruker-Winsinfonia software and considering the interactions as summarized above. The procedure of fitting determines the magnetic fields (B_{ir}) related to all transitions between spin states (both electronic and nuclear states are considered as well). By using derivative of Lorentzian lines centred at different B_{ir} and using suitable line width we can reproduce precisely all parameters of the experimental spectra. This allows extracting g_x, g_y, g_z components and the hyperfine coupling parameters summarized in table 3.3 as discussed in details in next paragraph.

Table 3.3. EPR spectral parameters of V^{4+} in $BiVO_4$ for samples A and B.

Samples	Ax	Ay	Az	Gx	gy	gz	ΔH_x	ΔH_y	ΔH_z
A	30	72	199	1.97	1.980	1.930	75	30	100
B	20	75	200	1.97	1.985	1.930	25	30	85

The spectral parameters reflect the symmetry of local environments around paramagnetic ions as well as the electronic wave functions and residence probabilities of unpaired electrons close to the nuclei. Particularly, the g-tensor components exhibit departures ($\Delta g_{x,y,z}$) with respect to the Landé g-factor of free electron ($g=2.0023$). These shifts depend on the spin-orbit coupling and on the energies of fundamental and excited orbitals occupied by unpaired electrons. Interpretation of the parameters gives information about the environments of V^{4+} ions and their electronic properties contributing to better understanding of conductivity in this type of materials and also their relevance in catalytic processes.

3.2.3f. EPR spectral analysis

EPR spectra recorded for two representative samples A (11 hr10:1) and B (24hr5:1) (Fig.3.25 (a, b)) reveal anisotropic behaviour due to magnetic and hyperfine tensors leading to different substructures. The simulation of EPR spectra requires two main contributions (Fig.3.25 c); the first anisotropic signal is related to isolated V^{4+} ions with orthorhombic local symmetry. The second contribution consists of a single broad line (200 Gauss as line width) without any details such as hyperfine structure or resolved substructure. Vanadium pairs or clustering of V^{4+} ions can account for the broad background absorption line. In all samples, anisotropic EPR spectrum is characterized by g-tensor reflecting an orthorhombic local symmetry around V^{4+} with almost the same components $g_x = 1.970$, $g_y = 1.985 - 1.980$, $g_z = 1.935 - 1.930$. This

is understood by the occurrence of similar electronic structure and local environment of V^{4+} in $BiVO_4$ irrespective of the sample microstructures (A, B). From a theoretical view, the electronic structure of $3d^1-V^{4+}$ ions in tetrahedral environment consists of fundamental state $d_{x^2-y^2}$ with energy $E_{x^2-y^2}$ and the excited states as d_{xy} , d_{xz} , d_{yz} with energies $(E_{ij}(xy, xz, yz))$. Components of the g-tensor can be expressed in terms of spin-orbit coupling between the fundamental and excited states [52] as in equation (3.4) below.

$$\begin{aligned}
 g_x &= g_e - \frac{2\lambda_0 \chi_{x^2-y^2}^2 \chi_{yz}^2}{(E_{x^2-y^2} - E_{yz})} \\
 g_y &= g_e - \frac{2\lambda_0 \chi_{x^2-y^2}^2 \chi_{xz}^2}{(E_{x^2-y^2} - E_{xz})} \dots\dots\dots (3.4) \\
 g_z &= g_e - \frac{8\lambda_0 \chi_{x^2-y^2}^2 \chi_{xy}^2}{(E_{x^2-y^2} - E_{xy})}
 \end{aligned}$$

with $g_e = 2.0023$ for a free electron, λ_0 the spin-orbit coupling and χ_{ij}^2 the fraction of d_{ij} anti-bonding orbitals of the Vanadium based complexes. Such equations are used to understand roughly the behaviour of electronic configuration related to V^{4+} ions. From the values of g-tensor components it is noticed that the local symmetry is nearly axial with $g_{\perp} \approx \frac{g_x + g_y}{2} \approx 1.978$ and $g_{\parallel} = 1.933$. Splitting of the electronic diagram related to V^{4+} may then be assigned to $\Delta_{\parallel} = E_{x^2-y^2} - E_{xy} < \Delta_{\perp} \approx E_{x^2-y^2} - E_{yz} \approx E_{x^2-y^2} - E_{xz}$. By using the free vanadium ion spin-orbit coupling parameter $\lambda_0 \approx 240 \text{ .cm}^{-1}$, $\Delta_{\parallel} = 12500 \text{ .cm}^{-1}$, $\Delta_{\perp} = 14400 \text{ .cm}^{-1}$, and considering the fraction of fundamental orbital $d_{x^2-y^2}$ in the anti-bonding wave-function as $\chi_{x^2-y^2}^2 = 1$, a rough estimation is then given for the contributions of excited states $\chi_{xz}^2 = \chi_{yz}^2 = 0.6$ and $\chi_{xy}^2 = 0.5$. These fractions of excited states in the wave-function of unpaired d-electron are quite high, hence the optical transition probabilities and sample absorption may be enhanced on a wide range of the visible spectrum. Thus, electronic configurations of reduced vanadium influence the optical absorption and charge transfer mechanism which may contribute to the photocatalytic activity of $BiVO_4$. On the other hand, a correlation between conductivity

and EPR measurements can be discussed to understand whether V^{4+} ions can act as charge carriers or charge traps in conduction channels. In this aim, the concentration of V^{4+} ions was evaluated and compared between both samples (A, B). This concentration is determined from the integrated line intensity of the EPR signal and compared to a reference sample [53]. In the sample A, concentration of $[V^{4+}]_A = 4.10^6 \text{ spin/gran}$ is one order of magnitude less than sample B ($[V^{4+}]_B = 4.10^7 \text{ spin/gran}$). Thus, sample B favour a high concentration of reduced vanadium ions, at the same time, the conductivity is also higher. So, with respect to $V^{5+} - O^{2-}$ molecular bonds which account for the charge transfer within crystalline structure, V^{4+} ions seem to favour the conductivity in samples.

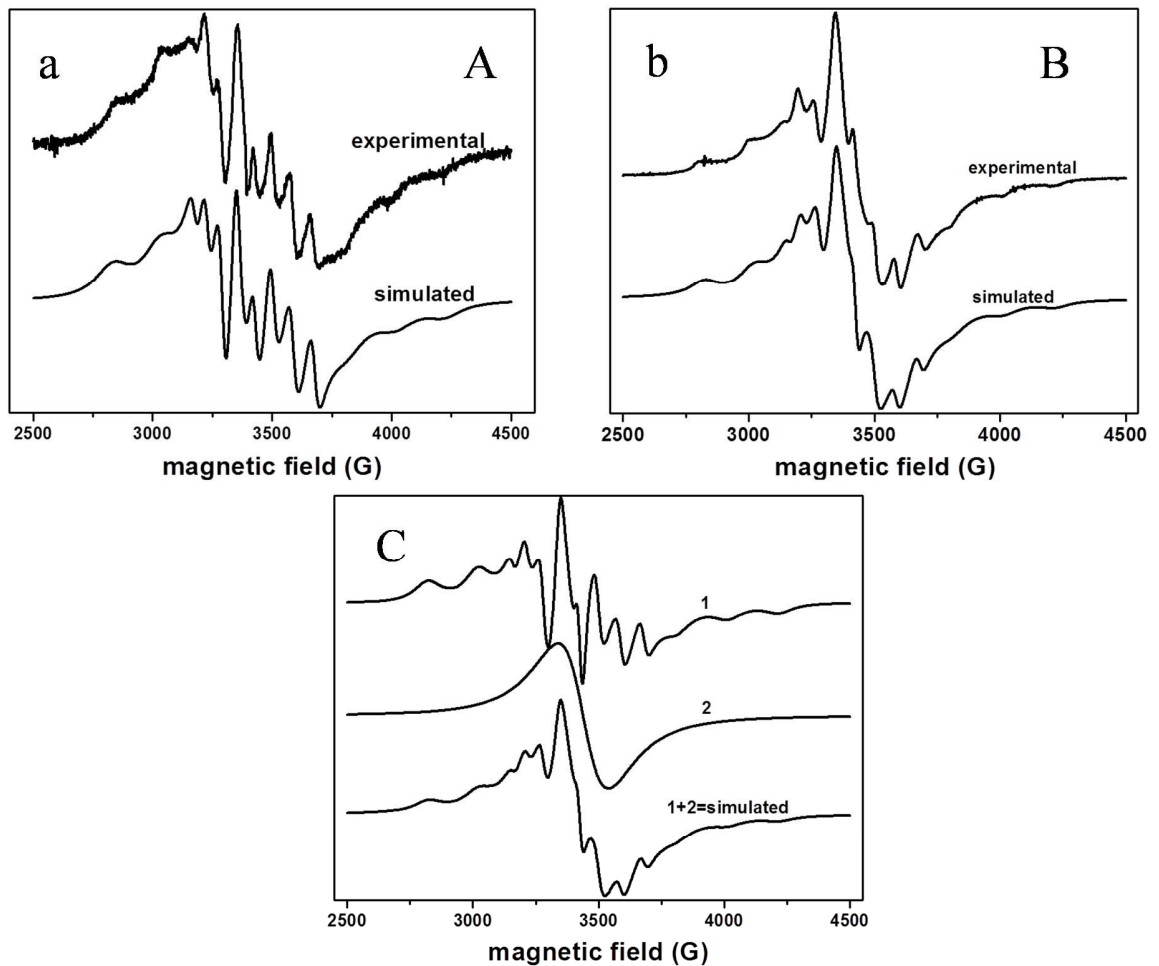


Fig. 3.25. EPR spectra of $BiVO_4$ samples A and B. The graph (C) illustrates the contributions to the vanadium EPR spectrum from (1) anisotropic signal of isolated V^{4+} and (2) background signal of V^{4+} pairs or emanating from clustering of V^{4+} ions.

3.3. Reproducibility test of ball milled BiVO₄

A Complex (hydrothermal process) and simple synthesis route (mechanochemical process) to synthesize monoclinic phase of BiVO₄ has been described in the above section. However, the phase formation, morphology and the crystalline structures are highly sensitive to the synthesis route used in its preparation. If the practical applications are to be achieved, it is also necessary for the synthesis method to be (i) controllable, (ii) reproducible and (iii) cheap. A variety of methods for synthesis of pure and doped BiVO₄ have been reported [54, 56] none of which meets all these conditions. Such observations are also reported for N-doped TiO₂ [57, 58].

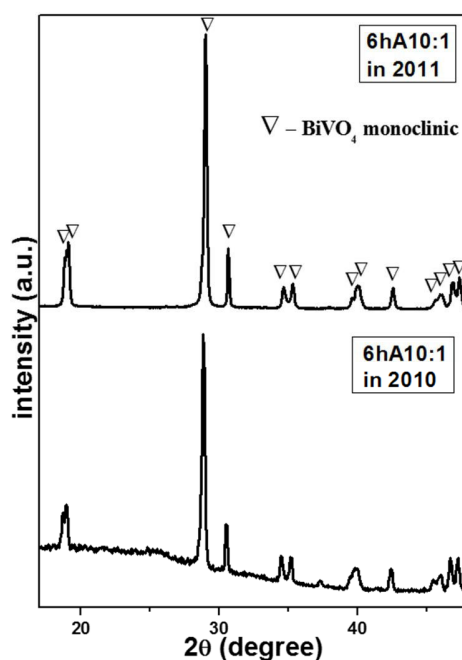


Fig.3.26. XRD patterns of as-synthesized BiVO₄ powders aged at different time.

Mechanochemical synthesis process is an advantageous technique, since the number of precursors used to prepare pure monoclinic BiVO₄ compound is minimum. Thermal treatment of BiVO₄ in the atmosphere of air results in significant improvement of crystalline structure. In order to determine the optimum synthesis parameters for preparing better photocatalysts, samples of precursors were milled for various milling time, BPR and milling atmosphere and then the final products were characterized by various techniques and discussed. Photocatalytic testing of these materials showed that, 6 h milled with 10:1 BPR and 400 RPM produced an effective visible-light active photocatalyst and showed improved photodegradation of Rh6 and MB as compared to 11 h and 16 h milled samples (as reported in chapter 5, section 5.2.2). According to these results, 6 h milled with 10:1 BPR sample is considered to be the optimized one. XRD was,

performed on this optimized sample that, shows peaks at 15.0° , 18.5° , 35.0° and 46.0° corresponding to the monoclinic scheelite phase of BiVO_4 (Fig 3.26, 6hA10:1 in 2010) The same optimized conditions were used after a year to check the crystalline nature and the XRD results displayed high reproducibility of BiVO_4 samples (Fig.3.26, 6hA10:1 in 2011).

FE-SEM images in Fig.3.27 shows clear spherical shape of BiVO_4 particles. The crystal size of BiVO_4 was estimated to be ~ 60 - 150 nm. This result was in good agreement with the evaluation obtained using a Scherrer equation based on the XRD patterns. There is no change in morphology and particle size of as synthesized BiVO_4 even after one year of aging process. This ensures that, based on the above optimal conditions BiVO_4 synthesis exhibits highly reproducible results.

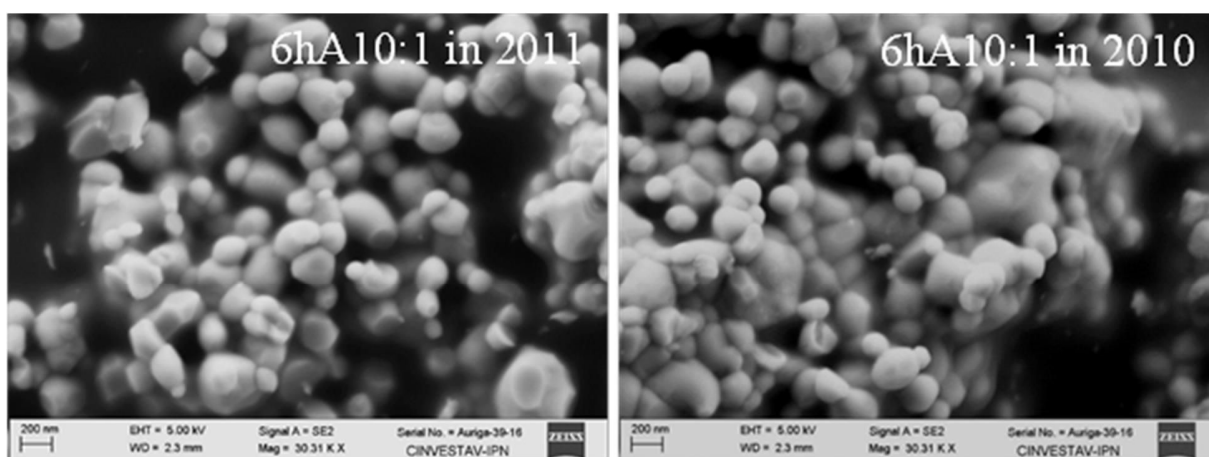


Fig.3.27. FE-SEM micrographs of as-synthesized BiVO_4 powders aged at different time.

3.4. Conclusion

Monoclinic scheelite BiVO_4 of different morphologies such as needle-like, sphere-like, cauliflower-like, porous-like and microclusters-like aggregates of uniform sizes were synthesized using hydrothermal method by adjusting pH and varying the surfactants. It was found that pH and surfactants, significantly influenced the morphology, crystalline order and light absorption of the as-obtained BiVO_4 . Relatively high pH (pH = 9) helps in forming acicular morphology, with improved crystalline order and expected to exhibit promising application as visible-light driven photocatalyst for the degradation of organic dyes. The unique formation of BiVO_4 particles

through hydrothermal method, would be helpful for providing a deeper understanding of crystal growth during the hydrothermal process.

Mechanochemical method was used to prepare BiVO₄ nanoparticles which are of spherical shape with an average size of about 20 nm. It is found that the ball milling time can refine the grain size, crystalline order and agglomeration of particles. Additionally, annealing treatments performed at suitable temperature, time and atmosphere contribute to stabilize the monoclinic phase of BiVO₄. The relevant parameters for an optimized synthesis is minimal time duration of 6 h and BPR parameters as 10:1. The structural, morphological and dielectric behavior are modulated with respect to milling time and BPR ratio. This is for the first time that systematic investigations by dielectric and EPR spectroscopy were achieved.

As a concluding remark, based on the structural, optical and electrical properties, visible light active photocatalysts have been prepared by a low-cost mechanochemical method that allows controllable and reproducible BiVO₄. In addition, the mechanochemical process used in this work also provides many advantages such as one-step synthesis of nanomaterials, considerably uniform and small size particles, high purity product formation and an environmental friendly synthesis method. This method is well suited to scale up for the production of large quantities of material at an economic cost, thus paving a way for variety of new applications in environmental remediation, public health protection and self-cleaning processes.

References

1. Y.D. Liu, H. Zheng, Z. Yuan, Y. Zhao, J. Waclawik, E.R. Ke, X. Zhu, *J. Am. Chem. Soc.*, 2009, 131, 17885-17893.
2. M. Li, L. Zhao, L. Guo, *Int J Hydrogen Energy*, 2010, 35, 7127-7133.
3. F. Dong, Q. Wu, J. Ma, Y. Chen, *Phys. Status Solidi A*, 2009, 206, 59-63.
4. H. Jiang, H. Dai, X. Meng, K. Ji, L. Zhang, J. Deng, *Applied Catalysis B, Environmental* 2011, 105, 326-334.
5. L. Zhang, J. Long, W. Pan, S. Zhou, J. Zhu, Y. Zhao, Xinang, G. Cao, *Materials Chemistry and Physics*, 2012, 136, 897-902.
6. S. M. Thalluri, M. Hussain, G. Saracco, J. barber, N. Russo, *Ind. Eng. Chem. Res.*, 2014, 53, 2640-2646
7. S. Obregón, A. Caballero, G. Colón, *Applied Catal. B, Environ*, 2012, 117-118, 59-66.
8. Hardcastle, I.E. Wachs, *J. Phys. Chem.*, 1991 95 5031-5041.
9. J. Yu, A. Kudo, *Chem. Lett*, 2005, 34, 850-851.

10. L. Sandhya Kumari, P. Prabhakar Rao, A. Narayana Pillai Radhakrishnan, Vineetha James, S. Sameera, Peter Koshy, *Solar Energy Materials & Solar Cells*, 2013, 112, 134-143.
11. R. Venkatesan, S. Velumani, A. Kassiba, *Materials Chemistry and Physics*, 2012, 135, 842-848.
12. H. Li, G. Liu, S. Chen, Q. Liu, W. Lu, *Physica E*, 2011, 43, 1323-1328.
13. Bin Zhou, Xu Zhao, Huijuan Liu, Jiuhui Qu, C.P. Huang, *Separation and Purification Technology*, 2011, 77, 275-282.
14. A. Zhang, J. Zhang, N. Cui, X. Tie, Y. An, L. Li, *J. Mol. Catal. A, Chem*, 2009, 304, 28-32.
15. L. Zhou, W. Wang, H. Xu, S. Sun, M. Shang, *Chem. Eur. Journal*, 2009, 15, 1776-1782.
16. G. Xi, J. Ye, *Chem. Commun*, 2010, 46, 1893-1895.
17. L. Zhang, W. Wang, L. Zhou, H. Xu, *Small*, 2007, 3, 1618-1625.
18. Y.R. Ma, L.M. Qi, J.M. Ma, H.M. Cheng, *Langmuir*, 2003, 19, 4040-4042.
19. Y. Chang, J.J. Teo, H.C. Zeng, *Langmuir*, 2005, 21, 1074-1079.
20. L. Zhou, W. Z. Wang, S.W. Liu, L.S. Zhang, H.L. Xu, W. Zhu, *J. Mol. Catal. A, Chem*, 2006, 252, 120-124.
21. M. L. Zhang, T.C. An, X.H. Hu, C.Wang, G.Y. Sheng, J.M. Fu, *Applied. Catal. A, Gen*, 2004, 260, 215-220.
22. Xue Meng, Lei Zhang, Hongxing Dai, Zhenxuan Zhao, Ruzhen Zhang, Yuxi Liu, *Materials Chemistry and Physics*, 2011, 125, 59-65.
23. Ken Hirota, Goro Kosmotsu, Hideaki Takemura and Osamu Yamaguchi, *Ceramics international*, 1992 18 285-287.
24. A. Zhang, J. Zhang, *Spectrochimica Acta Part A*, 2009, 73, 336-341
25. K. Shantha, G. N. Subbanna, and K. B. R. Varma. *J. Solid State Chem.* 1999 142 41-47.
26. F. Gao, X. Chen, K. Yin, S. Dong, Z. Ren, F. Yuan, T. Yu, Z. Zou, J. M. Liu, *Adv. Mater.* 2007, 19, 2889-2892.
27. T. Hisatomi, C. Katayama, Y. Moriya, T. Minegishi, M. Katayama, H. Nishiyama, T. Yamada, K. Domen, *Energy Environ. Sci*, 2013, 6, 3595-3599.
28. T.S. Zhang, J. Ma, L.B. Kong, *J. Mater. Res*, 2006, 21, 71-74.
29. X. Lin, J. Xing, W. Wang, Z. Shan, F. Xu, F. Huang, *J. Phys. Chem. C*, 2007, 111, 18288-18293.
30. M.D. Segall, P.J.D. Lindan, M.J. Probert, C.J. Pickard, P.J. Hasnip, S.J. Clark, M.C. Payne, *J. Phys. Condens. Matter*, 2002, 14, 2717-2744.
31. B. Vidhya, S. Velumani, J.A. ArenasAlatorre, A. MoralesAcevedo, R. Asomoza, J.A. ChavezCarvayar, *Mater. Sci. Eng. B*, 2010, 174, 216-221.
32. K. Shantha, G.N. Subbanna, K.B.R. Varma, *J. Solid State Chem*, 1999, 142, 41-47.
33. V.V. Zyryanov, *Inorg. Mater*, 2005, 41, 438-464.
34. J. Yu, A. Kudo, *Chem. Lett*, 2005, 34, 850-851.
35. M. Anpo, Y. Kubokawa, *Rev. Chem. Intermed*, 1987, 8, 105-124.

36. M. Anpo, H. Nakaya, S. Kodama, Y. Kubokawa, K. Domen, T. Onishi, *J. Phys. Chem*, 1988, 90, 1633-1636.
37. D.H. Franklin, I.E. Wachs, *J. Phys. Chem*, 1991, 95, 5031-5041.
38. R.L. Frost, D.A. Henry, M.L. Weier, W. Martens, *J. Raman Spectrosc*, 2006, 37, 722-732.
39. A. Walsh, Y. Yan, M.N. Huda, M.M. Al-Jassim, S. Wei, *Chem. Mater*, 2009, 21, 547-551.
40. J. B. Liu, H. Wang, S. Wang, H. Yan, *Mater. Sci. Eng B*, 2003, 104, 36-39.
41. L. Zhang, D. R. Chen, X. L. Jiao, *J. Phys. Chem B*, 2006, 110, 2668-2673.
42. M. Gotic, M. Ivanda, M. Soufek, S. Popovic, *J. Mol. Struct.* 2005, 744, 535-540.
43. S. Charpentier, A. Kassiba, J. Emery, M. Cauchetier, *J. Phys. Cond. Matter*, 1999, 11, 4887-4897.
44. S. Havriliak, S. Negami, *J. Polym. Sci., Polym. Symp*, 1966, 14, 89.
45. B. Li, B. Tang, S. Zhang, H. Jiang, *J. Mat. Sci*, 2010, 45, 6461-6466.
46. A. Kassiba, M. Tabellout, S. Charpentier, N. Herlin, J. R. Emery, *Solid. Stat. Com*, 2000, 115, 389-393.
47. A. Dutta, C. Bharti and T. P. Sinha, *Mater. Res. Bull*, 2008, 43, 1246-1254.
48. B. Hirschorn, M. E. Orazem, B. Tribollet, V. Vivier, I. Frateur, M. Musiani *J. Electrochem. Soc*, 2010, 157, C452-C457.
49. J. Macutkevic¹, J. Banys¹, A. Matulis, *Nonlin. Anal. Model. Control*, 2004, 9, 75.
50. H. Jang, H. Dai, X. Meng, L. Zhang, J. Deng, Y. Liu, C. T. Au, *J. Environ. Sci.* 2012, 24, 449-457.
51. A. Kassiba, R. Hrabanski, D. Bonhomme, A. Hader, *J. Phys. Condens. Matter*, 1995, 7, 3339-3353.
52. G. Oversluizen, R. Metselaar, *J. Phys. C, Solid State Phys.* 1982, 15, 4869-4880.
53. B. Pattier, M. Henderson, A. Poppl, A. Kassiba, A. Gibaud, *J. Phys. Chem. B*, 2010, 114, 4424-4431.
54. H. Xua, H. Li, C. Wu, J. Chu, Y. Yan, H. Shu, Z. Gu, *Journal of Hazardous Materials*, 2008, 153, 877-884.
55. M. Shang, W. Wang, L. Zhou, S. Sun, W. Yin, *Journal of Hazardous Materials*, 2009, 172, 338-344.
56. J. B. Liu, H. Wang, S. Wang, H. Yan, *Mater. Sci. Eng. B*, 2003, 104, 36-39.
57. S. Sakthivel, H. Kisch, *ChemPhysChem*, 2003, 4, 487-490.
58. S. Livraghi, A. Votta, M. C. Paganini E. Giamello, *Chem. Commun*, 2005, 4, 498-500.

4. BiVO₄ thin films: Results and Discussions

Metal oxide semiconductor based photocatalysis plays an important role in the development of clean energy and environmental protection [1]. In this context, heterogeneous photocatalyst, bismuth vanadate (BiVO₄) has drawn much attention in recent years due to its visible light driven photocatalytic behavior [2]. BiVO₄ was mostly prepared in powdered form, mainly due to the advantages of simple equipment requirements and low cost. However, the powder catalyst has many drawbacks, such as separation of catalyst from the slurry system after photocatalytic reaction, necessity of stirring the mixture during the reaction and aggregation of suspended particles [3]. Thin films offer an alternative to overcome these difficulties by manipulating powders mainly when nanoparticles are involved. Therefore, BiVO₄ thin films possess promising properties for developing better photocatalyst. Various synthesis routes were adopted to prepare BiVO₄ thin films with different morphologies and structures. The aim of this study was to develop a novel synthesis approach with less cost and ability to generate materials with tunable band gap. Herein, for the first time, an additive-free ultrasonic spray pyrolysis (USP) and rf-sputtering deposition method for the controlled preparation of BiVO₄ thin films were demonstrated. This includes stabilization of monoclinic phase with large specific surface (area) due to nanostructured organization of crystalline islands. On the contrary, choosing defined parameters of synthesis induce flat surface film with relatively low roughness. Structural, morphological and optical properties of as-prepared BiVO₄ thin films were investigated and discussed in details.

4.1. Thin film deposition using ultrasonic spray pyrolysis

USP is an innovative method for the preparation of thin films with uniform particle size. It has several advantages over other traditional methods, such as production of micrometer-or-submicrometer sized particles, high purity product, continuous operation and easy control of sample composition. Moreover, aerosol methods are well-suited for large-scale production. Synthesis of BiVO₄ thin films using USP method was reported recently [4]. It should be noted

that most of the previous studies on the synthesis of BiVO₄ thin films uses reactants such as bismuth (III) nitrate pentahydrate and ammonium metavanadate. Here, the preparation of BiVO₄ thin films by a facile ultrasonic spray pyrolysis (USP) method is presented. Commercial compounds (bismuth (III) nitrate pentahydrate and ammonium metavanadate) as well as low cost ball milled BiVO₄ were used as precursors to prepare BiVO₄ thin films.

4.1.1. Effect of substrate temperature

The main parameters in USP, which affect the morphology of the films are, precursor's concentration, carrier gas flow rate and the substrate temperature (T_{sub}). Use of commercial precursors or ball milled BiVO₄ with varying substrate temperature (300 to 500 °C at an interval of 25 °C) were found to be ineffective in changing the morphology of the deposited thin films. Even though the deposition conditions were varied to a large extent, we limit the whole report to most important samples deposited for constant time of 15 min at various T_{sub} ; i.e. 350°, 400°, 425° and 500 °C.

4.1.1a. XRD analysis

XRD patterns of samples prepared at various T_{sub} are shown in Fig.4.1. The observed diffraction peaks correspond to monoclinic BiVO₄ (JCPDS no. 014-01688)[5]. The unit cell parameters are $a = 0.5195$, $b = 1.1701$, $c = 0.5092$ nm and $\beta = 90.38$. Monoclinic scheelite crystal phase of BiVO₄ is confirmed by existence of the characteristic peaks at 18.5°, 28.8°, 35° and 46° [6]. The crystallographic planes are also shown in Fig.4.1.

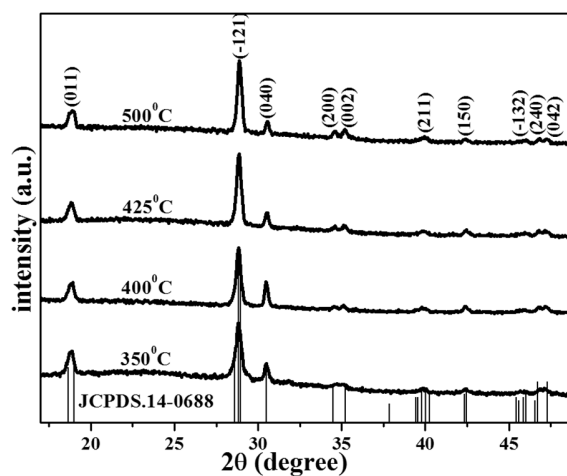


Fig.4.1. XRD patterns of BiVO₄ thin films deposited at different substrate temperatures.

Table 4.1. Structural parameters of USP deposited BiVO₄ thin films at different substrate temperatures.

Substrate Temperature (°C)	FWHM β (degree)	Crystallite size D (nm)	d (Å)	Strain ϵ $\times 10^{-3}$ Lines/m ²	Dislocation density $\delta \times 10^{15}$ Lines/m ²	Band gap E _g eV
350	0.295	29.0	3.097	1.3	1.18	2.20
400	0.268	32.1	3.093	1.1	0.97	2.14
425	0.246	35.0	3.092	1.0	0.82	2.09
500	0.230	37.4	3.087	0.9	0.71	2.07

No other diffraction peaks corresponding to secondary phases were detected, which suggested that the as-prepared BiVO₄ films are purely monoclinic in nature. In addition, narrow line widths of XRD pattern with increasing substrate temperature indicate an improvement of crystallinity with increasing T_{sub}. The full width half maximum (FWHM), crystal size, d-spacing value, strain and dislocation density were calculated and presented in table 4.1, from (-1 2 1) diffraction peak. Higher substrate temperatures are likely to result in higher surface mobility of BiVO₄ atoms propitiating the formation of larger crystalline grains. Systematic decrement in d-values (Table 4.1) was found with increasing T_{sub}, due to stress relaxation in the films deposited under higher substrate temperatures. Substrate temperature influences the strain and dislocation density significantly by reducing it, which also confirms the improvement of crystallinity. With increasing T_{sub}, it appears that the film growth along (0 0 2) plane starts and the orientation along the (0 4 0) gets suppressed, which is related to the anisotropic growth of the particles. The results suggested that, T_{sub} greatly affects the crystalline nature of BiVO₄ thin films.

4.1.1b. Surface morphological analysis by FE-SEM

Increase in the crystallite size along with decrease in strain and dislocation density occurs with increasing T_{sub}, is well evidenced from FE-SEM analysis. The morphologies of the as-prepared BiVO₄ thin films are depicted in Fig.4.2. It clearly reveals that the films are

homogeneous in nature and fine-grained microstructures occur with average grain size in the range of 40-200 nm. As the substrate temperature increases, there is no significant change in the morphology of the films, however, the particles become bigger in size. It is interesting to note that, the sample deposited at 350 °C is porous with poly dispersed islands of different sizes. This behavior of BiVO₄ island formation and latter transition to a continuous film suggest that the deposition time of 15 min is not good enough to form dense film at 350 °C. Such phenomena was observed and reported for other silver thin films, deposited using USP and even with other deposition techniques [7, 8]. With increasing T_{sub}, as-prepared BiVO₄ films have relatively smooth morphology and the particles are well connected to each other. It is clear that, crystallite size and densification of the film increases with increasing substrate temperature. Moreover, the film adheres strongly to the substrate and has tightly bound particles with crack-free surfaces. This indicates that the highly dense surface with larger grain size is favored by liquid-phase

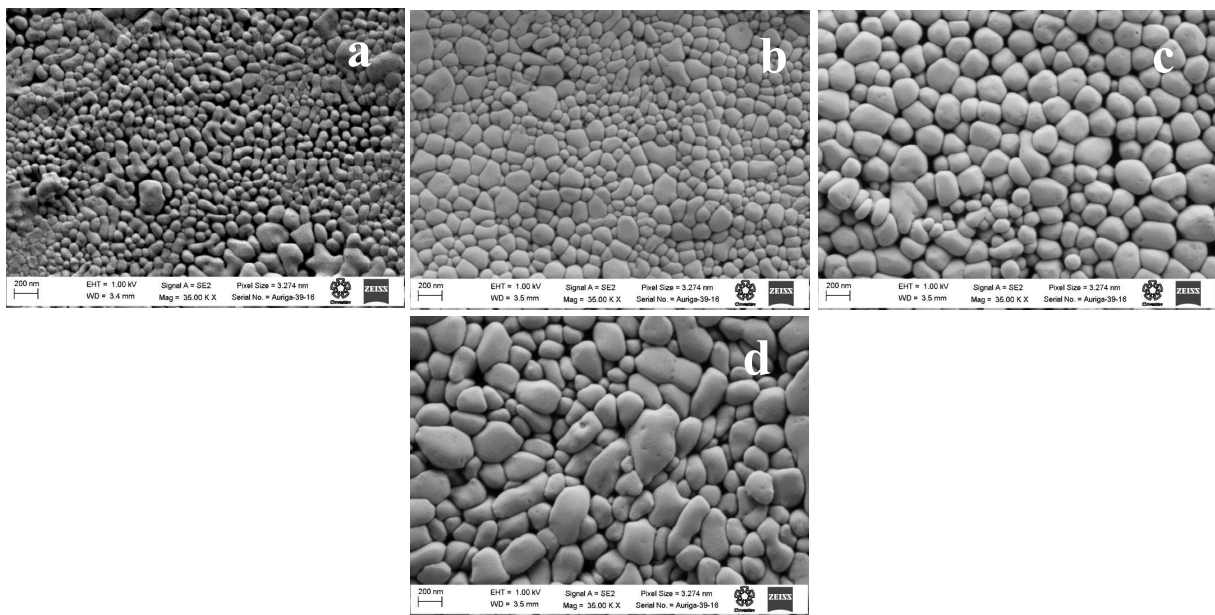


Fig.4.2. FE-SEM micrographs of BiVO₄ thin films deposited at different substrate temperatures a) 350°C b) 400°C c) 425°C and d) 500°C.

assisted re-crystalline process. A plausible explanation may be due to the high surface energy of precursors when deposited under high substrate temperature. In this case, the thermal energy is sufficient enough to favor a complete pyrolytic reaction between the reactant droplets leading to the formation of a more compacted film.

4.1.1c. HR-TEM and Raman analysis

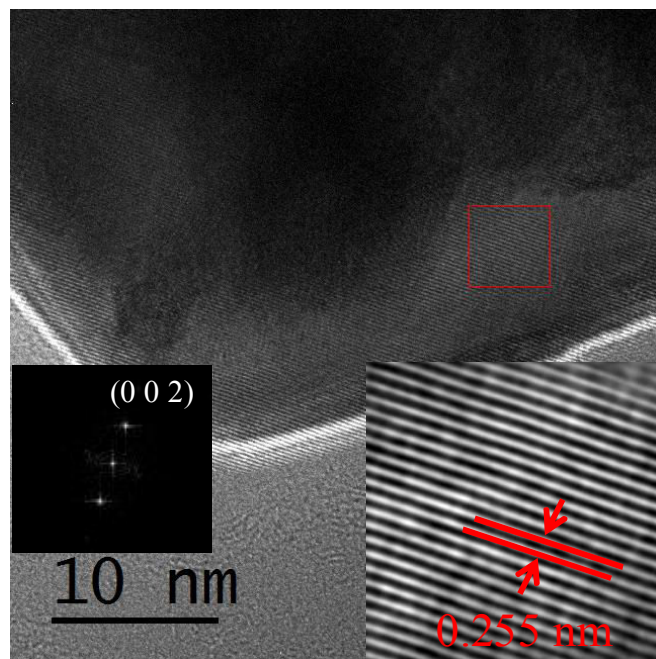


Fig.4.3. HRTEM images of 425°C deposited BiVO₄ film, inset shows FFT and inverse FFT of the selected area.

HR-TEM analysis was further used to identify the monoclinic structure and preferential orientation of BiVO₄ thin films. Fig.4.3, shows rim of the rounded shape ellipsoidal grains, and its insert exhibits FFT and inverse FFT of the selected area of BiVO₄ film deposited at 425 °C. HR-TEM image of this sample reveals sharp and clear lattice fringes indicating good crystalline nature of USP deposited film. Evidence for disordered grain boundary regions is also identified (edge of the rim). The d-spacing value measured from selected area electron diffraction (SAED) is 0.255 nm which agrees well with the lattice spacing 0.2546 nm for (0 0 2) of monoclinic BiVO₄ in XRD pattern. Thus, SAED pattern clearly indicates that the as-prepared films possess well crystalline monoclinic structure. The formation of monoclinic scheelite BiVO₄ structure was substantiated from the results of Raman studies. Fig.4.4 shows Raman spectra of BiVO₄ thin films obtained with different T_{sub}. Raman spectra of all the samples are characterized by six characteristic Raman modes of monoclinic scheelite BiVO₄ around 216, 333, 372, 640, 713 and 827 cm⁻¹. Raman modes at 827-833 cm⁻¹ and 713 cm⁻¹ correspond to the symmetric and anti-symmetric vibration of V-O stretching mode, respectively. The band at 640 cm⁻¹ is due to asymmetric V-O stretching mode.

The symmetric and anti-symmetric bending modes of vanadate anions are found at 372 and 333 cm^{-1} , respectively. The external modes (rotation/translation) were recorded at 216 cm^{-1} . The positions and full width at half maximum (FWHM) of the most intense peak near 827 cm^{-1} , were determined using Lorentzian-type curve fitting (Fig.4.5). A gradual shift of these Raman peaks towards the higher end of wavenumber, i.e., from 827 to 833 cm^{-1} , reveals that the average short-range symmetry of VO_4 tetrahedra becomes less regular. The differences in width and intensity of Raman peaks reflect variations in crystallinity, defect and disorder, particle size, and/or particle aggregation of these materials.

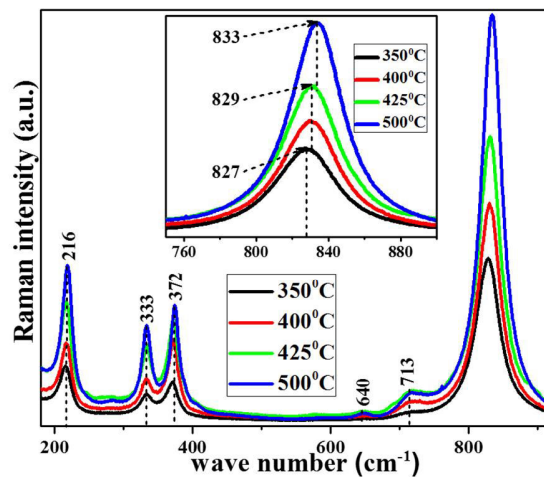


Fig.4.4. Raman spectra of BiVO_4 thin films deposited at different T_{sub} (inset: frequency shift with T_{sub}).

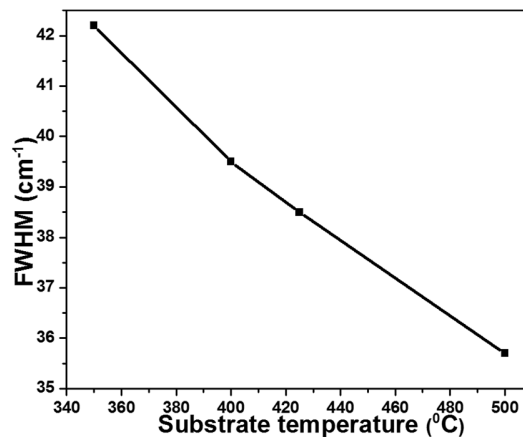


Fig.4.5. Dependence of FWHM of BiVO_4 thin films prepared at different substrate temperatures.

Results of Raman investigations indicate that the deposition parameters had an important effect on crystallinity of the films. Similar behavior was reported for other photocatalysts such as TiO_2 by Lin *et al* and Yang *et al* [9, 10]. They concluded that this effect is induced by variation in the particle size and surface atoms have a tendency to relax as in reconstructed surfaces. Such effects can lead to decreased FWHM values of Raman peaks, mainly when the surface possesses rough or well-connected particle morphologies of large crystallites. Raman investigations also points out that films deposited at higher substrate temperature show better crystallinity with lesser defects than samples prepared at lower T_{sub} (350 °C), probably due to the relationship between Raman stretching frequencies and the metal-oxygen bond length.

4.1.1d. UV-Visible absorption studies

Fig.4.6 shows the UV-Vis absorption spectra of BiVO_4 thin films deposited at different T_{sub} for 15 min. It was found that each sample showed different absorption profile in visible light region in addition to that of strong absorption in the UV and IR spectral regions. The absorption edge of BiVO_4 films are modified with T_{sub} due to different degree of crystallization and morphology of the films. The prolonged absorption tail in UV-Vis spectrum should result from the crystal defects formed at instantly high substrate temperature during ultrasonic spray deposition [11]. Noticeable shift in the absorption edge further broadened the visible-light absorption range. The energy band gap of BiVO_4 film was estimated from $(\alpha h\nu)^2$ versus photon energy ($h\nu$) plots as shown in the Fig.4.6 (inset). For the as-grown BiVO_4 thin films deposited at 350°, 400°, 425° and 500 °C, the optical energy gap was 2.20, 2.14, 2.09, 2.07 eV respectively (table 4.1). Therefore, the measured band gap energies for all samples are smaller than that of bulk BiVO_4 (2.3 eV [12, 13]). The narrow band gap of BiVO_4 film deposited at 425°C, indicates that this sample has lower conduction band level, which will increase the absorption characteristic for visible light.

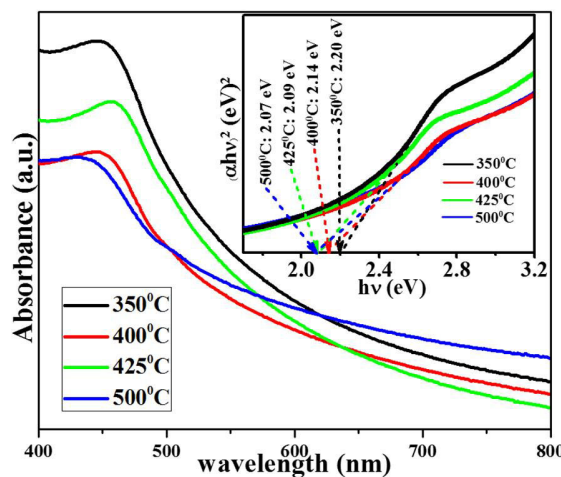


Fig.4.6. UV - Visible spectra of BiVO_4 thin films. Inset shows plot of $(\alpha h\nu)^2$ against $(h\nu)$.

As T_{sub} increases, band gap of BiVO_4 thin films decreases due to the increased packing density of the films [14]. This can be understood from FE-SEM micrographs (Fig.4.2) which indicates that, the increase in T_{sub} is related to increased grain size with uniformity and homogeneous distribution due to their coalescence. The origin of the variation in the optical band gap can also be explained by Burstein-Moss effect [15], band narrowing effect [16] and stress effect [17]. However, the Burstein-Moss effect can be applied to the increased band gap. Furthermore, films are deposited on non-conducting substrates (microslides), which confirms that, the deposited films are electrically insulating. Therefore, the physical origin of the smaller band gap is associated with the compressive stress effect. Similar behavior was also observed for the traditional photocatalysts, such as, YVO_4 [18], ZnO [19] and TiO_2 [14].

4.2. Thin film deposition using RF-Sputtering

Thin film deposition of BiVO_4 has been carried out using various techniques but to best of our knowledge, no reports are available on rf-sputtered BiVO_4 . The interest in application of rf-sputtering is due to several advantages like; good homogeneity, ease of composition control, large area deposition, good reproducibility and high sputtering efficiency. Moreover, films prepared by rf-sputtering have compactness, flatness and adhesion with substrates [20]. Preparation of BiVO_4 thin films using rf-sputtering technique is reported in this section.

An attempt has been made to optimize deposition parameters namely, rf-power, working pressure, substrate temperature and deposition chamber atmosphere to obtain monoclinic scheelite phase of BiVO_4 thin films. Thin films obtained under Ar atmosphere are found to be amorphous irrespective of experimental parameters. In this context, since crystallization temperature should be determined by annealing, in-situ HT-XRD measurement technique was performed to define the temperature range of crystallization. Structural, morphological and optical properties of BiVO_4 thin films prepared at various rf-sputtering parameters (different substrate temperatures with Ar and Ar+ O_2 atmosphere and oxygen flow rate) were investigated to achieve optimized parameters for the targeted applications in photocatalysis.

4.2.1. Effect of substrate temperature under Ar atmosphere

4.2.1a. Optimization of Crystallization temperature (HT-XRD) Room temperature XRD analysis, conducted prior to the in-situ HT-XRD experiments, indicates that the deposited films are amorphous. For the as-deposited thin films, a broad peak at the intense position (28.8°) was observed, indicating the formation of BiVO_4 amorphous films. 3D reaction pathway plots for HTXRD experiments conducted at different temperatures are shown in Fig.4.7. The in-situ HT-XRD data indicated the formation of BiVO_4 monoclinic phase around an annealing temperature of 276°C and monitored continuously up to 446°C . The formation of BiVO_4 monoclinic phase occurs within temperature range of 276°C - 408°C . However, it is interesting to note from the XRD plot (3D plots) Fig.4.7 that, when the temperature is above 408°C , the tetragonal phase of BiVO_4 appears as can be inferred from the additional peaks, at 22.9° and 31.8° . Thus, the phase transformation of the film occurs at critical temperature of about 408°C . However, appropriate annealing temperature leads to well crystallized BiVO_4 with the monoclinic scheelite phase (Table 4.2). It is also noticed that the particle size increases with increase in the annealing temperature while strain and dislocation density decreases. Based on these facts, it has been concluded that a suitable annealing temperature of around 400°C is required for crystallization of monoclinic phase BiVO_4 thin films that was deposited under Ar atmosphere.

Table 4.2. Structural parameters of In situ HT-XRD for BiVO_4 film deposited at room temperature under argon atmosphere.

Temperature ($^\circ\text{C}$)	FWHM (degree)	Crystallite size (nm)	Strain ($\epsilon \cdot e^{-3}$)	Dislocation density ($\delta \cdot e^{15}$)
276	0.4108	20	6.9	2.3
295	0.3940	21	6.7	2.12
314	0.3868	22	6.5	2.04
332	0.3806	22	6.4	1.98
351	0.3720	23	6.33	1.89
370	0.3698	23	6.28	1.86
389	0.3470	24	5.9	1.64
408	0.3115	27	5.3	1.32

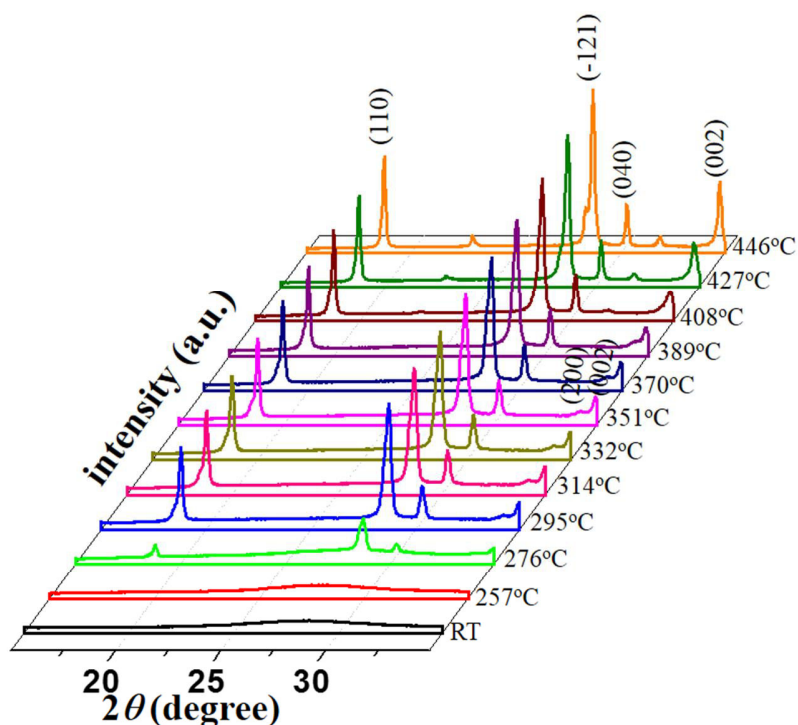


Fig.4.7. HT-XRD pattern of BiVO_4 film deposited at room temperature and annealed in situ (inside XRD system) under argon atmosphere.

4.2.1b. XRD and Raman analysis

The structure of the deposited films at substrate temperature of 450 °C and at room temperature was investigated by XRD. Similarly, structural characterization of BiVO_4 thin films of post-annealed at 400 °C has also been investigated using XRD. The corresponding XRD patterns of thin films are shown in Fig.4.8 (A) and (C). XRD patterns in Fig.4.8 (A) exhibited only a broad peak centered at $2\theta \sim 28.8^\circ$, (-121), indicating that the deposited films exhibit nanocrystalline structure with amorphous nature. This reveals that the substrate temperature or ion bombardment does not provide required activation to form polycrystalline film. In post-annealed samples, XRD patterns, showed the presence of (0 2 0), (0 1 1), (-1 2 1), (0 4 0), (2 0 0), (0 0 2), (2 1 1), (0 5 1), (1 3 2) and (0 4 2) peaks in Fig.4.8(C) thus confirming that they exhibit monoclinic phase [6]. The annealed films show sharp and intense peaks due to the improvement of crystallinity, as compared to deposited films which possess broad (-1 2 1) peak. The observed diffraction peak positions are found to be in good agreement with JCPDS-14-0688 [5], confirming the formation of single monoclinic phase BiVO_4 (space group $I2/a$), hence the

annealing temperature has significant effect on the crystallinity of the films. The peak broadening arises from dislocations and stacking faults. Strain also increases the peak width and, thereby, decreases the crystallite size as determined by Scherrer formula (equation 2.2, Chapter 2). Such broadening can also be introduced by surface tension and reconstructions that occur on nanocrystal surfaces. Diffraction peak shifts were analyzed based on intense peak of BiVO₄ at 28.8° (- 1 2 1). The displacement of highest peak of monoclinic BiVO₄ at (- 1 2 1) peak towards higher angles from 28.8° to 28.9°, could be seen from the insert in the upper right of Fig. 4.8 (C). This suggests that the distortion that occurred in BiVO₄ lattice is due to the changes in d-spacing thus consequently increases the cell volume. Indeed, microstrain comes from locally generated stress mainly due to the presence of dislocations and point defects. Such stress results in non-uniform changes in atomic distances and causes the broadening of diffraction line around an average atomic position. Lattice structure of BiVO₄ is monoclinic in nature and unit cell parameters have been determined for the post annealed optimized films and presented in table 4.3. The average crystallite size (D) of post-annealed BiVO₄ thin films was calculated using Scherrer formula (equation 2.2, chapter 2). Increment in the crystallite size was observed with increasing substrate temperature indicating the coalescence of particles due to the effect of annealing. The structural changes discussed above were confirmed by Raman spectroscopy of post-annealed BiVO₄ thin films as shown in Fig.4.7 (B) and (D). The intense Raman peak at 828 cm⁻¹ could be assigned to the symmetric stretching mode of V-O bond. The band at 208 cm⁻¹ is related to external mode (rotation/translation) of BiVO₄; the bands at 325 and 367 cm⁻¹ are due to the asymmetric and symmetric deformation modes of VO₄³⁻ tetrahedron, respectively [21]. Raman analysis showed that BiVO₄ film was well crystallized with the monoclinic structure, which was in accordance with the result of XRD observation (Fig.4.8C).

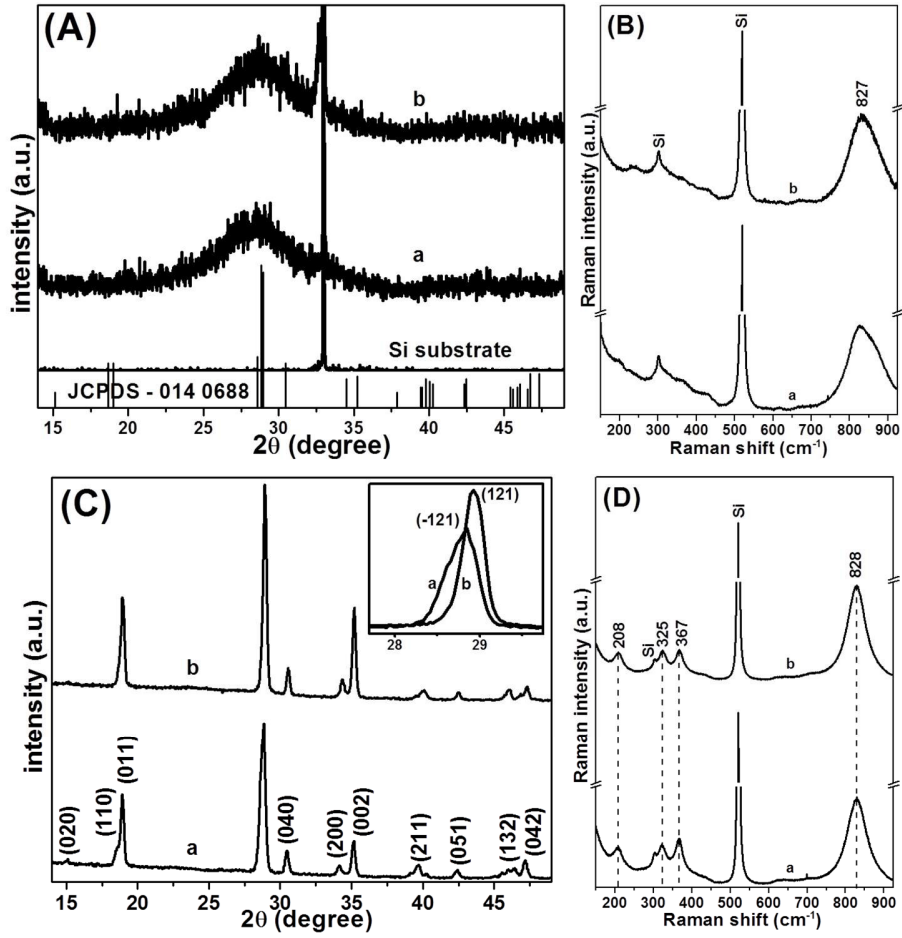


Fig.4.8. XRD patterns and Raman spectra of BiVO_4 thin films deposited at different substrate temperatures: a) RT deposited and b) deposited at 450°C . (A) and (B) as-deposited thin films, (C) and (D) post-annealed at 400°C thin films.

Table 4.3. Structural parameters of BiVO₄ post annealed (400 °C) thin films.

Samples	d – spacing (Å)			Lattice parameters (Å)				2θ ^o	FWHM (2θ ^o)	Crystallite Size (nm)	Strain ε * e ⁻³	Dislocation density δ * e ¹⁵
	(hkl)	Observe	JCPDS	a	b	c	JCPDS					
a	(-121)	3.0947	3.0950	5.154	11.702	5.104	a = 5.195 b = 11.701 c = 5.092	28.84	0.428	25.8	7.267	1.502
b	(121)	3.0865	3.0820	5.081	11.707	5.100		28.93	0.254	36.0	4.295	0.772

4.2.1c. Surface morphological analysis by FE-SEM and AFM

The change in uniformity and homogeneity with varying substrate temperature is visualized from FE-SEM analysis. Fig.4.9 shows the surface microstructure of BiVO₄ films deposited with varying substrate temperature on n-type Si (100). Nanocrystalline grains are observed for RT deposited film and Fig.4.9 (a) shows good homogeneous surface with round-shaped particles having uniformity throughout the film. Size of these particles, evaluated from the FE-SEM micrograph (using the magnification bar), shows an average grain size of about 15-25 nm which is in good agreement with crystallite size of about 25 nm as determined by Scherrer equation. Silva *et al* [22] reported, enhanced photoelectrochemical degradation of methylene blue with about ~350 nm grains of BiVO₄ thin film. The present work reports sphere like particles with improved homogeneity and much reduced particle size, so it can be stated that this compound in the form of thin film may act as promising candidate for the degradation of organic pollutants. But the films deposited at 450 °C (Fig.4.9 (b)) exhibited relatively dense and smooth surfaces with well-packed grains. It is discerned that the grains are growing in parallel to the substrate surface. On the contrary, superficial cracks due to crystalline grain growth were evident after thermal annealing (Fig.4.9 (b)). Variation in the surface morphology indicates that

the crystalline nature of film is improved with substrate temperature in agreement with XRD results.

Influence of substrate temperature and annealing on the morphologies of BiVO_4 films were examined by atomic force microscopy (AFM). Fig.4.10 shows AFM images of BiVO_4 films deposited on Si and annealed at 400°C for films deposited at RT (Fig.4.10 (a)) and 450°C (Fig.4.10 (b)). For the RT deposited film (Fig.4.10 (a)) spherical particles were observed on the surface of the film, confirms the formation of BiVO_4 nanocrystallites of size around 10-25 nm, with slight aggregation due to coalescence of the grains.

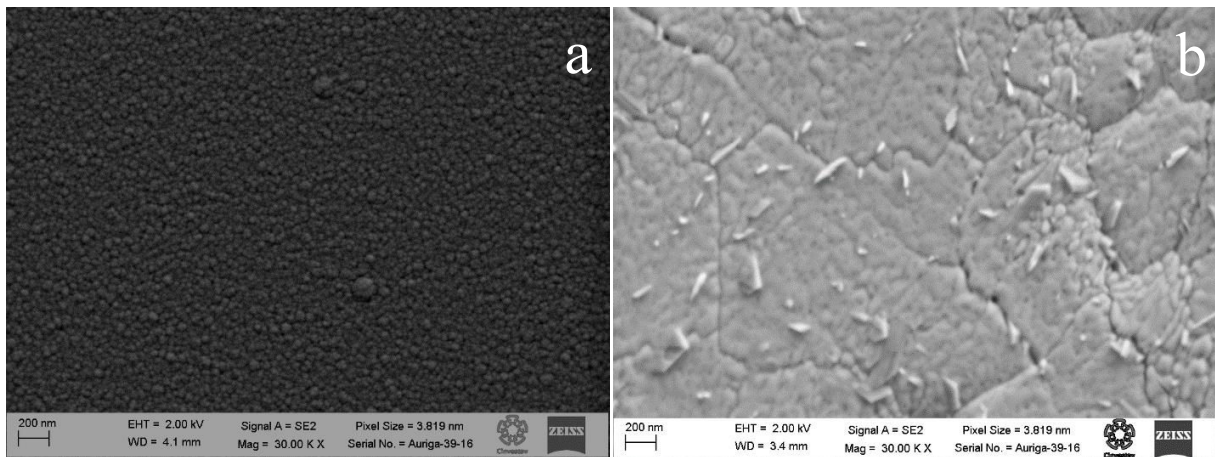


Fig.4.9. FE-SEM micrograph of post annealed (400°C) BiVO_4 films grown on Si (100): (a) deposited at RT, (b) deposited at 450°C .

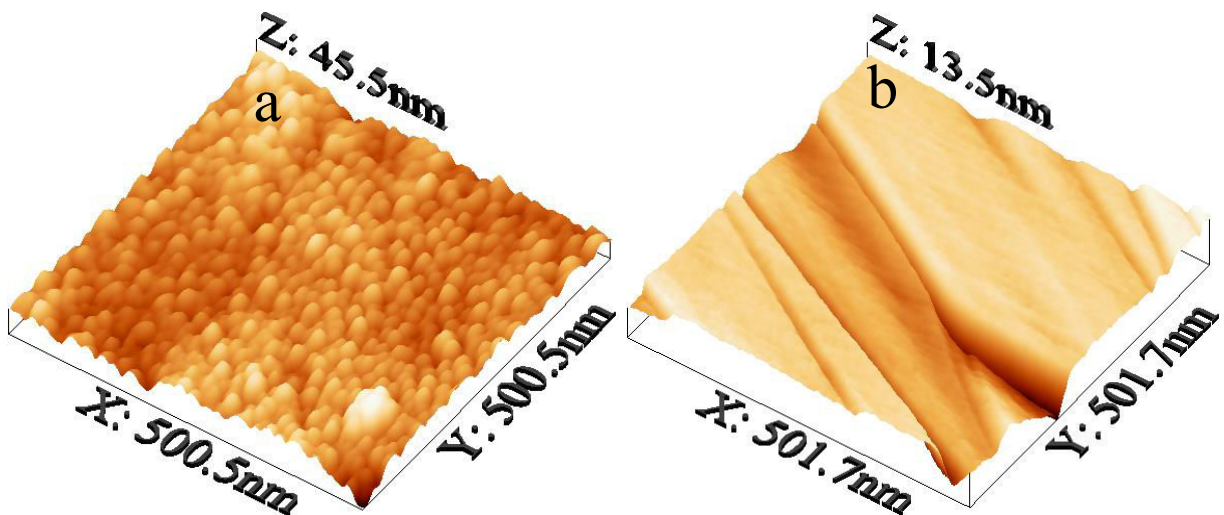


Fig.4.10. AFM images of BiVO_4 films deposited on Si and annealed at 400°C : (a) deposited at RT and (b) deposited at 450°C .

This agglomeration is driven by the surface and elastic energy minimization. BiVO₄ film deposited at 450 °C substrate temperature (Fig.4.10 (b)) is found to have smooth surface morphology along with a relatively less value of root-mean-square (rms) roughness i.e. 2.5 nm. The rms value estimated from Fig.4.9 (a) is found to be approximately 4.66 nm. Fig.4.10 (a) manifests that the space between crystallites is relatively large as compared with Fig.4.10 (b) where the crystallite arrangement is disordered with many equally distributed pores. Morphology of annealed film in the present study depends on the agglomeration of BiVO₄ nanocrystallites. Since the agglomeration took place after the formation of nanocrystallites, an analysis of the temporal and spatial development of nanocrystals was necessary to understand the film formation [23, 24]. As the roughness of the film increases with increasing substrate temperature (as evidenced by the roughness analysis), the above conclusion is relevant for understanding the agglomeration behavior. Heterogeneous catalysis is a surface boundary phenomenon that involves adsorption of light and pollutant on the surface of the catalyst, thus high specific surface area is a key parameter for better photocatalytic efficiency. In this regard, the agglomerates formed by the interconnection of nanocrystalline BiVO₄ particles on the surface of films may cause better absorption of light for the effective degradation of organic pollutants. The roughness factor of a BiVO₄ film is important in the field of heterogeneous catalysis. Similar surface roughening induced by longer deposition time and/or increased substrate temperature were usually observed in the case of TiO₂ [25] and SiO₂ [26] sputtered oxide layers. The observed change in the grain size, distribution and roughness of BiVO₄ film depending on the substrate temperature, can be used as a controlling parameter for changing the structural characteristics of the sputtered BiVO₄ layer.

4.2.2. Effect of oxygen flow rate

4.2.2a. XRD analysis

Fig.4.11 shows the XRD patterns of BiVO₄ films deposited at various oxygen percentages. In general, the film deposited at 2% oxygen flow rate was strongly oriented with their b-axis perpendicular to the substrate with mainly (1 1 0) diffraction peak at a Bragg angle of $2\theta = 18.67^\circ$. Also (0 4 0) reflection plane was little more prominent compared to film deposited with 10% oxygen flow rate and would indicate a change in the morphology. In this case ($O_2 = 2\%$), it can be observed that, there is a strong orientation with c-axis perpendicular to

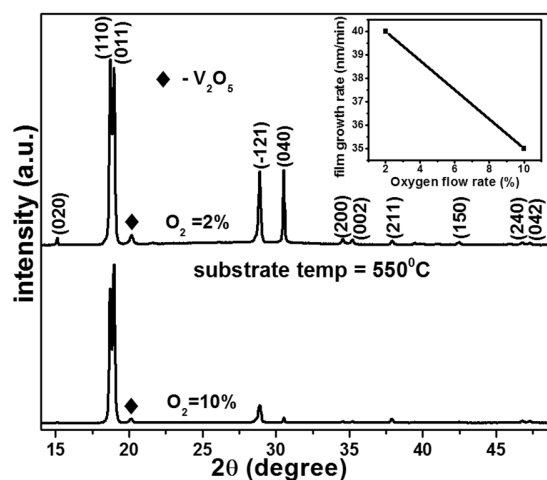


Fig.4.11. XRD patterns of BiVO_4 films sputtered at various Ar/O_2 mixed ambient (inset: thickness variation with oxygen pressure)

the substrate. This can be confirmed through the splitting orientation changes from (1 1 0) diffraction to (0 1 1). This type of preferential growth along a certain crystallographic direction is related to the surface energy. During the growth of thin film, grains with lower surface energy will become larger as the film grows [27]. Then the growth orientation will take place in the crystallographic direction of lowest energy. This can be explained as follows: the deposition rate decreases when oxygen percentage increases, and this will give enough time for BiVO_4 to grow more in preferred direction. The crystallite size of the prepared films was calculated from the XRD results by using Scherrer formula (equation 2.2, Chapter 2). Crystallite size decreased from 48 to 41nm between 2 to 10% oxygen flow rates, which is also related to changes in the deposition rate. A significant variation in the film thickness was observed, as shown in Fig.4.11 (inset), which is also caused by the change of oxygen percentage.

4.2.2b. Surface morphological analysis by FE-SEM

Typical 2-dimensional SEM image of the films are shown in Fig.4.12. The film deposited at 10% oxygen flow rate show beads in a row along with fine grain morphology while a bilayered structured was observed with film grown at 2% oxygen. The top layer has a large grain size (> 500 nm) with many voids between the grains. The bottom layer consists of significantly smaller grain size (< 100 nm), and the layer is compact. Such kind of morphology was observed by Liang *et al* [28] for BiVO_4 on FTO substrate deposited using spray pyrolysis technique and exhibited better properties of photoanode for photoelectrochemical water splitting. SEM micrograph also reveals that all films were uniform and crack free on the surface. In general,

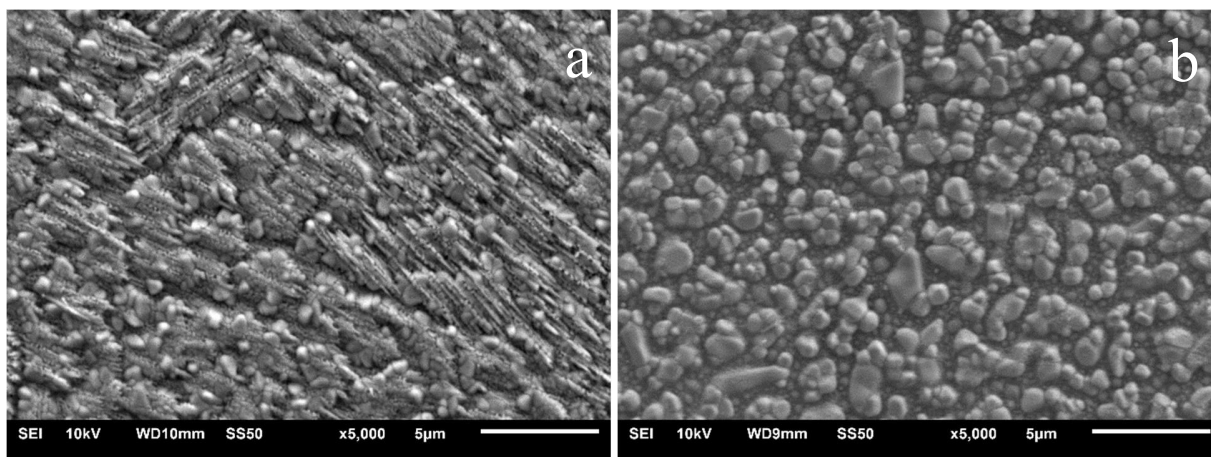


Fig.4.12 SEM images of BiVO_4 films on BK7. a) $\text{O}_2=10\%$ and b) $\text{O}_2=2\%$ deposited at 550°C .

crack in a film is mostly caused by differences in substrate, composition, thickness, and thermal annealing conditions. However, in this study it is proved that high-quality crack-free BiVO_4 thin films with precise stoichiometric ratio having a thickness of about 500 nm can be obtained.

4.2.3. Effect of substrate temperature under $\text{Ar}+\text{O}_2$ atmosphere

4.2.3a. XRD analysis

Fig.4.13 shows XRD patterns of deposited thin films prepared at 10% oxygen flow rate with different T_{sub} (350° , 450° , 550° and 600°C). It is interesting to note that these films exhibit quite good crystalline features without annealing. The characteristic peaks appearing in each of the four XRD patterns can be indexed for monoclinic BiVO_4 (JCPDS no. 14-0688) [5].

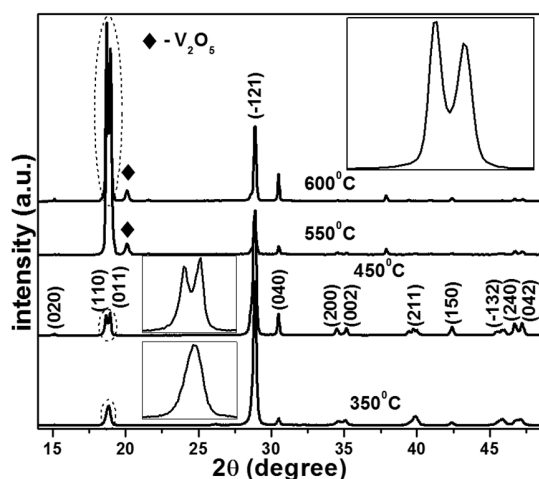


Fig.4.13. XRD patterns of BiVO_4 thin films deposited at different substrate temperatures (inset: magnification of peak at 18.8°).

Films deposited with lower substrate temperatures (350° and 450 °C) showed higher intense monoclinic bismuth vanadate peaks at 28.8°. With an increase in substrate temperature to 550° and 600 °C, films showed strong peaks for monoclinic BiVO₄ at 18.8°, indicating the preferential orientation. The two tiny peaks at 2θ values of 20.1° and 21.5° (film deposited at 550° and 600 °C) match with two of the highest intensity peaks of V₂O₅ (JCPDS 01-089-0611) [29]. However, XRD patterns for these samples were almost identical, and the highest BiVO₄ peak was 16 times more intense than the highest V₂O₅ peak. This suggests that excess of vanadium is incorporated into the interstitial sites of films. Under these conditions, vanadium readily reacts with oxygen during the deposition process. Crystalline nature of BiVO₄ can be readily seen by observing the splitting peaks at 18.8°, 35° and 46°. It is clear that the crystalline nature of the films increases with increasing substrate temperature (inset in Fig.4.13).

As the temperature increased above 450 °C, the intensity of (-1 2 1) peak decreased and the (0 1 1) peak becomes more intense. In addition, an intense peak of (0 1 1) was observed at temperatures above 450 °C, this means that the substrate temperature plays a major role in deciding preferential orientation (Fig. 4.13 (inset)). Similar behavior was observed for ZnO thin films, in which it was explained that the crystal planes perpendicular and parallel to the substrate are mixed together as the substrate temperature is raised [30]. This behavior may also be attributed to complex thermodynamic nature of the deposition process, which is a combination of amorphous nature of the substrate and the continuous bombardment of energetic sputtered species on a heated surface that usually enhances the mobility of species and their diffusivity, resulting in formation of polycrystalline films as observed from the appearance of other XRD peaks [30]. Indeed, it was reported that the deposition of ZnO on a heated amorphous substrate with substantial oxygen partial pressure, leads to the enhancement of several crystal planes, and thus resulting in the mixing of these planes [31].

4.2.3b. Surface morphological analysis by FE-SEM and AFM

Fig.4.14 shows SEM and AFM images of the sputtered BiVO₄ films at different T_{sub}. From these SEM images, it can be seen that grain size, morphology and its distribution are largely affected by the substrate temperatures as expected from the XRD data. The structural characterization (XRD, Fig.4.13) confirmed increased splitting, sharpening and preferential orientation with increasing substrate temperature. Morphology of films deposited at 350 °C, is

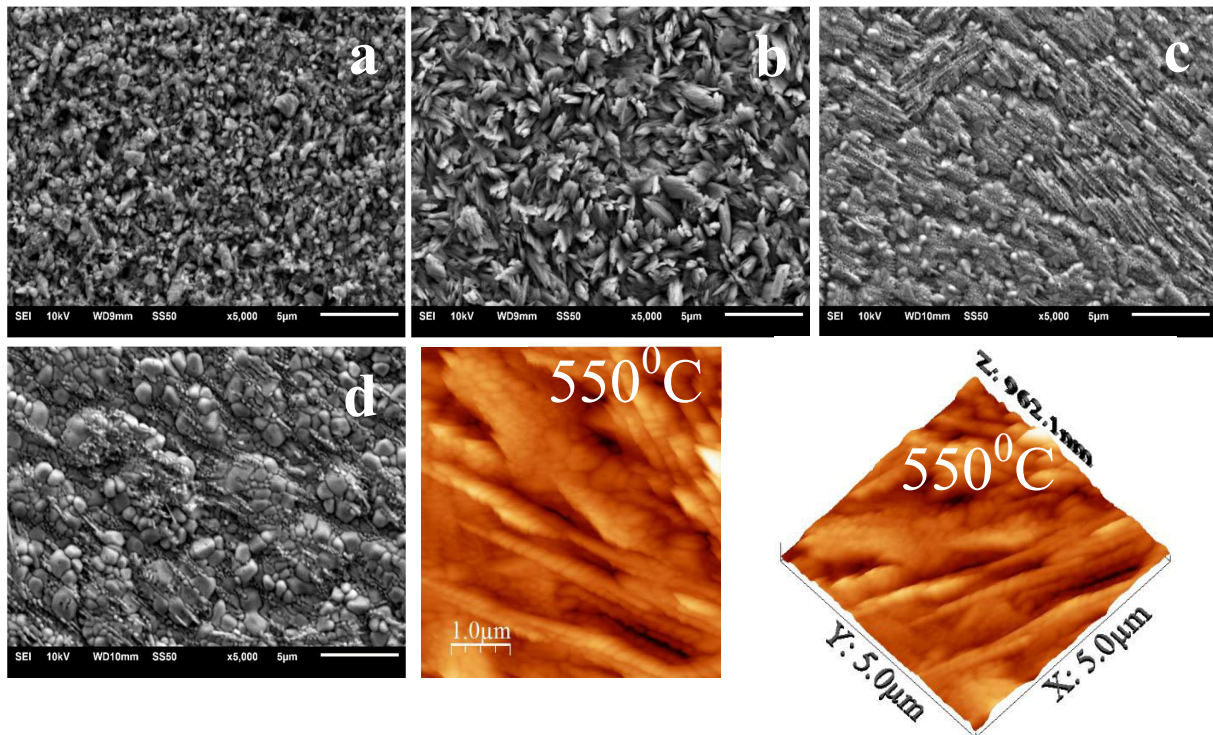


Fig.4.14. SEM micrographs of BiVO₄ thin films deposited at different substrate temperatures. a) 350°C, b) 450°C, c) 550°C, d) 600°C and 2D and 3D AFM images of film deposited at 550°C.

found to have continuous irregular grains of different sizes 10 nm to 1 micrometer. The surface of the film deposited at 450 °C was uniformly distributed as flakes or leaf-like morphology with an almost uniform distribution. The size and shape of an individual leaf is found to be quite uniform. The film grown with 550 °C, shows the beads in a row along with fine grain morphology. At 600 °C, it appeared that small grains coalesce together to form larger grains. This process of coalescence causes major grain growth and surface roughness. We also presume that the evolution of microstructure would be related to migration of surface atoms during the deposition. The sputtered atoms form nucleation centers and due to thermal energy migrate and coalesce to form denser film with larger grains and lower defects. This transformation in the structure can be explained by various steps as coalescence, nucleation, aggregation, and subsequent growth by stacking the particles. This rf-sputtered thin film has shown a unique morphology (acicular and grains) which may possess large surface area therefore, it is quite suitable for utilizing maximum solar radiation in energy conversion devices and photodegradation of organic pollutants. AFM images provide 3D image of BiVO₄ films in terms of depth, height, and grain size. The 2D and 3D images of BiVO₄ film with (5 x 5 μm) surface

area scanned by AFM is displayed in Fig.4.14. 3D micrograph of film deposited at a substrate temperature 550°C revealed and evidenced the acicular morphology as seen in the SEM micrograph (fig.4.14 (c)). The grains have grown along the direction of substrate, this result is in well agreement with XRD pattern. Overall, the surface was homogenous and grains have diverse shapes, heights and sizes. In addition all the films showed crack free and porous free morphology. These observations confirm that the increase in the adatom mobility of the sputtered atoms contribute to void-free and crack free surface morphology [32]. In SEM and AFM images, the beads in a row morphology are seen on a primary layer (Fig.4.14). It is a result of a competition during deposition between the rate of arrival of new BiVO₄ species on to the surface and concurrent redistribution over the surface by diffusion.

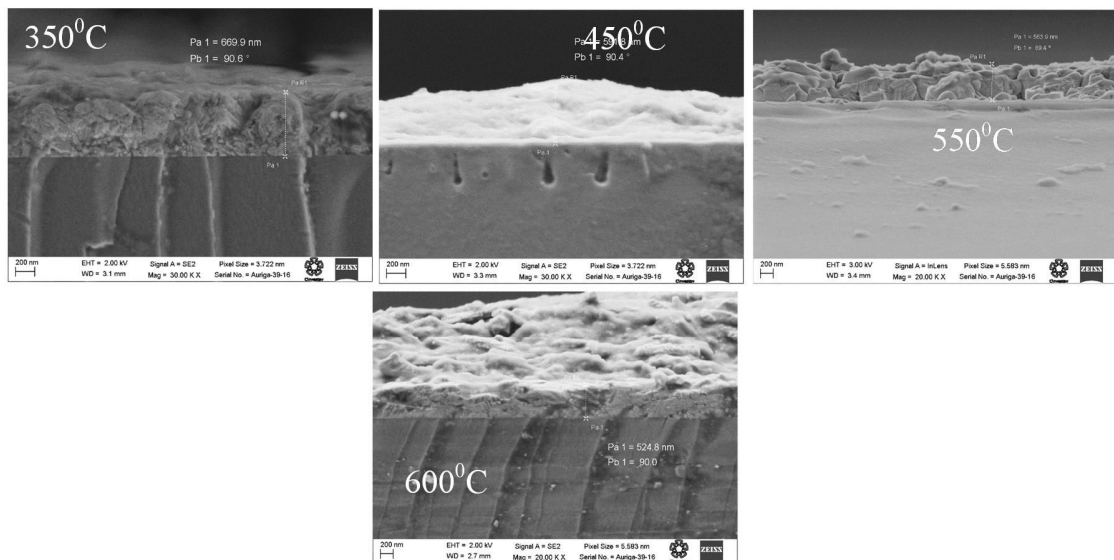


Fig.4.15. FE – SEM cross sectional micrographs of BiVO₄ thin films deposited at different substrate temperatures.

Thickness of the various substrate temperature deposited BiVO₄ films were characterized by cross section of BiVO₄ (Fig.4.15) films and profilometry techniques and are presented in table 4.4. Linear decrease in film thickness was observed with increasing T_{sub} (Fig.4.16), which is consistent with the changes in surface color. Dark yellow color (not shown here) corresponds to 671 nm film thickness deposited at 350°C while pale yellow color corresponds to 480 nm thickness deposited at 600°C.

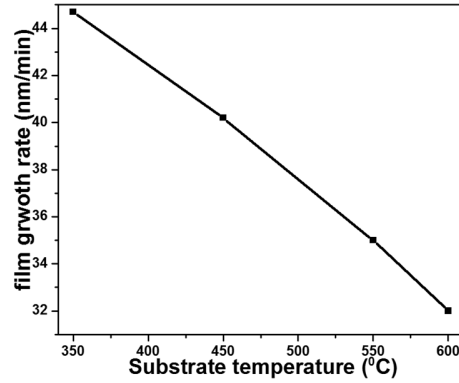


Fig.4.16. Film growth rate at different substrate temperatures.

Table 4.4. Calculated thickness of rf-sputtered BiVO₄ films.

Substrate temperature (°C)	Thickness (nm)		
	FE-SEM	Profiolometry	Average
350	671	635	653
450	603	600	601
550	525	537	531
600	480	430	455

4.2.4. Optical characteristics

The optical absorption spectra of BiVO₄ thin films deposited in Ar atmosphere are shown in Fig.4.17, along with the band gap evaluation seen in the inset. BiVO₄ films deposited at various substrate temperatures under Ar atmosphere showed intense absorption in the visible-light region (from 400 to 500 nm) in addition to that in the UV region. Castillo *et al* [33] attributed the steepness of BiVO₄ absorption profiles to the degree of crystallinity as a complement to diffraction profiles. Indeed band broadening can be caused by a number of

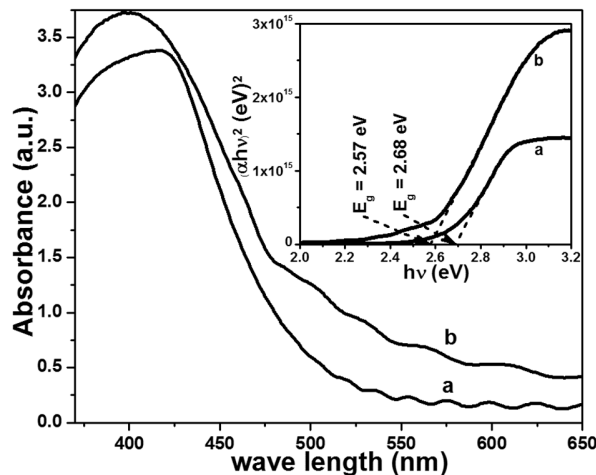


Fig.4.17. UV - Visible absorption spectrum of a BiVO₄ thin film obtained by rf-sputtering on glass substrate under Ar. a) deposited at RT and b) deposited at 450 °C (inset: $(\alpha h\nu)^2$ vs photon energy plot).

factors beyond crystallinity. The steep shape of the spectrum indicated that the visible-light absorption is due to inter band transition. Considering direct band gap transition [33], the optical band gap E_g was estimated.

The band edge for the films (a) and (b) are found to be 492 and 518 nm respectively. The absorption wavelength of BiVO_4 thin film is decreased as compared to bulk. In other words, the absorption edge of BiVO_4 thin films blue shifted towards higher energy side [34, 35]. Thus, the estimated band gap for samples (a) and (b) were found to be 2.67 and 2.59 eV respectively. The higher value of optical band gap obtained for the film may be attributed to quantum confinement effect by the formation of small sized nanocrystals.

The optical absorption spectra of sputter deposited BiVO_4 films with different oxygen flow rate are shown in Fig.4.18. As compared to 2% oxygen flow rate, there was strong photoabsorption in the visible region for the film grown under 10% oxygen flow rate. So, increasing oxygen flow rate causes a red shift in absorption edge. It was clear that increment of O_2 flow rate led to a reduction in the band gap energy. Band gap energy (E_g) helps in evaluating the optical absorption performance of photocatalysts; lower the E_g value, higher is the photocatalytic performance [36, 38]. The decrease in band gap energy indicates that film deposited at 10% oxygen flow rate has a broader optical absorption property as compared to film deposited at 2% oxygen flow rate. So, 10% deposited BiVO_4 film, can be expected to produce more electron-hole pairs under the same visible-light irradiation and will result in higher photocatalytic activity.

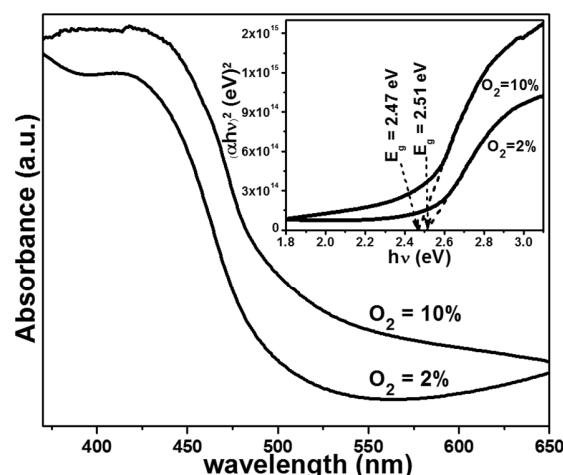


Fig.4.18. UV - Visible absorption spectrum of a BiVO_4 thin film obtained by rf-sputtering with different oxygen pressure percentage (inset: $(\alpha h\nu)^2$ vs photon energy plot).

UV-Vis measurements were performed to determine differences in optical properties of the films prepared with different T_{sub} under Ar+O₂ atmosphere. Fig.4.19 shows UV-Vis absorbance spectrum for BiVO₄ films synthesized with different T_{sub} . The spectrum of the film

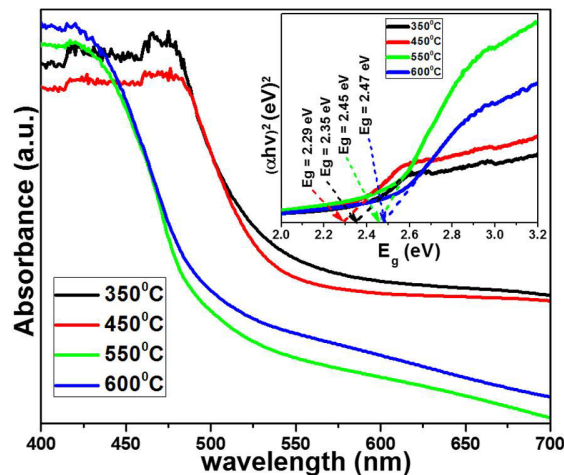


Fig.4.19. UV - Visible absorption spectrum of a BiVO₄ thin film obtained by rf-sputtering on BK7 substrate under Ar+O₂ atmosphere (inset: $(\alpha h\nu)^2$ vs photon energy plot).

showed sharp absorption edges. Plot of absorption coefficient as a function of photon energy ($h\nu$) were used to calculate the band gap of the deposited films as shown in Fig.4.18 (inset). The determined band gap energies of film deposited at 350°, 450°, 550° and 600 °C are found to be 2.35, 2.29, 2.47 and 2.45 eV respectively which is inconsistent with the literature report [39, 40]. These results clearly demonstrate that the substrate temperature has a great impact on the electronic structures of BiVO₄.

4.3. Conclusion

The new BiVO₄ thin film preparation approach combining the versatility of mechanochemical with ultrasonic spray pyrolysis and rf-sputtering should nicely complement the replication techniques that already exist. Significant effort has been devoted to optimize the experimental parameters of these two techniques. The experimental results indicate that (i) XRD measurements of thin films exhibit a greater quality of crystalline order with monoclinic scheelite structure. (ii) HT-XRD measurement give additional pathway forward for the preparation of crystalline BiVO₄ thin films. (iii) The morphology of BiVO₄ thin films was significantly varied from fine grains to nanocrystalline-like, leaf-like, beads in row-like and double layers consisting of 10 nm particles using rf-sputtering as compared with USP technique.

This modified nanostructures could allow efficient charge generation, separation, transportation and utilization to enable a new generation of highly efficient photocatalysts. (iv) The band gap of the deposited films can be engineered from 2.09 eV to 2.67 eV to satisfy for the high absorption of solar energy. Summarizing these findings, substrate temperature has served as the most influential parameter in controlling the particle size, morphology, preferential orientation and absorption edge of the thin films. This work is anticipated to open new possibilities in reducing the energy cost and promoting to obtain the metal oxide structures from cheap precursors, potentially useful in advanced applications such as photocatalysis or photovoltaics.

References

1. M. N. Fox, M. T. Dulay, *Chem. Rev.* 1993, 93, 341-357.
2. H. K. Timmaji, W. Chanmanee, N. R. de Tacconi, K. J. Rajeshwar, *J. Adv. Oxid. Technol.* 2011, 14, 93-105.
3. M. A. Lazar, S. Varghese, S. S. Nair, *Catalysts*, 2012, 2, 572-601.
4. M. Li, L. Zhao, L. Guo, *International J. hydrogen energy*, 2010, 35, 7127-7133.
5. S. M. Thalluri, M. Hussain, G. Saracco, J. barber, N. Russo, *Ind. Eng. Chem. Res*, 2014, 53, 2640-2646.
6. S. Dong, C. Yu, Y. Li, J. Sun, X. Geng, *J. Solid state chemistry*, 2014, 211, 176-183.
7. E. Zaleta-Alejandre, R. Balderas-Xicotencatl, M.L. Perez Arrieta, A.N. Meza-Rocha, Z. Rivera-Alvarez, C. Falcony, *Materials Science and Engineering B*, 2013, 178, 1147-1151.
8. H. C. Kim, T.L. Alford, D.R. Allee, *Applied Physics Letters*, 2002, 81, 4287-4289.
9. L. Lin, Y. Chai, Y. Yang, X. Wang, D. He, Q. Tang, S. Ghoshroy, *Inter J. Hydrogen energy*, 2013, 38, 2634-2640.
10. G. Yang, Z. Jiang, H. Shi, T. Xiao, Z. Yan, *J. Mater. Chem*, 2010, 20, 5301-5309.
11. A. Kudo, K. Omori, H. Kato, *J. Am. Chem. Soc*, 1999, 121, 11459-11467.
12. A. Zhang, J. Zhang, N. Cui, X. Tie, Y. An, L. Li, *Journal of Molecular Catalysis A, Chemical*, 2009, 304, 28-32.
13. X. Lin, H. Li, L. Yu, H. Zhao, Y. Yan, C. Liu, H. Zhai, *Material research bulletin*, 2013, 48, 4424-4429.
14. M. Vishwas, K. Narasimha Rao, R. P. S. Chakradhar, *Spectrochimica Acta Part A: Molecular and Biomolecular spectroscopy*, 2012, 99, 33-36.
15. E. Burstein, *Phys. Rev*, 1954, 93, 632-633.
16. S.C. Jain, D.J.Roulston, *Solid State Electron*, 1991, 34, 453-465.
17. T. Prasada Rao, M.C. Santhosh Kumar, S. A. Angayarkanni, M. Ashok, *J. Alloys Compd*, 2009, 485, 413-417.

18. D. R. Milev, P. A. Atanasov, A.Og. Dikovska, I. G. Dimitrov, K. P. Petrov, G. V. Avdeev, *Applied surface science*, 2007, 253, 8250-8253.
19. Y. E. Jeong, S. Park, *Current applied physics*, 2014, 14, 30-33.
20. H. Sun, W. Ma, J. Yu, X. Chen, W. Sen, Y. Zhou, *Vacuum*, 2012, 86, 1203-1209.
21. R. L. Frost, D.A. Henry, M.L. Weier, W. Martens, *J. Raman Spectrosc*, 2006, 37, 722-732.
22. M. R. da Silva, L. H. Dall'Antonia, L. V. A. Scalvi, D. I. dos Santos, L. O. Ruggiero, A. Urbano, *J Solid State Electrochem*, 2012, 16, 3267-3274.
23. G. Lian, Z. Shan, Z. Qing-hong, *Chemical Industry Press*, 2002, 191-232.
24. I. Umezu, A. Sugimura, M. Inada, T. Makino, K. Matsumoto, M. Takata, *Phys. Rev. B*, 2007, 76, 1-10.
25. M. Abdul Khadar, N.A. MoheemmedShanid, *Surface & Coatings Technology*, 2010, 204, 1366-1374.
26. E. Quartarone, P. Mustarelli, S. Grandi, F. Marabelli, E. Bontempi, E, *Journal of Vacuum Science & Technology A: Vacuum, surface and films*, 2007, 25, 485-491.
27. R. Tahar, *J. Eur. Ceram. Soc*, 2005, 25, 3301-3306.
28. Y. Liang, T. Tsubota, L. P. A. Mooij, R. van de Krol, *J. Phys. Chem. C*, 2011, 115, 17594-17598.
29. S. P. Berglund, D. W. Flaherty, N. T. Hahn, A. J. Bard, C. B. Mullins, *J. Phys. Chem. C*, 2011, 115, 3794-3802.
30. K. Wasa, S. Hayakawa, *Handbook of Sputter Deposition Technology, Principles, Technology and Applications*, Noyes Publication, 1992, 124-157.
31. S. J. Kang, Y. H. Joung, *Applied. Surf. Sci.* 2007, 253, 7330-7335.
32. S. B. Amor, M. Jacquet, P. Fioux, M. Nardin, *Materials Chemistry and Physics*, 2010, 119, 158-168.
33. Nikola C. Castillo, A. Heel, T. Graule, C. Pulgarin, *Applied Catalysis B: Environmental*, 2010, 95, 335-347.
34. C. Karunakaran, S. Kalaivani, P. Vinayagamoorthy, S. Dash, *Materials science in semiconducting processing*, 2014, 21,122-131.
35. S. Sarkar, K. K. Chattopadhyay, *Physics E*, 2012, 44, 1742-1746.
36. A. Iwase, A. Kudo, *J. Mater. Chem*, 2010, 20, 7536-7542.
37. W.R. Zhao, Y. Wang, Y. Yang, J. Tang, Y. Yang, *Applied. Catal. B, Environ*, 2012, 115, 90-99.
38. M. Yao, M. Liu, L. Gan, F. Zhao, X. Fan, D. Zhu, Z. Xu, Z. Hao, L. Chen, *Colloids Surf., A, Physicochem. Eng. Aspects*, 2013, 433, 132-138.
39. H. Liu, R. Nakamura, Y. Nakato, *J. Electrochem. Soc*, 2005, 152, G856.
40. A. P. Zhang, J. Z. Zhang, *J. Alloys and Compounds*, 2010, 491, 631-635.

5. Photocatalytic investigations

Photocatalytic reactions are classified into homogeneous and heterogeneous depending on the nature of reactants and the class of photocatalysts. In this frame, heterogeneous photocatalysts such as TiO_2 , ZnO , WO_3 and BiVO_4 were widely investigated during the last decade with an objective to achieve simple and complete photodecomposition of organic pollutants into less harmful compounds [1]. The main goal of the present work is to evaluate photocatalytic efficiency of BiVO_4 powders and thin films obtained by different techniques presented in the previous chapters. In this context, degradation of methylene blue (MB) and rhodamine 6G (Rh6) in water were carried out and reported. These potential photocatalysts can then be used to degrade more toxic pollutants stemming from various industries and agricultural activities which can have an adverse effect on Ecology [2, 3].

By using suitable irradiation source and spectrophotometer for the measurements of absorbance, an operational setup was designed to carry out the photocatalytic reactions between BiVO_4 and dye molecules. Photodegradation kinetics of Rh6 dye was studied for BiVO_4 micro and nanostructures prepared using hydrothermal, mechanochemical and rf-sputtering methods. MB photodegradation performance was studied for the ball milled BiVO_4 nanopowders and USP deposited thin films. The degradation time was compared and deliberated on crystalline nature, surface states and micro and nano structures of BiVO_4 powders and thin films.

5.1. Concept of photodegradation process

Photocatalytic process occurs when semiconducting materials are subjected to light irradiation causing accelerated chemical reactions. Such processes give rise to free radical species which can react with organic components leading to their mineralization and then their degradation. As it can be observed from Fig.5.1, a photocatalyst such as BiVO_4 in contact with organic pollutants under visible light illumination, absorbs such radiation, which corresponds to its optical band gap. As a result, electrons are promoted from its valence band to the conduction band, then photo-induced charge carriers were created and separated (Eq. (5.1)).

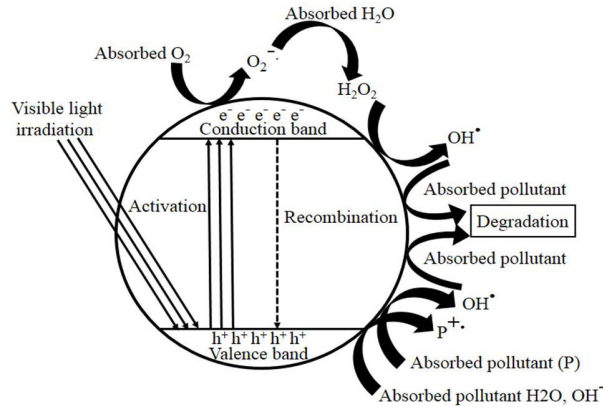
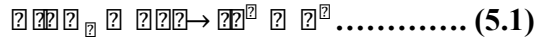
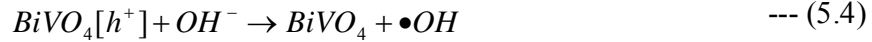
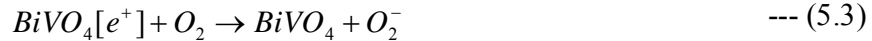


Fig.5.1. General Mechanism of photocatalysis.



The charged species diffuse rapidly towards the catalyst surface where they undergo reduction-oxidation reactions. Excited photoelectrons react with adsorbed oxygen molecules O_2 to form electronically active superoxide anion radicals (O_2^-). On the other hand, photo-induced holes in the valence band oxidize H_2O leading to the formation of hydroxyl radical species ($\bullet OH$). The valence band (h^+) potential is positive enough to generate hydroxyl radicals ($\bullet OH$) from water adsorbed at the surface on $BiVO_4$ and the conduction band (e^-) potential is negative enough to reduce adsorbed molecular oxygen leading to peroxide radicals [4] as shown in the

following equations:



Hydroxyl radical is a powerful oxidizing agent which attacks the organic matter (R) present at or near the surface of $BiVO_4$. It is capable to degrade toxic and bio resistant compounds into harmless species. The products of the photodegradation are reduced to purely mineralized compounds and then CO_2 is released. An example is illustrated below in Fig.5.2, which shows degradation pattern of pesticide as methyl parathion (MP) using TiO_2 photocatalyst.

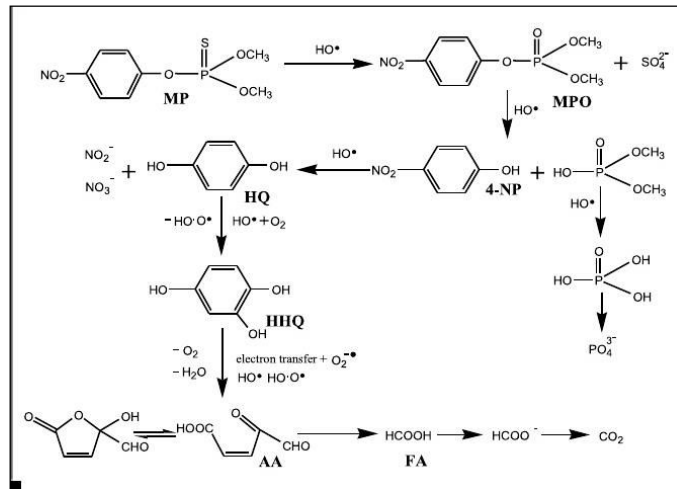


Fig.5.2 Degradation of methyl parathion using TiO_2

5.2. Photodegradation study of BiVO_4 powders

Dye degradation in aqueous solutions is employed as a measure of the photocatalytic activity of BiVO_4 nanostructures. In this work, the degradation of MB and Rh6 are considered and the efficiency of the process is analyzed based on the structure, morphology, and specific surface area of BiVO_4 . Rh6 is photostable in the absence of catalyst unlike methylene blue which shows appreciable degradation in light even without any catalyst.

5.2.1. Photodegradation effects on hydrothermally synthesized acicular BiVO_4

To demonstrate the photocatalytic activity of acicular monoclinic BiVO_4 , Rh6 dye molecules are chosen as a probes for the photocatalytic process. Fig.5.3 shows UV-Vis spectra

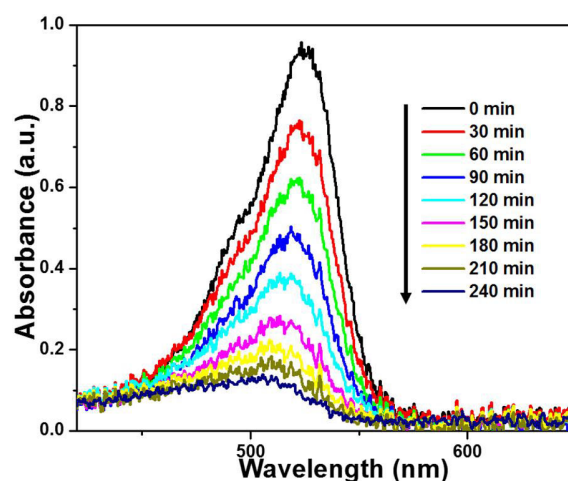


Fig.5.3. Changes in UV-Vis spectra of BiVO_4 particles dispersed in Rh6 solution as a function of irradiation time.

taken over time during the photodegradation of Rh6 mediated by BiVO₄ acicular particles. From Fig.5.4, it can be concluded that the photodegradation rate of Rh6 is up to 86% in a span of 240 min under visible light irradiation, which is much higher than that of the results shown Obregon *et al* [5].

In addition to decreased absorption of Rh6/BiVO₄ suspension during photodegradation, there is distinct blue-shift of the absorption band spectrum. The main reason for this blue-shift is due to the removal of ethyl groups one by one, which is in good agreement with the literature reports [6, 7]. Indeed, during 240 min of illumination, there is a blue-shift from 526 nm to 507 nm in the presence of BiVO₄, indicating that Rh6 has released methyl groups [8]. The normalized concentration of the dye solution (C/C_0) is proportional to the normalized maximum absorbance (A/A_0) [9]. Therefore, the temporal concentration changes of Rh6 during the photodegradation can be derived from the changes in the dye's absorption profile (\cong 527 nm) at a given time interval. The change in the concentration (C) of Rh6 in solution was monitored through its $\ln(C/C_0)$ vs irradiation time curve [10]. Fig. 5.4 shows the photodegradation efficiency of Rh6 as a function of the irradiation time. The decrease of Rh6 concentration in the presence of pure BiVO₄ is 86% after 240 min or irradiation.

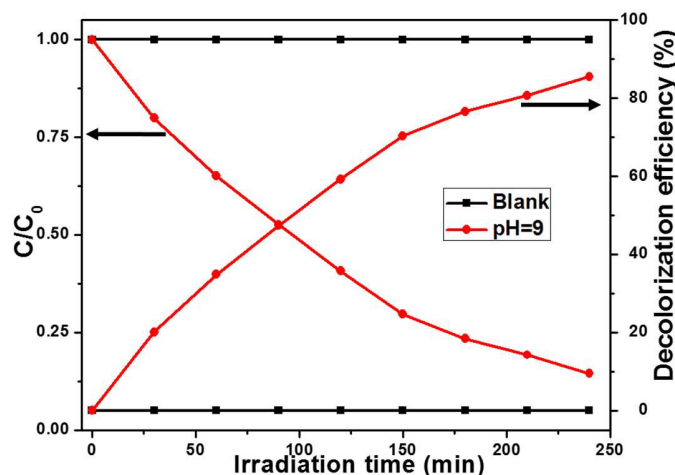


Fig.5.4. Photodecomposition of Rh6 dye and decolorization efficiency of BiVO₄ C and C₀ refers to the concentration of the dye Rh6 at time (t) and at initial time respectively.

The results indicate that the photodegradation of dyes proceeds through a pseudo first-order kinetic reaction [11]. The evaluated reaction rate (k) for BiVO₄ with acicular morphology is 0.008 min⁻¹. The larger the constant, lower the reaction rate will be. No attempt was made to

investigate the degradation mechanism of this organic compound using as-prepared BiVO_4 photocatalyst because similar information is available in the literatures [12, 13].

5.2.2. Photodegradation study of ball milled BiVO_4

Rh6 and MB (with a major absorption band at 527 and 664 nm, respectively) were chosen as the model pollutants for testing the photocatalytic activity of the ball milled samples (6hA10:1, 11hA10:1 and 16hA5:1) under visible light irradiation. The photocatalytic reactions of the prepared samples were performed under three different conditions: (i) Degradation of Rh6 and MB monitored under visible light for 180 mins without photocatalyst, and the decomposition percentage was found to be 0% for Rh6 but MB showed 3%. (ii) The experiments were also performed under dark for 60 mins in the presence of photocatalysts, which indicated the adsorption of dyes on the active sites of the photocatalyst. (iii) Finally, degradation of Rh6 and MB was monitored in the presence of photocatalysts under visible-light irradiation. The results suggest that degradation of both the dyes were effectively achieved by visible-light illumination.

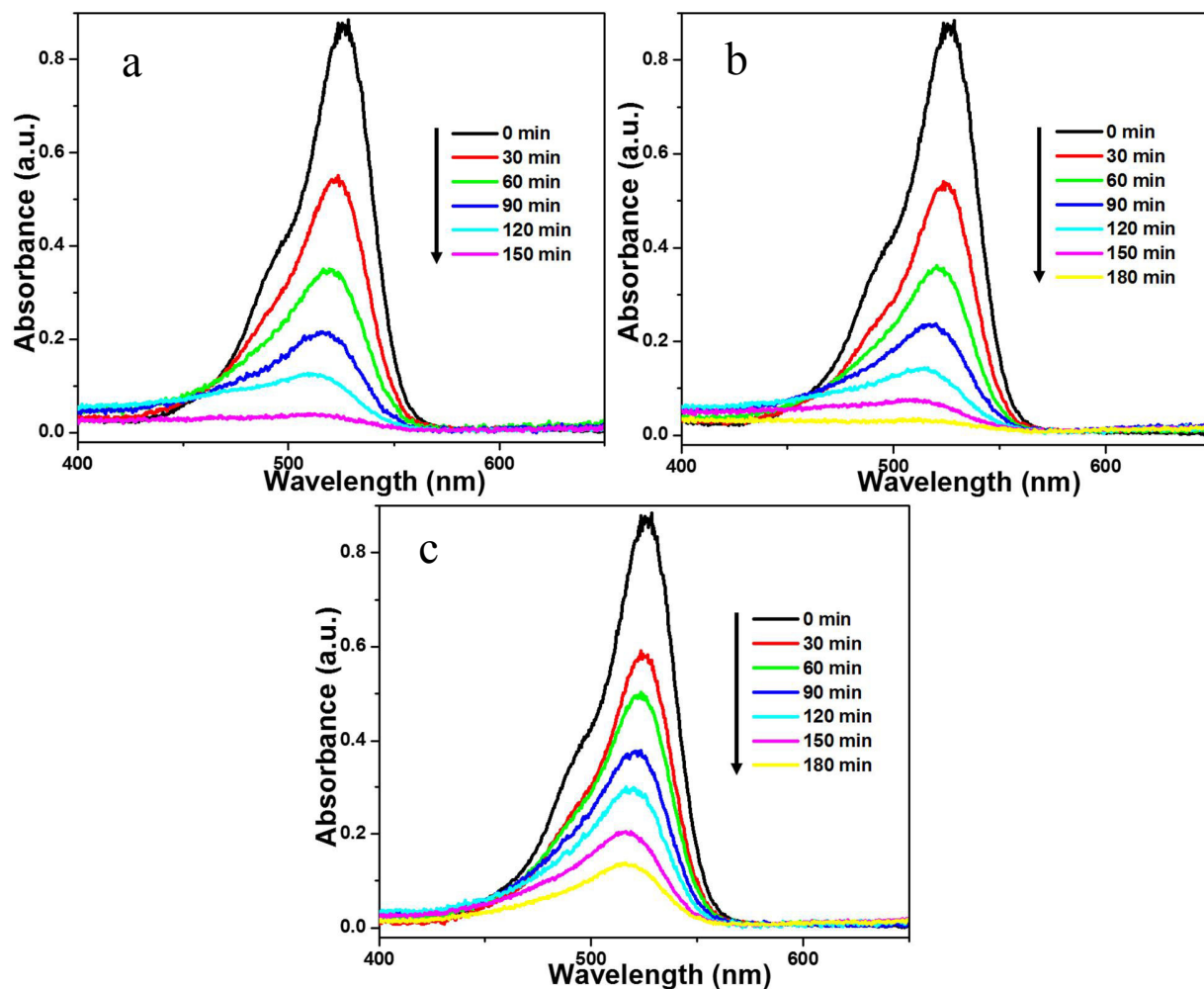


Fig.5.5. Absorption change of Rh6 solution undergoing a photocatalytic process with ball milled BiVO_4 photocatalyst. (a) 6hA10:1, (b) 11hA10:1 and (c) 16hA5:1.

The evolution of spectral changes during the photodegradation process of Rh6 by 6hA10:1, 11hA10:1 and 16hA5:1 is displayed in Fig.5.5. The spectra showed that the intensity of absorption peak decreases as the illumination time increases, thus indicating Rh6 was gradually mineralized as expected in photocatalytic process.

Table 5.1. Peak shift position of ball milled samples versus irradiation time.

Irradiation time (min)	Samples with peak shift (nm)		
	6hA10:1	11hA10:1	16hA5:1
0	527.1	527.1	527.1
30	522.5	523.9	524.4
60	519.1	520.2	522.8
90	516.6	517.6	520.7
120	511.6	514.4	518.6
150		511.8	516.5

As discussed in section 5.1, when BiVO_4 is irradiated with visible spectrum it induces a decomposition of the dyes. In this process, the hydroxyl radical is an extremely strong, non-selective oxidant which makes complete mineralization of dyes, like CO_2 and H_2O [14, 15] which remain in the decolorized solution. In case of Rh6, the photodegradation can occur by two mechanisms:

- i) $\cdot\text{OH}$ radicals effects on the aromatic chromophore rings, leading to a degradation of Rh6 structure and reduction of the absorption band without a wavelength shift;

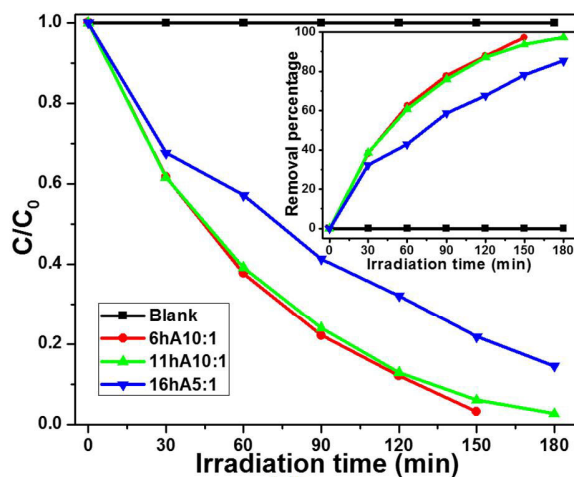


Fig.5.6. Photodegradation of Rh6 in aqueous dispersions under visible light irradiation for different BiVO_4 ball milled samples (inset Rh6 removal percentage vs time of ball milled samples).

- ii) by a successive de-ethylation from the aromatic rings, causing significant blue shift according to the formation of different de-ethylated Rh6 intermediates [13, 14].

According to the spectral evolution (Fig.5.5), a depletion of absorbance occurs with a blue shift of the absorption maxima as shown in table 5.1. Rh6 photodegradation can be attributed to color change of aqueous solution and decrement in the intensity of absorbance.

The percentage of Rh6 degradation as a function of illumination time is shown in Fig.5.6. It was found that degradation rates of Rh6 for 16hA5:1 sample is much lower (85.4%) under visible light irradiation because of its band gap limitation and increased agglomeration of the particles. The magnitude of Rh6 degradation was much larger for sample 11hA10:1 which is 97.3% in 180 min. The relatively poor photodegradation efficiency of other samples might be ascribed to the quick recombination of charge carriers. However, 6hA10:1 exhibited a much higher photocatalytic activity (97.3% in 150 min) as compared to 11hA10:1 and 16hA5:1 samples. The excellent performance could be attributed to the reduced particle size and well dispersed particles which can usually offer more active adsorption sites and photocatalytic reaction centers. This may suppress the recombination of electron/hole pair and enhance the quantum efficiency for effective photodegradation.

UV-Vis spectra of MB solution after 120 min. of irradiation time for sample 6hA10:1 is plotted in Fig.5.7. It is clear that the absorption peak at 664 nm decreases dramatically as visible light irradiation time increases and nearly disappears within 120 min. Furthermore, for the entire

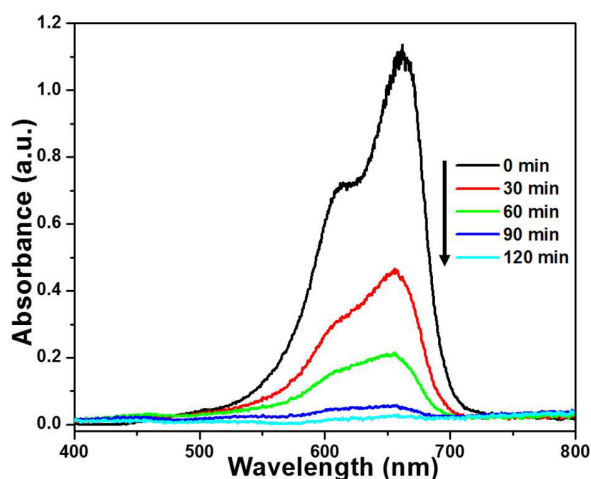


Fig.5.7. Changes of UV - Vis spectra of 6hA10:1 BiVO₄ particles suspended MB solution as a function of irradiation time.

ball milled samples the absorption maxima position of MB did not change significantly, indicating that demethylation was not the main reaction pathway. At the same time, the blue color of MB disappeared gradually, demonstrating that the chromophoric structure ($>C=N-$) of MB was destroyed [16].

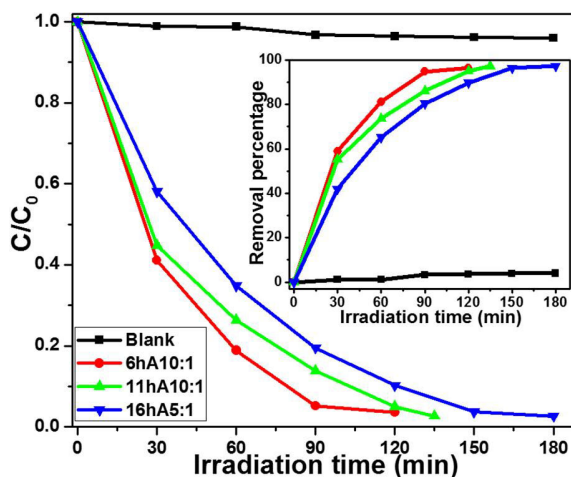


Fig.5.8. Photodegradation of MB in aqueous dispersions under visible light irradiation for different time ball milled BiVO_4 samples (inset MB removal percentage vs time of ball milled samples).

Fig.5.8 shows the relative concentration changes (C/C_0) of MB at 664 nm as a function of visible light irradiation for the samples 6hA10:1, 11hA10:1 and 16hA5:1. Apparently, blank experiments showed negligible changes in MB concentration (3.9%) within 180 min of visible light irradiation. The 6hA10:1 sample showed good photocatalytic activity than 11hA10:1 and 16hA5:1 samples for the degradation of MB. The total photodegradation of MB for the 6hA10:1 sample in the reaction solution was 96.5% under 120 min of visible light irradiation. It is found that the milling time and BPR experimental parameters played a vital role in the enhancement of photodegradation process. The optimized synthesis parameter for maximum photocatalytic efficiency was found to be 6 h milling with 10:1 BPR.

The photodegradation rate constant (k_{app}, min^{-1}) was calculated from the slope of the plot $-\ln(C/C_0)$ versus irradiation time. In all cases, R^2 factor (R means the correlation coefficient that gives the quality of a least square fitting to the original data) was greater than 0.97, which confirm the relevance of Langmuir-Hinshelwood kinetic model ($-\ln(C/C_0) = k_{app}t$) for Rh6 and MB degradation. The reaction rate constants of Rh6 dye for samples 6hA10:1, 11hA10:1 and 16hA5:1 are found to be 0.0215, 0.0198 and 0.0103 min^{-1} respectively (Fig.5.9 (A)). The reaction

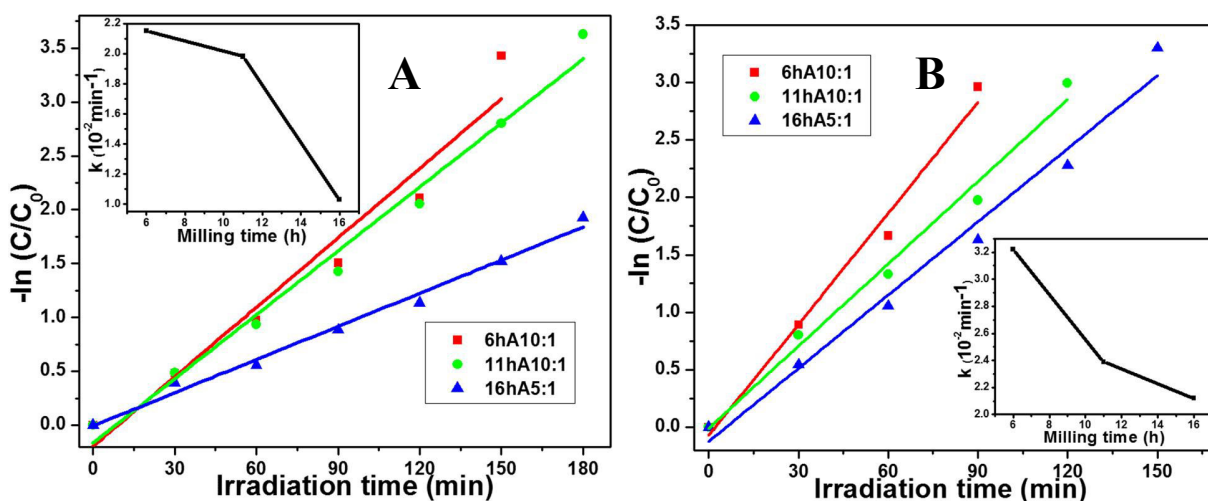


Fig.5.9. Photocatalytic pseudo-first-order kinetics of 6hA10:1, 11hA10:1 and 16hA5:1. (A) Rh6 and (B) MB. (inset: photodegradation rate constant for different ball milled BiVO_4 powders).

rate constants of MB dye for samples 6hA10:1, 11hA10:1 and 16hA5:1 are found to be 0.0322, 0.0238 and 0.0212 min^{-1} respectively (Fig.5.9 (B)). As shown in the Fig.5.9 (A) and (B) (inset), the rate constant of 6hA10:1 is much larger than that of 11hA10:1 and 16hA5:1. Therefore 6hA10:1 possesses superior photocatalytic activity which is consistent with the photocatalytic degradation results presented in Fig.5.6 and 5.8. In comparison, the reaction rate constants for the degradation of Rh6 and MB for sample 6hA10:1 was 0.0215 min^{-1} and 0.0322 min^{-1} , respectively.

It has been reported that the crystal structure, crystallinity, morphology and surface area of the photocatalyst are important factors influencing its photocatalytic performance [17]. As revealed in the XRD investigations, all the as-prepared BiVO_4 powders possessed well-grown monoclinic crystal structures. It means that the crystal structure and crystallinity may not be the main reason for different photocatalytic activities of these BiVO_4 materials. Therefore, the larger surface area and spherical-like morphology would account for excellent photocatalytic activity of monoclinic bismuth vanadate powders.

5.2.3. Photodegradation study of USP deposited BiVO_4 thin films

Photocatalytic activity of BiVO_4 thin films was evaluated by measuring the degradation of MB dye solution. The change in MB concentration was determined by measuring its characteristic absorption band at 664 nm (Fig. 5.10). It can be seen that BiVO_4 film obtained at

425 °C, shows an excellent visible-light driven photocatalytic activity, (66% of MB is degraded in 120 min) than the films deposited at 350°, 450° and 500 °C. Notably, the enhanced visible-light driven photodecomposition property could be ascribed to its narrow band gap (2.09 eV) and

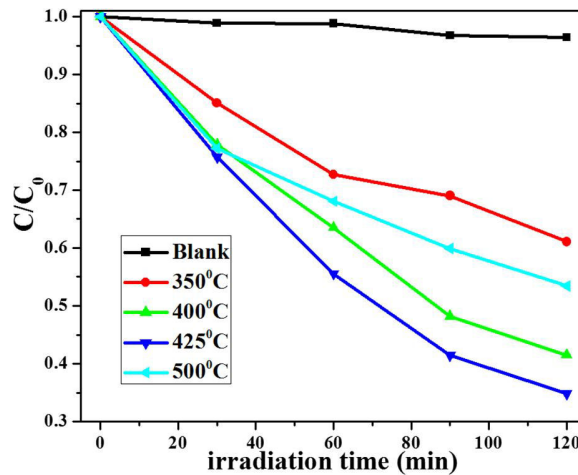


Fig.5.10. Photodegradation of MB in aqueous dispersion under visible light irradiation for BiVO₄ films deposited at different T_{sub} using USP technique.

also to the crystalline order and microstructure of the films.

The density functional theory (DFT) calculation shows that the valence band (VB) of monoclinic scheelite BiVO₄ is composed of hybrid orbitals of Bi6s and O2p, whereas the conduction band (CB) is composed of V3d orbitals. The charge transfer is supposed to take place from Bi6s and O2p hybrid orbitals to V3d orbitals under photoexcitation [18, 19]. Band gap energy (E_g) is a commonly used property to evaluate the optical absorption performance of photocatalysts; lower the E_g value, higher is the photocatalytic performance. The decrease in band gap energy indicates that BiVO₄ thin films have a broader optical absorption region, which can be excited to produce more electron-hole pairs under the same visible light irradiation and then result in higher photocatalytic activity.

In addition, increased light absorption and reduced charge recombination are responsible for the enhanced photocatalytic activity [20] of BiVO₄ thin films. As shown in Fig.5.11, the Langmuir-Hinshelwood kinetic equation (equation 2.9. chapter 2) fits quite well with the experimental data (correlation coefficient R² > 0.96), indicating the applicability of the Langmuir-Hinshelwood kinetic model [21]. USP deposited BiVO₄ thin films exhibited considerable enhancement in the photocatalytic removal of MB. The photodegradation rate constant (Fig.5.10 (inset)) for BiVO₄ films deposited at 350 °, 400°, 425° and 500 °C were found

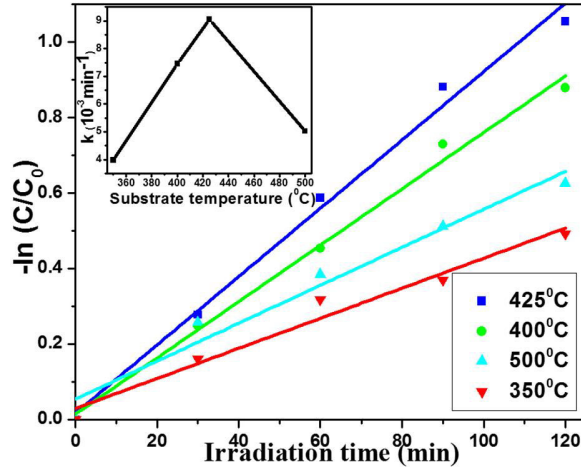


Fig.5.11. Photocatalytic pseudo first order kinetics of BiVO_4 films deposited at different T_{sub} using USP method for the degradation of MB under visible light irradiation (inset: photodegradation rate constant for different T_{sub} deposited USP thin films).

to be 3.98×10^{-3} , 7.46×10^{-3} , 9.05×10^{-3} and $5.02 \times 10^{-3} \text{ min}^{-1}$ respectively. Larger the rate constant, faster will be the reaction rate. Therefore, 425 °C deposited BiVO_4 thin film showed superior photocatalytic activity for the decomposition of MB under visible-light irradiation, mainly due to the reduction in band gap.

5.2.4 Photodegradation study of RF – Sputtered films under Ar atmosphere

Photocatalytic activity of prepared BiVO_4 thin films was evaluated by measuring the degradation of Rh6 in aqueous solution under visible-light irradiation. Fig.5.12 (A) and (B) shows UV-Vis spectra of decomposed Rh6 dye deposited at room temperature (RT) (sample A) and film deposited at a substrate temperature of 450°C (sample B) respectively. Fig.5.12 (A) and (B) inset (AFM images) shows nanocrystalline (sphere-like) and flat surface (smooth) morphology respectively, which is responsible for the temporal evolution of Rh6 dye. The absorbance intensities of Rh6 are gradually decreased in the presence of BiVO_4 thin films with the increase in exposure time, indicating a decrease in Rh6 dye concentrations due to degradation of chromophoric structure of dye [22, 23]. Fig. 5.13 shows photocatalytic degradation efficiency versus visible light irradiation time of the RT and 450°C T_{sub} deposited BiVO_4 films. As shown

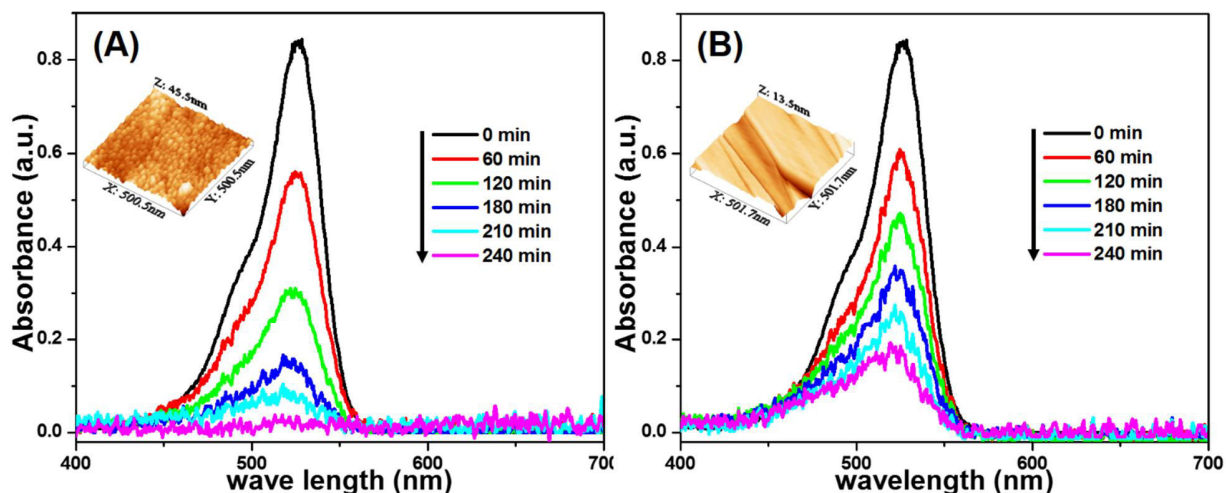


Fig.5.12. Absorption spectra of Rh6 solution in the presence of rf-sputtered BiVO_4 thin films obtained in Ar atmosphere A) RT deposited film and B) 450°C deposited film.

in Fig. 5.13, Rh6 concentration in blank did not change even after being irradiated for 240 min. The degradation rate of Rh6 solution for sample A was $\sim 95.5\%$ and for sample B was only 72.1% after 4 h of visible-light irradiation. This may be due to difference in the band gap between the samples as well as to restricted recombination rates of the charge carriers. In addition, reports have shown that the surface area of a photocatalyst with different morphologies, is an important factor that influences its photocatalytic performance [24, 26].

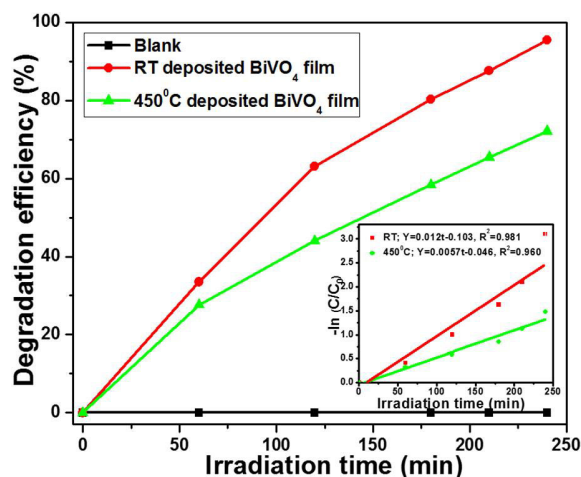


Fig.5.13 Photocatalytic degradation of Rh6 for Ar atmosphere rf-sputtered BiVO_4 thin films (inset: kinetic fit for Rh6 dye degradation with RT and 450°C rf-sputtered films).

As it can be seen from FE-SEM micrographs and AFM images, sample **A** may possess much higher surface area than sample **B** due to its homogenized sphere like morphology. It is clearly seen that, under identical conditions, BiVO₄ thin films composed of spheres had higher photocatalytic activity than films with smoother surfaces. The specific surface effects occurring at interfaces contribute to efficient photocatalytic reaction. Moreover, these investigations confirmed that the band gap, crystallinity and morphology significantly influence the activities of BiVO₄ thin films.

Photodegradation of Rh6 follows pseudo-first-order kinetics which is presented in Fig. 5.13 (inset). The pseudo-first-order rate constant (k_{app}) is in agreement with general Langmuir – Hinshelwood model:

$$-\ln (C/C_0) = k_{app}t \quad \text{--- (5.6)}$$

where k_{app} , C_0 and C denote the apparent reaction rate constant, the initial concentration, and the concentration at the reaction time t , respectively. The plots of $-\ln(C/C_0)$ versus irradiation time are shown in Fig.5.13 (inset). The parameters calculated from the model are also plotted in this figure along with the corresponding correlation coefficients. The pseudo first-order rate constant (k_{app}) for samples A and B are 0.012 and 0.0057 min⁻¹ respectively. This rate constant inferred that, the photodegradation efficiency of Rh6 by sample A was higher than that of sample B, underlying the high photocatalytic activity of the RT deposited BiVO₄ film mainly due to the unique morphology leading to higher activity of such sphere like particles quantitatively.

Several parameters were considered for the photodegradation of Rh6 by BiVO₄ films such as structural aspects, morphology and band gap differences in the deposited films. Compared to XRD, Raman spectroscopy is more sensitive to slight change of metal-O bond lengths as well as lattice perturbations in the local structure. Major Raman bands of both BiVO₄ thin films were shifted to higher frequencies (828 cm⁻¹ red shift, chapter 4, section 4.2.1b, Fig.4.8 D) as compared to typical Raman bands of bulk and well crystallized BiVO₄ [27]. Raman stretching frequency is quite sensitive to the metal-O bond lengths, with higher stretching frequencies corresponding to the shorter metal-O bond lengths [28, 29]. This can be correlated with the work done by Yu *et al* [30] on the photocatalytic properties of BiVO₄ for oxygen evolution from aqueous solution of AgNO₃ under visible light irradiation. They found that the initial rate of O₂ evolution is proportional to the Raman V-O bond stretching frequencies. Yu et

al correlated higher V-O bond stretching frequencies with shorter V-O bond lengths and proposed that shorter V-O bond lengths lead to greater mobility of photogenerated holes improving the photocatalytic activity. On the basis of this discussion, samples which possess shorter V-O bond length are expected to have higher photocatalytic activity. However, the activity for sample B was not as high as sample A due to the main differences in FWHM and intensities of XRD peaks. Crystalline order is more improved in sample A as compared to B even though they exhibited monoclinic scheelite structure. Careful analysis of FE-SEM micrograph reveals many cracks (Chapter 4, section 4.2.1c, Fig.4.9 b) along with grooves on the surface of the 450 °C deposited films. It may be suggested these surface defects acted as recombination centers between photogenerated holes and electrons. Such behavior was also observed by Zhou *et al* [31] for the photocatalytic degradation of rhodamine B using one-dimensional Iron oxide particles.

The difference in the intensities of asymmetric and symmetric deformation vibrations of VO_4^{3-} tetrahedra at 325 and 367 cm^{-1} (chapter 4, section 4.2.1b, Fig.4.8 D) is also a key parameter which differentiates the photocatalytic activity between sample A and B [32]. As the corresponding modes are relatively weak for sample B it can be thought that more distorted VO_4^{3-} tetrahedra are involved in sample B. The distortion in the local structure leads to overlap between the Bi6s and O2p orbitals which enhance the migration of photogenerated holes. Therefore sample deposited at 450 °C exhibited lower photocatalytic activity than expected.

5.2.5. Photodegradation study of Rh6 – Sputtered films under Ar+O₂ atmosphere

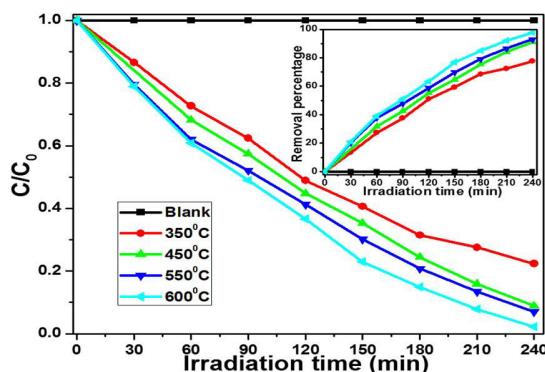


Fig.5.14. Photodegradation of Rh6 in aqueous dispersions under visible light irradiation on BiVO_4 thin films deposited with different T_{sub} under Ar+O₂

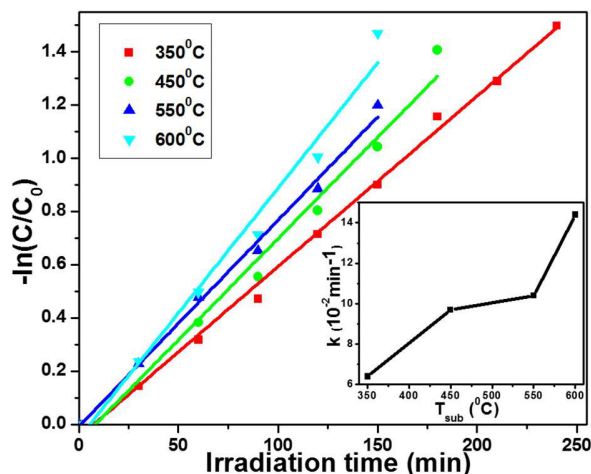


Fig.5.15. Photocatalytic pseudo first order kinetics of BiVO_4 films deposited at different T_{sub} by rf - sputtering for the degradation of Rh6 under visible light irradiation.

Fig.5.14 showed the degradation of Rh6 by using thin films deposited with various substrate temperatures under Ar and O_2 atmosphere. C_0 and C are the initial and residual concentrations of Rh6 at initial time and at time t of irradiation respectively. An experimental blank test (without BiVO_4 thin films) was also performed under visible light irradiation and the results revealed that the concentration of Rh6 remained unchanged in this condition. It can be observed that the absorption peaks of Rh6 solution gradually decreases along with irradiation time in the presence of thin films indicating the decomposition of Rh6 in aqueous solutions.

Depending on the substrate temperatures 350° , 450° , 550° and 600°C , the rate of degradation level was 77%, 91%, 94% and 97% respectively within a time span of 240 min.

Thus, removal percentage of Rh6 degradation correlates with the substrate temperature (T_{sub}) (Fig.5.14 (inset)). In addition, $(-\ln(C/C_0))$ versus irradiation time (t) lead to linear variation characterized by a photocatalytic rate constant depicted in insert of Fig.5.15. The results indicate approximately linear variation of k -factor ($R^2 > 0.95$) with the substrate temperature.

5.2.6. Reusability test of BiVO_4 thin films

One major feature of photocatalyst lies in its stability during the photoinduced degradation process. The possibility of catalyst recovery and reuse in photocatalytic processes is

important, since it can contribute significantly to lower the operational cost for the targeted applications. Reusability and stability of the sputtered films was tested after a photocatalysis experiment.

The structural stability was checked by XRD while surface states are analyzed by SEM. There was no structural change observed before and after the photocatalytic study (Fig.5.16), as depicted by XRD pattern. This indicates that BiVO_4 films are chemically stable under irradiation and against the dye charged solutions.

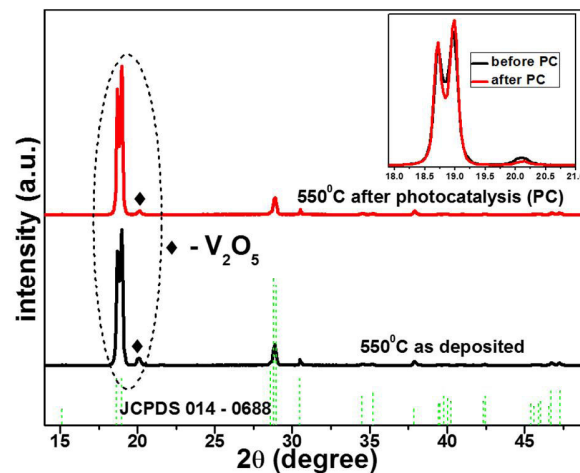


Fig.5.16. XRD patterns of BiVO_4 film deposited at $550\text{ }^\circ\text{C}$ before and after the photocatalytic study.

Fig.5.17 shows SEM images of the BiVO_4 film deposited at $550\text{ }^\circ\text{C}$ substrate temperature before and after photocatalytic reaction. No changes in the film surface morphology were apparent from the SEM analysis. Similar trend was observed for all other rf-sputter deposited films. It can be concluded that the crystallinity and morphology of BiVO_4 films are quite stable even after photocatalytic reactions. The identical measurement conditions confirm the reusability and high stability of monoclinic scheelite BiVO_4 thin films.

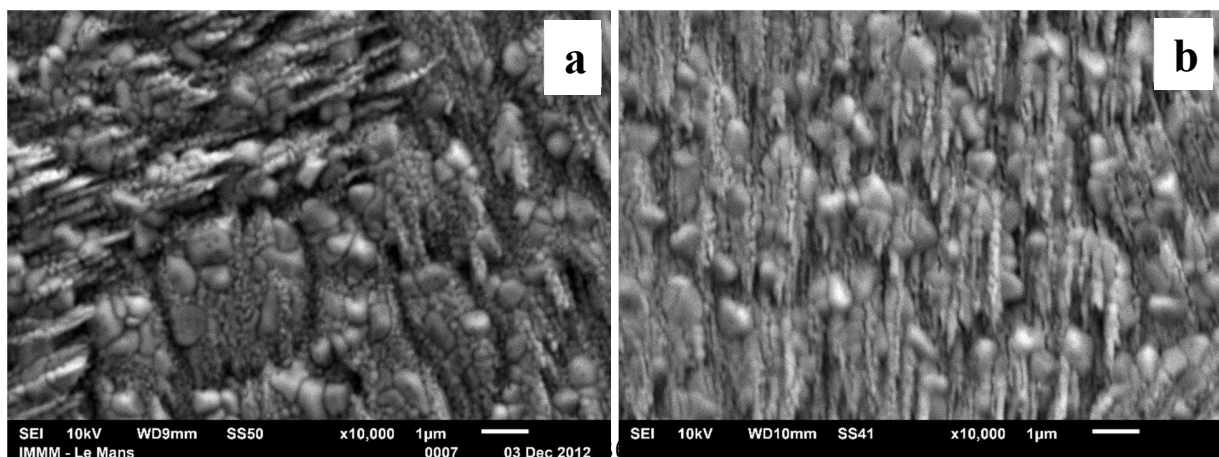


Fig.5.17. SEM surface images of $550\text{ }^\circ\text{C}$ rf-sputtered BiVO_4 film. (a) before (b) after photocatalytic study.

5.3 Conclusion

An efficient visible light driven photocatalyst BiVO₄ powder was prepared via hydrothermal and mechanochemical processes and thin films using USP and rf-sputtering techniques. The effect of synthesis conditions such as, pH and surfactant variation in hydrothermal, BPR and milling time in mechanochemical method and effect of substrate temperature with USP and rf-sputtering have been explored. Ball milled sphere-like BiVO₄ powder shows superior (50% higher) photocatalytic activity as compared to hydrothermally obtained BiVO₄. The difference between surface morphology and size of the particles were compared for the enhanced photocatalytic activity due to its increased surface to volume ratio. For thin film based photocatalysis, films deposited at 425°C using USP showed better performance (66%) compared to the films deposited at 350°, 400° and 500°C narrow band gap (2.09 eV). However, such photocatalytic activity is lower than that demonstrated by using rf-sputtered films. Additionally, the crystalline nature, preferential orientations of film growth, morphology and textures were found to be key parameters in governing the overall photocatalytic performance of BiVO₄ films. XRD and SEM analysis confirms the reusability and photochemical stability of rf-sputtered BiVO₄ thin films after photodegradation reactions. This is crucial fact proves the relevance of bismuth vanadate in photocatalysis applications compared to other photoactive semiconducting oxides. Systematic studies were carried out for better understanding of the key parameters that ensures the best performance of photocatalysis reactions. Such knowledge can be utilized in real applications like wastewater treatment for environment preservation.

References

1. M. I. Litter, *Applied catalysis B: Environmental*, 1999, 23, 89-114.
2. A. Sugunan, J. Dutta, *Nanotechnology*, 2008, 2, 125-147.
3. F. D. Mai, C. C. Chen, J. L. Chen, S. C. Liu, *J. Chromatogr. A*, 2008, 1-2, 355-365.
4. J. Niu, S. Ding, L. Zhang, J. Zhao, C. Feng, *Chemosphere*, 2013, 93, 1-8.
5. S. Obregón, A. Caballero, G. Colón, *Applied. Catal. B, Environ*, 2012, 117-118, 59-66.
6. W. Zhao, C. Chen, X. Li, J. Zhao, *J. Phys. Chem. B*, 2002, 106, 5022-5028.
7. H. Fu, C. Pan, W. Yao, Y. Zhu, *J. Phys. Chem. B*, 2005, 109, 22432-22439.
8. W. Liu, L. Cao, G. Su, H. Liu, X. Wang, L. Zhang, *Ultrasonics Sonochemistry*, 2010, 17, 669-674.
9. S. Gawande, S. R. Thakare, *Indian, J of Chemistry*, 2013, 52, 614-618.

10. H. Zhang, D. Chen, X. Y. Wang, H. Chang, J. Li, *Environ. Sci. Technol*, 2010, 44, 1107-1111
11. J. Zhang, H. Cui, B. Wang, C. Li, J. Zhai, Q. Li, *Chem. Engi Journal*, 2013, 223, 737-746.
12. Z. Zhang, W. Wang, M. Shang and W. Yin, *Catalysis communications*, 2010, 11, 982-986.
13. A. Martinez-de la Cruz, U.M. Garcia Perez, *Materials research bulletin*, 2010, 45, 135-141.
14. D.G. Wang, R.G. Li, J. Zhu, J.Y. Shi, J.F. Han, X. Zong, C. Li, *J. Phys. Chem. C*, 2012, 116, 5082-5089.
15. S.W. Cao, Z. Yin, J. Barber, F.Y.C. Boey, S.C.J. Loo, C. Xue, *ACS Al. Mater. Interfaces*, 2012, 4, 418-423.
16. Z. Zhu, L. Zhang, J. Li, J. Du, Y. Zhang, J. Zhou, *Ceramics International*, 2013, 39, 7461-7465.
17. F. Mei, C. Liu, L. Zhou, W. K. Zhao, Y. L. Fang, J. B. Wang, Y. Y. Ren, *Journal of Korean physical society*, 2006, 48, 1509-1513.
18. W. Liu, Y. Yu, L. Cao, G. Su, X. Liu, L. Zhang, Y. Wang, *J. Hazard. Mater*, 2010, 181 1102-1108.
19. S. Kohtani, M. Koshiko, A. Kudo, et al., *Applied. Catal. B*, 2003, 46, 573-586.
20. P. Sangpour, F. Hashemi, Alireza, Moshfegh, *J. Phys. Chem. C*, 2010, 114, 13955-13961.
21. Y. Li, X. Li, J. Li, J. Yin, *Water Res*, 2006, 40, 1119-1126.
22. Z. Zhang, W. Wang, M. Shang, W. Yin, *Catalysis Communications*, 2010, 11, 982-986.
23. G. Tan, L. Zhang, H. Ren, S. Wei, J. Huang, A. Xia, *Al. Mater. Interfaces*, 2013, 5, 5186-5193.
24. B. Elgh, N. Yuan, H. S. Cho, E. Nilsson, O. Terasaki, Anders E.C. Palmqvist, *J. Phys. Chem. C*, 2013, 117, 16492-16499.
25. D. Arney, L. Fuoco, J. Boltersdorf, Paul A. Maggard, *J. Am. Ceram. Soc*, 2012, 96, 1158-1162.
26. P. Efstathiou, X. Xu, H. Ménard, John T. S. Irvine, *Dalton Trans*, 2013, 42, 7880-7887.
27. M. Gotic, S. Music, M. Ivanda, M. Soufek, S. Popovic, *J. Mol. Struct*, 2005, 535, 744.
28. I. D. Brown, K. K. Wu, *Acta Crystallogr*, 1976, B32, 1957-1959.
29. Y. Liang, T. Tsubota, Lennard, P. A. Mooij, Roel van de Krol, *J. Phys. Chem. C*, 2011, 115, 17594-17598.
30. J. Yu and A. Kudo, *Adv. Funct. Mater*, 2006, 16, 2163-2169.
31. X. Zhou, H. Yang, C. Wang, X. Mao, Y. Wang, Y. Yang, G. Liu, *J. Phys. Chem. C*, 2010, 114, 17051-17061.
32. H. B. Fu, C. S. Pan, W. Q. Yao, Y. F. Zhu, *J Phys Chem B*, 2005, 109, 22432-22439.

6. Summary and perspectives

6.1. Summary

Direct conversion of sunlight into photo electrochemical energy is a preferred method for clean and safe environmental remediation in future. Low cost techniques with realistic potential for direct preparation is developed and presented in this research work. BiVO_4 powders in micro and nanoscale sizes were successfully prepared by hydrothermal and mechanochemical processes and optimized to obtain monoclinic phase. Also BiVO_4 thin films were deposited using ultrasonic spray pyrolysis (USP) and rf-sputtering technique and the parameters were optimized to get homogeneous films. The main objectives that were realized in this work are

- The experimental parameters that influenced the formation of monoclinic BiVO_4 both in powder or thin film form are evaluated and optimized.
- Fundamental characterizations were performed to understand the behavior of material and optimization of properties to obtain good absorption in visible range of electromagnetic spectrum.
- The influence of crystalline phase, degree of crystalline order, morphology, surface states, spectral absorption range and oxygen vacancy on the photocatalytic performance.
- Comprehension of photocatalytic efficiency of BiVO_4 nanostructures for enhanced degradation of organic dyes.

Hence this work can be divided into four parts 1) preparation of micro sized powders using hydrothermal processes 2) preparation of nanopowders using high energy ball milling, 3) deposition of thin films using USP and 4) deposition of thin films by rf-sputtering

Hydrothermal process: Irrespective of the variation in pH and surfactants, well crystallized monoclinic BiVO_4 was obtained with the hydrothermal method. With oleylamine surfactant, micro entities and acicular-like morphologies were synthesized at pH 2 and 9

respectively. Spherical-like morphology was obtained without surfactant. Irregular, cauliflower, porous and ball like BiVO₄ morphologies are obtained with the surfactants such as oleic acid, hexadecyltrimethylammonium bromide, polyvinyl alcohol and polyvinyl pyrrolidone respectively. UV-Visible diffuse reflectance spectra of hydrothermally obtained BiVO₄ samples showed absorption edge in the range of 502-523 nm thus proving visible-light absorption. Formation of monoclinic scheelite structure was substantiated by the results of FT-IR spectra by giving the characteristic band of monoclinic BiVO₄ at 720 cm⁻¹. Hence it can be concluded that, different morphologies of well crystallized BiVO₄ powders can be obtained by varying pH and surfactants.

Mechanochemical process: This technique overcomes the tedious chemical processes since it is one-step synthesis of nanomaterials, to obtain considerably uniform small particles with high purity and an environmental friendly synthesis method. This technique is employed to synthesize nanoparticles with reduced reaction time (6 h) and particle size (20 nm) in comparison with the hydrothermal and other chemical methods. Careful adjustments of the experimental parameters (milling time and balls to powder weight ratio (BPR)) were done to control the particle size, aggregation and crystallinity of the as-prepared BiVO₄ powders. However, annealing temperature at 450 °C was found to play a critical role in improving the crystalline order. Particularly, sharp and well resolved XRD lines indicate good crystalline order involved in BiVO₄ nanoparticles with a net improvement after annealing. The relevant parameters for an optimized synthesis consist of minimal time duration of 6 h and BPR parameters as 10:1. The optical properties were found to be slightly dependent (2.4 - 2.3 eV) on the synthesis conditions and annealing.

For the first time, systematic investigations by dielectric and EPR spectroscopy were performed on these ball milled nanopowders. The main idea was to evaluate the electrical conductivity and the effect of mixed oxidation states of vanadium (V⁵⁺, V⁴⁺) on the conductivity. The paramagnetic and active electronic centers were investigated by EPR and assigned to V⁴⁺ ions involved in crystalline tetrahedral sites of BiVO₄ as clearly stated from the anisotropy of the EPR spectral parameters (g-tensors and hyperfine A-tensors). XRD and FE-SEM results confirmed the feasibility and reproducibility of desired material by ball milling method. It is also worth noting that ball milling is well suited to scale up for the production of large quantities of

powders at an economic cost. Thus it is favorable to use such materials in environmental remediation, public health protection and self-cleaning applications.

Ultrasonic spray pyrolysis: Non-vacuum based USP technique fabricated in our lab was used to deposit BiVO₄ thin films. This is a single step process without any post annealing/chemical treatment. XRD pattern confirms the polycrystalline monoclinic scheelite structure of BiVO₄ along with increased crystallinity and particle size (29 to 37 nm) with increasing substrate temperature (T_{sub} : 300° to 500 °C @ 25 °C interval). FE-SEM micrographs of USP deposited films exhibits relatively compact, dense and fine grain morphology in the range of 40-200 nm. HR-TEM image of film deposited at a substrate temperature of $T_{\text{sub}}= 425$ °C showed sharp and clear lattice fringes indicating good crystalline perfection of the film. Decrement in the film growth rate was observed with increasing T_{sub} . The V-O stretching mode (at 827 cm⁻¹) of BiVO₄ thin films shifted to a higher frequency (833 cm⁻¹) with increment in T_{sub} , indicating that the bond length have become shorter. The narrow band gap of BiVO₄ thin films deposited at 425 °C indicates that this sample has the lower conduction band level, which will increase absorption in the visible light. It should be noted that, in view of adaptability for large scale production and large surface area coating, the spray pyrolysis technique is simple, less cost effective and quite efficient as compared to other techniques.

RF-Sputtering: BiVO₄ thin films with various morphologies were successfully prepared using rf-sputtering by varying three different experimental parameters namely the deposition chamber atmosphere, rf-power and substrate temperatures.

First, BiVO₄ was deposited under Ar atmosphere at different substrate temperatures (RT, 450° and 600 °C) and rf-powers (25 and 50 W). These conditions yield only amorphous film as was confirmed by the broad characteristic XRD peak at 28.8° and also the broad Raman band at 827 cm⁻¹. To determine the crystalline formation/structural rearrangement of films, in-situ XRD experiments were carried out under variable temperatures. This result indicated that the formation of BiVO₄ monoclinic phase occurs within the temperature range of 276°-408 °C. The annealed films show sharp and intense peaks due to the enhancement of crystallinity compared to as-deposited films. It was found that the surface morphology of the BiVO₄ films are dependent on substrate temperatures and reproducible. To exemplify this, nanocrystalline grains were observed in the films deposited at RT with grain size ranging from 15-25 nm. Relatively highly dense with quite low rough inconspicuous grains were obtained for the film deposited at 450 °C.

From the AFM micrographs, surface roughness is evaluated and found to be approximately 4.66 nm and 2.50 nm (rms values) for films deposited at RT and 450 °C, respectively.

Secondly, the main drawback of Ar atmosphere deposition involves two step preparation process (deposition and annealing), hence, there is a need of employing gas mixture comprising of Ar and O₂ resulting in one step formation of stoichiometric BiVO₄ thin films. Keeping this aim, deposition with various oxygen pressures was examined through BiVO₄ films being prepared on BK7 substrate at fixed substrate temperature of 550 °C. XRD pattern shows a preferential orientation with monoclinic phase structure. It was found that [O₂/(O₂ + Ar)] flow-rate had large influence on surface morphology. Beads in a row along with fine grains and bilayer structure was observed for 10% and 2% oxygen flow rate respectively. The deposition rate decreased from 40 nm/min to 35 nm/min with increasing oxygen pressure percentage from 2 to 10% respectively.

Finally, varying the substrate temperature (T_{sub}) the microstructure and crystallinity are tuned which had a direct influence on the optical and electronic properties. So, BiVO₄ films were prepared at different substrate temperature with fixed oxygen partial pressure. XRD results revealed the formation of monoclinic phase of BiVO₄ on the as deposited films. The splitting peak at 18.8° is more prominent by increasing T_{sub} thus emphasizing improvement of crystallinity with rising T_{sub}. Detailed structural analysis revealed that the preferential orientation changes from (-1 2 1) to (1 1 0) when the T_{sub} raised above 450 °C. The film growth was found to decrease from 45 nm/min to 32 nm/min with increasing T_{sub} from 450° to 600 °C. Irregularly shaped grains, autumn leaf like, beads in a row with fine grain morphology were observed for 350°, 450° and 550 °C substrate temperature respectively. The rf-sputtered films with various experimental parameters exhibited strong absorption in the visible light region. The band gap energies of BiVO₄ thin films were estimated to be in the range of 2.09-2.67 eV.

Photocatalysis: Finally BiVO₄ micro and nanostructures prepared by various techniques were tested for the photodegradation of organic dyes namely, rhodamine 6G (Rh6) and methylene blue (MB).

- ✓ Hydrothermally prepared acicular BiVO₄ powders exhibited 86% removal of Rh6 under visible light illumination of 240 min.
- ✓ Mechanochemically prepared BiVO₄ nanoparticles at different milling time has been investigated for photodegradation of Rh6 and MB dyes, which is in the order of 6hrA10:1

< 11hrA10:1 < 16hrA5:1. Size controlled BiVO₄ nanoparticles of 6hA10:1 sample showed 97% removal of Rh6 under visible light illumination of 150 min. The photocatalytic activity of 6hA10:1 sample was 50% superior, as compared to hydrothermally prepared BiVO₄ powder. The enhanced catalytic activity is likely due to the role of high specific surfaces of grains as well as unique surface chemistry properties as probed by FE-SEM and EPR analysis.

- ✓ The photocatalytic activity of monoclinic BiVO₄ thin films grown by USP technique at different T_{sub} were tested for MB degradation. Photodegradation of MB follows the order 425° < 400° < 500° < 300°C. The increased photocatalytic activity is associated with a wide visible light response due to its narrow band gap (2.09 eV).
- ✓ Morphology-controlled BiVO₄ thin films prepared under Ar atmosphere by rf-sputtering at RT (18 nm particle size) had 98% removal of Rh6 in 240 min. The combination of Ar/O₂ sputtering gases avoids two step preparation (deposition and annealing) of the films. Different T_{sub} (350, 450, 550 and 600°C) deposited films confirmed further enhancement of catalytic activity. Porosity, thickness and morphology of the films, significantly enhances the photodegradation activity.
- ✓ The reusability of BiVO₄ thin films was accounted from its unaltered crystalline phase and morphology. Additionally, it was demonstrated that the films are photochemically stable even after the photocatalytic study.

These results evidence the importance of all the above synthesis techniques for better degradation efficiency, which is essential for practical applications. This study opens a new way to prepare well defined functional BiVO₄ nanostructures with enhanced photodegradation performance.

6.2. Future recommendations

BiVO₄ has shown quite versatile and stable morphologies with optimal electronic and optical properties for photocatalysis. However, some aspects of the materials need to be explored for an in-depth understanding and generated database on the materials and their features. Also, some of the uncovered experimental results and demerits of the pristine BiVO₄ system needs to be explored for eventual better improvement of photocatalytic performances.

1. Analyzing BiVO₄ nanostructures by X-ray photoelectron spectroscopy (XPS) for the complete understanding of chemical composition and chemical states with particular emphasis on the surface states.
2. Specific surface (surface area) measurements of powders and nanostructured thin films must be performed. This is of particular interest to support the observed changes of photocatalytic activity as function of film roughness and the nanoparticle morphologies.
3. Apart from surface area, structural and morphological evolution of the sample is responsive for the photocatalytic improvement. Though a systematic study on USP and rf-sputtering, deposited films are presented, in particular with USP, most of synthesis has been done with one concentration of the precursor solution for obtaining crystalline monoclinic phase of BiVO₄. Even though the substrate temperature and carrier gas (air) flow rate were optimized, another systematic study with varying precursor solution and solvent concentration is expected to yield an interesting morphology which will lead to better application.
4. Monoclinic BiVO₄, which has been considered as highly active photocatalyst among its many polymorphs, has a band gap of 2.3-2.6 eV, so it can absorb the visible portion of the solar energy so as to have a theoretical efficiency of 9% for solar-to-chemical conversion. However, the short carrier diffusion lengths and significant recombination of photon generated electron-hole pairs limit the photoactivity of BiVO₄. To enhance the activity of BiVO₄ for water oxidation it is fundamental to reduce electron-hole recombination rates. This can be ensured by metal doping which is expected to have great influence on photocatalytic activities.
5. The recent breakthrough in solar water splitting with BiVO₄ was demonstrated with a low cost, spray-deposited and non-porous tungsten-doped bismuth vanadate photoanode in which carrier-separation efficiencies of up to 80% are achieved. The 4 mA cm⁻² photocurrent corresponds to a solar-to-hydrogen efficiency of 4.9%, which is the highest efficiency yet reported for a stand-alone water-splitting device based on metal oxide photoanodizing tungsten (W) doping of BiVO₄. This was achieved on the dense and cracked thin films. Our experience on photocatalysis can be oriented to water splitting using selective samples from the present work. Additionally, studying the photo-electrochemical properties of pristine BiVO₄ and doping may lead to a noticeable improvement in the application of BiVO₄ in other active area connected with energy or clean environmental needs.

6. It is a well-known fact that hybrid systems as those associating with TiO_2 and dyes for photovoltaic effect can be thought for BiVO_4 systems. Since they can be synthesized in several forms and morphologies, their functionalization by organic molecules can contribute to photoinduced charge transfer and can be used in photocatalysis or in photovoltaic applications.

7. The controlled synthesis of nano and/or micro materials of different structures of pristine BiVO_4 was successfully studied for their photocatalytic dye degradation performance. However, it was reported that composite semiconductors are photocatalytically more active than the individual components. With the formation of heterojunctions, namely p-n or n-n type with appropriate band gaps, they can effectively promote the significant reduction of recombination of photogenerated charge carriers. Coupling monoclinic scheelite BiVO_4 with another semiconductor in forming composites with heterojunctions is an effective approach to enhance separation of generated electron-hole pairs. There are few reports on these composites but it was rather complicated to synthesize the composite and also to obtain different morphologies. Hence we propose that such composites must be explored in detail for their great impetus on improvement of the catalytic performance.

Articles in referred journals:

1. **R.Venkatesan, S.Velumani, M.Tabellout, N.Errien, A.Kassiba “Dielectric behavior, conduction and EPR active centres in BiVO₄ nanoparticles”** Journal of Physics and Chemistry of Solids 74 (2013) 1695-1702.
2. **R. Venkatesan, S. Velumani, A. Kassiba “Mechanochemical synthesis of nanostructured BiVO₄ and investigations of related features”** Materials Chemistry and Physics 135 (2012) 842-848.

International conference contributions

Oral Communications

1. **“High photocatalytic performance of BiVO₄ nanostructured thin films prepared by rf-sputtering”** in symposium 7D of IMRC 2013, Cancun, Mexico, August 11-15, 2013.
2. **“Controllable synthesis of highly efficient BiVO₄ photocatalyst prepared by mechanochemical milling and rf-sputtering”** in symposium R, Photocatalysis of JSAP-MRS joint symposia, Kyoto, Japan, September 16-20, 2013.
3. **“The Effect of deposition parameters on rf-sputtered BiVO₄ thin films”** in symposium 6C of IMRC 2012, Cancun, Mexico, August 12-17, 2012.
4. **“Comparative synthesis routes for photocatalytic nanostructured bismuth vanadate”** in symposium 1A of IMRC 2012, Cancun, Mexico, August 12-17, 2012.
5. **“Synthesis of BiVO₄ by Mechanochemical process and its characterization”** in symposium 5 of IMRC 2011, Cancun, Mexico, August 14-19, 2011.

Poster presentations

1. **“Optimization of BiVO₄ thin film by ultrasonic spray pyrolysis for photocatalytic applications”** in symposium 7D of IMRC 2013, Cancun, Mexico, August 11-15, 2013.
Won first price for the poster presentation among the participants on Tuesday (13/8/2013). Will be presenting the results in the coming MRS spring meeting at San Francisco, USA.
2. **“Mechano-chemical synthesis of BiVO₄ and its enhanced photocatalytic properties for degradation of methylene blue”** in symposium 7D of IMRC 2013, Cancun, Mexico, August 11-15, 2013.

3. **“A Comparative photocatalytic performance of BiVO₄ particles prepared by ball milling and hydrothermal route”** in symposium R, Photocatalysis of JSAP-MRS joint symposia, Kyoto, Japan, September 16-20, 2013.

4. **“Growth mechanism of BiVO₄ thin films deposited by rf sputtering and its characterization”** in symposium 1A of IMRC 2012, Cancun, Mexico, August 12-17, 2012.

Won third price for the poster presentation among the participants on Tuesday (13/8/2012).

5. **“Effect of milling time on BiVO₄ nanoparticles synthesized by mechanochemical process”** in symposium 5 of IMRC 2011, Cancun, Mexico, August 14-19, 2011.

Won third price for the poster presentation among the participants on Wednesday (16/8/2011).

Articles under preparation

1. Surfactant assisted hydrothermal synthesis of BiVO₄: morphological influence on the decomposition of rhodamine 6G.

2. Efficient removal of rhodamine 6G and methylene blue using ball milled nanostructured BiVO₄.

3. Optimization of BiVO₄ thin films by ultrasonic spray pyrolysis for photocatalytic applications.

4. Effect of substrate temperature on the enhancement of photocatalytic degradation of rhodamine 6G dye: BiVO₄ films prepared using rf-sputtering.

5. Enhanced photocatalytic activity of BiVO₄ thin films fabricated by rf-sputtering for rhodamine 6G degradation.

Thèse de Doctorat

Venkatesan RAJALINGAM

TITRE : SYNTHÈSE ET CARACTÉRISATION DES MATÉRIAUX NANOSTRUCTURES DE BiVO_4 : APPLICATION À LA PHOTOCATALYSE

Résumé

Les matériaux pour la photocatalyse en lumière visible ont attiré un grand intérêt car ils peuvent exploiter tout le spectre d'irradiation solaire notamment afin de détruire des polluants organiques pour l'environnement comme dans la purification de l'eau. Dans ce contexte, le bismuth de vanadates (BiVO_4) est digne d'intérêt en raison de sa largeur de bande interdite électronique ($\sim 2,3$ eV) et sa potentielle activité photocatalytique. Des études systématiques ont été menées pour les caractéristiques physico-chimiques de poudres BiVO_4 synthétisées par voie hydrothermale et par broyage mécanique à haute énergie. La pertinence de la méthode de mécano-synthèse a été démontrée grâce notamment à son faible coût de fonctionnement, de mise en œuvre facile ainsi que le nombre limité de paramètres et la possibilité d'obtenir des particules à taille réduite (20-100 nm) avec une phase cristalline monoclinique. En couches minces, les matériaux BiVO_4 ont été synthétisés par pulvérisation ultrasonique (USP) et par pulvérisation cathodique radiofréquence (rf). Les paramètres pour des dépôts optimaux ont été identifiés permettant d'obtenir des films minces sans fissures, suffisamment denses avec des surfaces texturées à morphologies contrôlées. Les études structurales, vibrationnelles, et les propriétés électroniques et optiques ainsi que leur interprétation grâce à des modèles ont été menées pour une parfaite connaissance des caractéristiques des matériaux BiVO_4 . Pour les applications visées, BiVO_4 sous forme de poudres et de films minces ont été utilisés comme photocatalyseurs pour la dégradation de rhodamine 6G (Rh6) et le bleu de méthylène (MB) sous irradiation en lumière visible. La structure scheelite monoclinique de nanoparticules sphérique de BiVO_4 obtenues par mécano-synthèse, ont montré une efficacité améliorée (+50%) de l'activité photocatalytique par rapport à des particules de forme aciculaire obtenues par voie hydrothermale. Dans le cas de films minces, le taux de dégradation du BM est de l'ordre est de 66% pour les films synthétisés par USP alors qu'un taux de 99% a été atteint avec des films obtenus par pulvérisation cathodique rf. Ces travaux valident les propriétés photocatalytiques remarquables de BiVO_4 par rapport aux matériaux existants avec des applications prometteuses, notamment dans la résolution de problèmes environnementaux.

Mots clés

BiVO_4 , Semiconducteurs, Nanopoudres, Films minces, Synthèse hydrothermale, Mécano-synthèse, Méthode de pulvérisation ultrasonique, Pulvérisation cathodique rf, Photocatalyse, Propriétés électroniques et optiques, dégradation de polluants organiques.

Abstract

Visible light photocatalysts have attracted a great interest since it may exploit the wide solar irradiation spectrum to destroy organic dyes as required for environmental need such as water purification. In this context, bismuth vanadate (BiVO_4) is worth of interest due to its narrow band gap (~ 2.3 eV) and the ability to exhibit efficient photocatalytic activity. Systematic studies have been carried out on the physico-chemistry of BiVO_4 synthesized as powders by hydrothermal and mechano-chemical techniques. The relevance of ball milling method was demonstrated through its low processing cost and easy scaling up as well as limited variable parameters to obtain reduced particle sizes down to (20-100 nm). As thin films, BiVO_4 were grown by ultrasonic spray pyrolysis (USP) and rf-sputtering techniques. Optimum deposition parameters were identified, leading to the formation of crack free, dense media with textured surfaces composed by controlled morphologies. Analysis of the structural, vibrational, electronic and optical experiments, interpretation and development of models were carried out for deep insight on the properties of BiVO_4 materials. For concrete applications, BiVO_4 as powders and thin films were used as photocatalysts for the degradation of rhodamine 6G (Rh6) and methylene blue (MB) under visible light irradiation. Monoclinic scheelite structure of spherical-like BiVO_4 nanoparticles obtained by mechano-chemical process, have shown 50% more efficient photocatalytic activity compared to acicular-like BiVO_4 grains obtained by hydrothermal method. The average degradation rate of MB using USP grown films was found to be 66% during 120 minutes. A significant rate increase in the photocatalytic activity up to 99% was achieved by using rf-sputtered films. Thus, BiVO_4 was demonstrated as efficient photocatalysts compared to existing materials with promising applications notably in solving environmental problems.

Key Words

BiVO_4 , Semiconductors, Nanopowders, Thin films, Hydrothermal synthesis, Mechano-chemical process, Ultrasonic spray pyrolysis, rf-sputtering, Photocatalysis, Electronic and optical properties, degradation of organic pollutants.